Ontwerp en modellering van anisotrope lichtgevende dunnefilmapparaten met behulp van vlakkegolfexpansie

Design and Modelling of Anisotropic Thin Film Light-Emitting Devices with the Plane Wave Expansion Method

Lieven Penninck

Promotoren: prof. dr. ir. K. Neyts, prof. dr. ir. P. De Visschere
Proefschrift ingediend tot het behalen van de graad van
Doctor in de Ingenieurswetenschappen: Fotonica

Vakgroep Elektronica en Informatiesystemen
Voorzitter: prof. dr. ir. J. Van Campenhout
Faculteit Ingenieurswetenschappen en Architectuur
Academiejaar 2012 - 2013

UNIVERSITEIT
GENT

ISBN 978-90-8578-579-8
NUR 924, 959
Wettelijk depot: D/2013/10.500/12

Promotor:

Prof. Kristiaan Neyts	Ghent University, ELIS

Co-Promotor:

Prof. Patrick De Visschere	Ghent University, ELIS

Examination committee:

Prof. Jeroen Beeckman	Ghent University, ELIS
Prof. Peter Bienstman	Ghent University, INTEC
Prof. Patrick De Baets	Ghent University, Mechanische Constructie en Productie (chair)
Prof. Patrick De Visschere	Ghent University, ELIS
Prof. Malte Gather	Technical University of Dresden
Prof. Pascal Kockaert	Université Libre de Bruxelles
Prof. Kristiaan Neyts	Ghent University, ELIS
Prof. Dirk Poelman	Ghent University, Solid State Sciences

This work has been supported by the Flemish agency for Innovation through Science and Technology(IWT).

Dankwoord

Beste lezers,

Terwijl jullie op zoek waren naar dit dankwoord, jullie willen natuurlijk weten of jullie wel vermeld worden, is jullie waarschijnlijk hier en daar een wiskundige formule opgevallen. Wie schrik heeft niks te zullen opsteken bij het lezen omdat het allemaal ondoorgrondbaar wiskundig gekrabbel is, mag opgelucht ademhalen. U leert hier het woord “floccinaucinihilipilification”, hetgeen betekent “iets waardeloos bevinden”, dat naar verluidt het langste engelse woord is. Met zoiets kan je indruk maken aan op café. Hopelijk zullen jullie ook de rest van deze thesis niet “floccinaucinihilipilificaten“. Ik heb er mijn uiterste best voor gedaan, maar eerlijk gezegd was het nooit gelukt zonder hulp van een heel pak mensen.

Van dit proefschrift was niets in huis gekomen zonder de geduldige begeleiding van mijn promotoren: Kristiaan en Patrick. Zij waren altijd beschikbaar met advies, uitleg en ideeën, maar ook om fouten te ontdekken en de puntjes op de i te zetten. Het laten kristalliseren van ideeën in een meanderende wetenschappelijke discussie heeft mij niet alleen veel bijgebracht maar was zelf een vorm van ontspanning.

Gedurende dit project had ik het voorrecht samen te werken met heel wat fijne collegas. In eerste instantie de “OLED-mensen”: Saso, Wouter (Woesty), Mohammed, Geraldine en Thomas. Die mij vergezeld hebben op lange autoritten naar vergaderplaatsen, bij het schrijven van “deliverables” en het rond telefoons gekluisterd zitten voor “telcos”. Maar ook de kantoor maatjes: Filip S., Filip B., Bart, Matthias, Masoumeh, Oksana, Jannis, John, Joanne en alle andere huidige en vroegere bewoners van de Fyselek-gang: Manoj, Caspar, Toon, Samira, Stephane, Aimi, Koen, Björn, Jendrei, Pieter, Jeroen, Glen, Yi, Wout, Olliver, Tom, Alex en Marc.

Ook de vele externe partners die bijgedragen hebben door het vervaardigen en meten van samples wil ik niet vergeten. In het bijzonder, hartelijk dank aan Ralf Krausse en Frank Steinbacher van Siemens en Sebastian Reineke en Simone Hoffman van de Technische Universiteit Dresden. Alsook de andere partners van: Philips Aachen, Novaled, Evonik, St. Gobain, Microsharp, OM&T, …

Voor alle fijne avonturen en dolle fratsen die mij de afgelopen jaren veel plezier bezorgden, om af en toe een beetje gezaag te verdragen en mij er op gezette tijden in te peperen dat “de universiteit een beschutte werkplaats voor intellectuelen is”. Bedankt: Daan, Rasta, WP, Kelly, Ruth, Tine, Sofie, Pumba, de jonge (en al iets minder jonge) Trefpunters, de NAC & Zone Gent’ers, de oude Sint-Lievens boys, klimkompanen en alle andere kenissen en sympathisanten…

Tenslotte zijn er nog een aantal mensen waar op zich niks mis mee is. Pennincks zowel van geboorte als aangetrouwd: mijn ouders, broer, zus en haar kroost. En mijn persoonlijke keuze om aan de familie toe te voegen: Edwina.

Lieven Penninck
22 Januari 2013, Gent

Table of contents

Samenvatting

Van een kind dat met een zaklamp speelt tot de ontwikkeling van geavanceerde telescopen en lasers, licht begrijpen en manipuleren fascineert talloze mensen. Ons dagdagelijks leven is moeilijk voorstelbaar zonder de veelheid aan lichtbronnen die ons omgeven. In de afgelopen twee eeuwen zijn heel wat verschillende lichtbronnen uitgevonden. Deze worden niet alleen gebruikt voor verlichting maar ook in hogesnelheids communicatie, zeer precieze metingen, heelkundige ingrepen, …

Geen enkele lichtbron is perfect geschikt voor al deze toepassingen. Het is belangrijk om over gepaste lichtbronnen te beschikken die op een efficiënte wijze licht genereren en om dit licht op efficiënte wijze te gebruiken voor het be-oogde doeleinde. Dit werk richt zich op twee technologieën voor lichtopwekking met een verschillend doel: organische licht emitterende diodes (OLEDs) en vloeibaar kristal (LC) lasers.

Deze twee technologieën werden bestudeerd door middel van numerieke simulaties via expansie in vlakke golven. Vlakke golf expansie is gebaseerd op het principe dat ingewikkelde electromagnetische velden kunnen ontbonden worden als een reeks vlakke golven. In het bijzonder werd anisotroop gedrag in beide technologieën onderzocht. Hiervoor werd de techniek, die welbekend is voor isotrope materialen, uitgebreid naar emissie en propagatie van licht in optisch anisotrope, dunne (één-dimensionale) films.

Organische LEDs voor energie zuinige verlichting

Ongeveer 20% van het wereldwijde elektriciteitsverbruik gaat op aan elektrische verlichting. De meerderheid van deze lampen zijn vandaag de dag nog steeds gloeilampen of halogeen lampen. Zowel gloeilampen (18lm/W) als halogeen lampen (20 lm/W) verbruiken een hoog vermogen. Door gloei- en halogeenlampen te vervangen door zuinigere verlichting kan het totale elektriciteitsverbruik (en de bijhorende rekening en milieuvervuiling) gevoelig dalen. Een aantal bekende alternatieven zijn de TL-buis (tot 100lm/W) , de compacte fluorescente lamp, gekend als spaarlamp, (tot 60lm/W) en vaste stof verlichting zoals inorganische licht emitterende diodes (LEDs) (tot 90 lm/W commercieel verkrijgbaar, >100lm/W in onderzoeksresultaten).

Organische licht emitterende diodes (OLEDs) zijn een type vaste stof verlichting dat een snelle ontwikkeling doormaakt. OLEDs stralen licht uit over een groot uniform oppervlak, in tegenstelling tot inorganische LEDs die kleine, zeer heldere puntbronnen zijn. Witte OLEDs met een efficiëntie tot 90lm/W[1] zijn al gemaakt. Daarenboven stralen OLEDs een breed spectrum dat kleuren natuurlijk weergeeft uit (hoge CRI). OLEDs kunnen zelf doorzichtig en/of flexibel zijn.

Een OLED bestaat uit een of meer dunne (~100nm) lagen organisch materiaal met halfgeleider-achtige eigenschappen tussen twee, eveneens dunne, electrodes. Als een spanning wordt aangelegd over de elektroden, worden elektronen geïnjecteerd aan de kathode en holtes geïnjecteerd aan de anode. De elektronen en de holtes bewegen vervolgens doorheen de organische lagen. Wanneer een elektron en een holte elkaar ontmoeten, kunnen ze recombineren en daarbij een foton uitstralen. De organische lagen kunnen gedeponeerd worden door opdamping in de gas-fase of vanuit een oplossing door spincoating, printen, enzovoort.

OLED technologie heeft een grote ontwikkeling doorgemaakt en OLED schermen zijn nu te vinden in moderne GSMs en ook de eerste OLED lampen zijn op de markt verschenen. Niettegenstaande die grote vooruitgang hebben OLEDs hun volledig potentieel nog niet bereikt. Een probleem is dat geschikte blauw emitterende materialen (en geschikte gastheer materialen) die een lange levensduur en een efficiënte (fosforescente) uitstraling combineren nog niet bekend zijn. De betrouwbaarheid van de fabricage moet verbeteren om grote OLED panelen met hoge opbrengst (yield) te vervaardigen. Ook de energie efficientie van standaard OLEDs kan nog sterk verbeterd worden.

De voornaamste reden voor de lage efficiëntie van huidige OLEDs is de lage optische uitkoppeling in conventionele (vlakke) OLEDs. Het grooste deel van het licht dat in de OLED gegenereerd wordt, blijft gevangen in de OLED door total interne reflectie (TIR). TIR treedt op wanneer een golf met een grote hoek vanuit een materiaal met een hoge brekingsindex invalt op een grens met een materiaal met lage brekingsindex. Enkel licht met een invalshoek kleiner dan 34° in de organische lagen, waar het licht gegenereerd wordt, is in staat uit de OLED te ontsnappen. In een typische OLED wordt om die reden slechts 20% van het licht uitgekoppeld.

In mijn onderzoek heb ik manieren bestudeerd om de efficiëntie te verhogen door uitstraling van licht met kleine invalshoek te bevorderen. Hiervoor heb ik gebruik gemaakt van vlakke golf simulaties van emissie van licht.

Het uitstralingspatroon van OLEDs wordt sterk beïnvloed door interferentie tussen de uitgestraalde golven en hun reflectie aan de metalen cathode. Emissie binnen de ontsnappingskegel wordt versterkt door constructieve interferentie als de afstand tussen de emitterende laag en de cathode goed gekozen is. De kathode veroorzaakt ook een ander belangrijk effect: het optreden van plasmon golven aan het metaaloppervlak en absorptie van het nabije veld. De koppeling met plasmon golven kan gevoelig verminderd worden door de afstand tot de kathode te vergroten. Bovendien hangt de koppeling met plasmon golven ook af van de oriëntatie van de emitterende dipoolmomenten.

In de meeste emitterende materialen zijn de dipoolmomenten isotroop verdeeld, zodat evenveel licht uitgestuurd wordt in alle richtingen (weliswaar gewijzigd door interferentie in de OLED lagen). Maar de uitstraling van elk individueel dipoolmoment is gericht rondom het evenaarsvlak van de dipool. Door analyse van de fotoluminescente vervaltijden in verschillende laagstructuren heb ik aangetoond dat in bepaalde fosforescente materialen de verdeling van dipoolmomenten anisotroop is met 80% van de dipolen in het vlak evenwijdig met de OLED lagen.

Onze simulaties tonen dat als alle dipolen in het vlak georiënteerd zijn, de uitkoppeling efficiëntie naar lucht verhoogt van 20% tot 30%. Anisotrope emitters kunnen gecombineerd worden met uitkoppelstructuren zoals microlensfolies om nog hogere uitkopppelefficiënties te bekomen. Met een volledig georiënteerde emitter is bijna 70% van het licht beschikbaar in het substraat waar het kan geëxtraheerd worden door andere uitkoppelstructuren.

Cholesterische vloeibare kristallen voor lage kost miniatuurlasers

Vloeibare kristal displays (LCDs) zijn de voornaamste technologie voor vlakke beeldschermen geworden. Maar de mogelijkheden van vloeibare kristallen zijn niet beperkt tot beeldschermen. De optische eigenschappen van vloeibare kristallen(LCs) kunnen makkelijk geregeld worden door middel het aanleggen van relatief lage elektrische velden. Die eigenschap heeft de interesse in vloeibare kristallen gewekt voor heel wat andere optische toepassingen zoals regelbare filters, regelen en trimmen van golfgeleiders, luminescente zonneconcentratoren voor “smart windows”, zelfs OLEDs. Onlangs werden ook lage kost kleurstof (“dye”) lasers gemaakt gebaseerd op de hoge reflectiviteit van cholesterische vloeibare kristallen.

Materialen in de vloeibaar kristallijne toestand delen eigenschappen van de vloeibare en de vaste (kristallijne) toestand. Een vloeibaar kristal kan vloeien en bewegen zoals een vloeistof maar de moleculen behouden een deel van de ordening uit de vaste toestand. Een nematisch vloeibaar kristal bestaat uit sigaar-vormige moleculen die allemaal in de zelfde richting ge-oriënteerd zijn. De brekingsindex van het LC is verschillend voor elektromagnetische golven met een elektrische veld evenwijdig aan de LC moleculen dan voor golven met elektrische velden loodrecht op de moleculen.

In een cholesterisch vloeibaar kristal(CLC) draaien de vloeibaar kristal moleculen ten opzichte van elkaar zoals een schroef. De afstand waarover de schroef 360° draait heet de pitch. Het profiel van de brekingsindex varieeert periodiek in een CLC, dat veroorzaakt hoge reflecties voor golflengtes ongeveer even lang als de pitch. Het golflengte gebied waarin hoge reflecties optreden staat bekend als de “bandgap” van het CLC. Zulke “zelf-vormende spiegels” maken het mogelijk om optische componenten met een lage kostprijs te vervaardigen.

Wanneer bovendien nog een laser dye opgelost is in het CLC, kan een laser gemaakt worden. Binnenin de CLC film onstaat een staande golf voor golflengtes aan de rand van de bandgap. Als de dye moleculen geëxciteerd worden tot boven de drempel met een gepulste korte golflengte pomplaser dan zendt de CLC-film laserlicht, met een langere golflengte, uit in de loodrechte richting. De dikte van de film bedraagt ongeveer 10 µm. Laser emissie in CLCs is mogelijk over het volledige zichtbare spectrum met behulp van verschillende dye molecules. De golflengte kan op verschillende manieren geregeld worden binnen een bereik van ongeveer 50nm. CLC lasers ondervinden nog hinder van de hoge drempel voor laser werking en een beperkt uitgestraald vermogen en ook door verbleken (“bleaching”) van de laser dye.

In dit werk wordt het uitsralen van licht door CLCs gesimuleerd voor zowel spontane als gestimuleerde emissie. Het gemeten emissiespectrum onder verschillende hoeken en de polarizatie worden correct voorspeld door de vlakke golf expansie. Verder werd een methode om de drempelversterking en de laser golflengte te schatten ontwikkeld en experimenteel geverifieerd. Optische versterking wordt behandeld door een versterkingsterm toe te voegen aan de brekingsindices. Dit model kan een nuttig hulpmiddel blijken bij het ontwerp van meer geavanceerde vloeibaar kristal lasers.

Summary

From a child toying with a flashlight to today's advanced telescopes and lasers, manipulating and understanding light has fascinated countless people. It is hard to imagine everyday life without the light sources installed all around us. In the past two centuries many different light sources have been invented. The most obvious use for a light source is illumination. But light is also used for high-speed communication, high accuracy measurements, surgery, ...

No single light source is perfect for all these applications. It is important to have light sources which generate light in an efficient way and to use the generated light efficiently for the targeted purpose. This work is focused on two light generating technologies for different purposes: organic light emitting diodes (OLEDs) and liquid crystal (LC) lasers.

These two devices were investigated by numerical simulation using plane wave expansion. Plane wave expansion is based on the principle that complicated electromagnetic fields can be described as a series of plane waves. In particular anisotropic behaviour in both devices was examined. For this the plane wave expansion technique, which is well known for isotropic materials, was expanded to treat light emission and propagation inside thin (one dimensional) films of uniaxially anisotropic materials.

Organic LEDs for energy efficient lighting

Electrical lighting accounts for around 20% of the worldwide electricity consumption. Today the majority of lamps are still incandescent light bulbs or halogen lamps. Both incandescent (18 lm/W) and halogen lamps (20 lm/W) are very power consuming. Replacing incandescent and halogen lamps with more energy efficient lighting will significantly decrease the total electricity consumption (and the cost and pollution that come with it). Some well known alternatives are the fluorescent tube (up to 100lm/W), compact fluorescent lamp (up to 60lm/W), usually called “energy saving lamp”, and solid state lighting like inorganic light emitting diodes (LEDs) (up to 90 lm/W commercially available, >100 lm/W in laboratory results).

Organic light emitting diodes (OLEDs) are a type of solid state light source that is developing rapidly. OLEDs emit light in a large uniform area, unlike inorganic LEDs which are small very bright point sources. White OLEDs with an efficiency as high as 90lm/W [1] have been made, furthermore a broad spectrum with good colour rendering properties is emitted (high CRI). Even transparent and flexible OLEDs can be made.

An OLED is made by depositing thin (~100nm) layers of organic materials with semiconductor-like properties between two electrodes. When a voltage is applied over the electrodes, electrons are injected at the cathode and holes are injected at the anode. The electrons/holes traverse through the device. When an electron encounters a hole they can recombine and emit a photon. The organic materials can be deposited from the gas phase by evaporation or from a solution by spincoating, printing, ...

OLED technology has progressed rapidly and OLED displays are now available in high-end mobile phones and the first OLED lamps have been introduced to the market. Even though OLED technology has made great progress, OLEDs have not yet realized their full potential. One issue is the lack of blue emitting materials (and suitable organic hosts) with a long lifetime and efficient (phosphorescent) light emission. The reliability of fabrication should also improve to make large OLED panels with a high yield. The energy efficiency of standard OLEDs can still be significantly improved.

The major reason for this low efficiency is the poor optical outcoupling of conventional (planar) OLEDs. A majority of the light generated inside OLEDs cannot escape from the device due to total internal reflection (TIR). When a light waves impinges on a boundary between one material with high and another with low refractive index at oblique angles, it is 100% reflected. Only light with an angle below 34° in the organic layers, where light is generated, is able to escape the device. In a typical OLED only 20% of the light is outcoupled because of this effect.

In my research I have studied ways to promote light emission in shallow angles, thereby increasing the outcoupling efficiency. For this I have used plane wave simulations of the light emission.

The emission pattern of OLEDs is strongly influenced by interference between the emitted waves and their reflection at the metal cathode. Emission in the escape cone is enhanced by constructive interference if the distance between the cathode and the emission site is properly chosen. Another significant effect of the cathode is the occurrence of surface plasmon waves and absorption of the near field. Surface plasmon waves are bound to the metal interface and cause optical losses in OLEDs. With the plane wave expansion I was able to deduce analytical formulas to estimate the power lost to plasmon waves. The coupling to plasmon waves is strongly reduced by increasing the distance to the cathode. Furthermore the coupling to plasmon waves depends on the orientation of the emitting dipole moments.

In most emitting materials the dipole moments are distributed in an isotropic way, and light is emitted in all directions (modified by interference in the OLED layers). But the radiation of each individual dipole is directed around the equatorial plane of the dipole moment. By analyzing the photoluminescent decay times in different microcavities, a phosphorescent emitter with an anisotropic distribution of 80% in-plane dipoles is demonstrated.

Simulations show that if all dipoles are arranged in-plane with the OLED layers the outcoupling efficiency to air would improve from 20% to 30%. Anisotropic emitters can be combined with known outcoupling techniques like microlens foils to provide even higher outcoupling efficiencies. With a fully oriented emitter nearly 70% of the light is reaches the OLED substrate where it is available for extraction by outcoupling foils.

Cholesteric liquid crystals for miniature low cost lasers

Liquid crystal displays (LCDs) have become the dominant technology for flat panel displays. But the use of liquid crystals is not limited to displays. The optical properties of liquid crystals can be tuned easily by moderate electric fields. This feature has sparked interest in liquid crystals for other optical applications like tuneable filters, tuning and trimming of waveguide devices, luminescent solar concentrators for smart windows, OLEDs and recently miniature, low cost dye lasers based on the high reflectivity of cholesteric liquid crystals.

Materials in the liquid crystal state share properties of both the liquid and the solid (crystal) state. A liquid crystal can flow and move like other liquids but the ordering of molecules, typical for the solid state, is partly preserved. A nematic liquid crystal consists of cigar-shaped molecules that are all oriented in the same direction. The refractive index of the LC is different for electromagnetic waves with an electric field parallel or perpendicular to the LC molecules.

In a cholesteric liquid crystal (CLC) the liquid crystal molecules are rotated like a screw with respect to each other, the distance over which the screw rotates a full 360° is known as the pitch of the CLC. In a CLC the refractive index changes periodically, causing strong reflection of light with wavelengths around the same size as the pitch and circular polarization of the same helicity as the CLC. The wavelength range of strong reflection is known as the bandgap of the CLC. This “self-manufacturing mirror” has sparked the interest in CLC for making low cost optical components.

When organic laser dye molecules are dissolved into the CLC, a laser can be made. A CLC film supports a resonant standing wave for wavelengths at the edge of the bandgap. When the dye molecules are pumped above the lasing threshold by a pulsed shorter wavelength pump laser, longer wavelength laser light is emitted perpendicular to the CLC film. The thickness of the CLC film is around 10µm. Laser emission has been shown across the entire visible spectrum employing different dye molecules [2]. The emission wavelength can also be tuned across ranges of about 50nm in different ways. However CLC lasers are still hindered by high lasing thresholds and low output power, as well as bleaching of the dye molecules.

In this work the light emitting properties of CLC films are simulated with the anisotropic plane wave expansion method both for spontaneous and stimulated emission. The measured emitted spectrum at different angles and polarization are accurately modelled by the plane wave expansion. A model for estimating the gain threshold and laser wavelength of CLC films was developed and verified by experiment. Optical amplification is treated by introducing gain terms to the refractive index. This model may prove a valuable tool to design more advanced liquid crystal lasers.

List of Symbols

Symbol	Unit	Description
$\overline{\overline{A}}$	-	Field reflection matrix of a layer stack
α	%	Effective fraction of horizontal dipoles
c	m/s	Speed of light in vacuum
c	-	Optical axis of a uniaxial medium
β	°	Inclination angle of the optical axis
γ	°	Azimuth angle of the optical axis
e^-	C	Unit charge
EQE	-	External quantum efficiency
E_{photon}	J	Energy of a single photon
ε_0	F/m	Dielectric permittivity of vacuum
$\varepsilon_\perp$	F/m	Perpendicular dielectric constant
$\varepsilon_{\|\|}$	F/m	Parallel dielectric constant
F	-	Normalized total power generated by a dipole antenna integrated over wavelength
F_λ	-	Normalized total power generated by a dipole antenna per wavelength
Γ_{nr}	μs^{-1}	Non-radiative decay rate
Γ_r	μs^{-1}	Radiative decay rate

Symbol	**Unit**	**Description**
$\Gamma_{r,0}$	μs^{-1}	Radiative decay rate in an infinite medium
Γ_{tot}	μs^{-1}	Total decay rate
h	Js	Planck constant
I_i	-	Normalized radiative flux in medium i integrated over wavelength
$I_{i,\lambda}$	-	Normalized radiative flux in medium i integrated per wavelength
J	A/m²	Current density
K	m²	Normalized power flux per κ^2 integrated per wavelength
K_λ	m²	Normalized power flux per κ^2 per wavelength
$P(\theta)$	1/sr	Normalized power flux per space angle integrated per wavelength
$P_\lambda(\theta)$	1/sr	Normalized power flux per space angle per wavelength
P	nm	Pitch of a cholesteric liquid crystal
$\mathbf{k}$	1/m	Wave vector of a plane wave
k_i	1/m	Component of $\mathbf{k}$ along direction i
κ	1/m	in-plane component of $\mathbf{k}$
$\mathbf{L}$	-	Director of a liquid crystal
λ	m	Wavelength
μ	N / A^2	Magnetic permeability of vacuum
N_{e^-}	-	Number of electrons injected
N_{exc}	-	Number of excitons formed
N_{h^+}	-	Number of holes injected
η_{cb}	-	Charge balance
η_{st}	-	Singlet-triplet ratio
$\eta_{out,i}$	-	Optical outcoupling efficiency into medium i
η_{rad}	-	Radiative decay efficiency

Symbol	**Unit**	**Description**
$\mathbf{p}$	Cm	Dipole moment
ν	°	Inclination angle of a dipole moment
ζ	°	Azimuth angle of a dipole moment
LF	lm	Luminous flux
LE	lm/W	Luminous efficacy
LCE	Lm/A	Luminous current efficacy
RF	W/m	Radiative flux per unit wavelength
$S_0(\lambda)$	1/nm	Emission spectrum of a dye in a homogeneous medium
S_{dye}	-	Order parameter of dye molecule orientation in LC
τ	μs	Decay time
θ_{TIR}	°	Total internal reflection angle
θ	°	Inclination angle of a plane wave
φ	°	Azimuth angle of a plane wave
V_{on}	V	“turn on” voltage
$V_0(\lambda)$	Lm/W	Eye sensitivity curve
ω	1/s	Angular frequency
$\mathbf{1}_{e/o}$	-	Unit vector along the direction of (extra-) ordinary polarization

List of Abbreviations and Acronyms

Abbreviation	Description
CLC	Cholesteric Liquid Crystal
EBL	Electron Blocking Layer
EML	Emitting Layer
ETL	Electron Transport Layer
HBL	Hole Blocking Layer
HOMO	Highest Occupied Molecular Orbital
HTL	Hole Transport Layer
IR	Infra-Red
LC	Liquid crystal
LED	(inorganic) Light Emitting Diode
LUMO	Lowest Unoccupied Molecular Orbital
MBI	Multiple Beam interference
MSE	Mean Square Error
PBG	Photonic bandgap
PWE	Plane Wave Expansion
OLED	Organic Light Emitting Diode
TIR	Total internal reflection

Abbreviation	Description
UV	Ultra-violet
VCSEL	Vertical cavity Surface Emission Laser
WAI	Wide Angle Interference

1. Introduction

“Imagine you’re sitting next to a swimming pool and somebody dives in. When lots of people have dived into the pool, there is a very great choppiness of all the waves all over the water. And to think that it’s possible that some sort of insect with sufficient cleverness could sit in the corner of the pool and by the nature of the irregularities and bumping of the waves has figured out who jumped in where and when and what’s happening all over the pool. That is what we are doing when we look at something.”- R. Feynman[3]

This analogy illustrates the importance of light to our daily lives and how remarkable it is that we can derive so much from the seemingly chaotic electromagnetic waves which fall upon our irises. All this information about size, shape, position, etc. is carried to us by light waves which are just bouncing up and down through the air. Optical modelling and analysis, that’s what this thesis is about, is in fact the same thing as looking at something but taken even further. By carefully measuring, analyzing and studying the electromagnetic waves and understanding their nature, we can find out what is really happening inside tiny devices. By finding out how things work, we can improve them to be more useful to us. And that is where the scientific fascination for finding things out can help the entire society (even those not fascinated by light).

Naturally society has a great need for high quality light sources for all kinds of circumstances. No single light source is perfect for every possible application. This work is situated in an effort to develop high performance light sources. It is important to have light sources which generate light in an efficient way but also to use the generated light efficiently for the targeted purpose. This work is focused on two light generating technologies for different purposes: organic light emitting diodes (OLEDs) and liquid crystal (LC) lasers.

In the following sections of this introductory chapter the possibilities of these technologies are further elaborated. First we take a more general look at ways in which light can be generated. Then the advantages (and drawbacks) of OLEDs are discussed and compared to other established and developing light sources. Second LC lasers are introduced and the motivation behind LC laser research is explained. In the final section the contents of this PhD thesis are explained chapter per chapter.

1.1 Light generation

Light emission or luminescence can be caused in many different ways. Luminescence is often classified by the way it is induced. For example:

- Photoluminescence: induced by light
- Electroluminescent: induced by electrical current
- Chemo-luminescence: induced by chemical reactions
- Bioluminescence: induced by a biological process (usually a chemical reaction taking place inside an organism)
- Sono-luminescence: induced by sound
- Iono-luminescence: induced by ion bombardment (e.g. the aurora borealis)

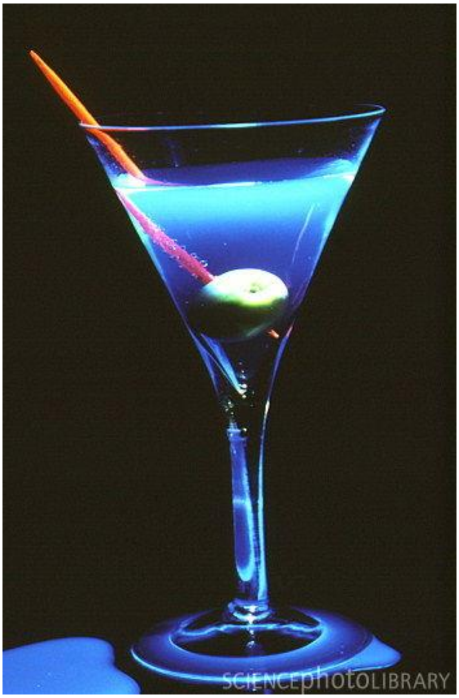

Figure 1.1 An example of luminescent materials. Quinine, an ingredient of tonic, emits a weak blue light when exposed to UV radiation.

These excitation sources all have the effect of bringing a molecule or particle to a higher energy excited state. When the molecule returns to the lower energy ground state, the remaining energy is emitted as a photon.

For applications mainly electroluminescence and photoluminescence are important and only these two will be considered in the remainder of this work. Photoluminescence is a useful and versatile research tool, since it is easily obtained by illuminating the material with a different light ,shorter wavelength , source. The importance of electroluminescence lies obviously in the possibility to make light emitting devices which are driven by electrical power.

A vast number of light emitting materials exist and employ a number of different mechanisms (see above). Since light can be emitted in so many ways from so many materials, many different methods for generating light can be found in nature and technology. Some common examples are: heated Tungsten wires in incandescent lamps, radiation from ionized gas in fluorescent tube lighting, recombination of electron-hole pairs in LEDs and semiconductor lasers, fluorescence from organic molecules like green fluorescent protein in some species of jellyfish, oxidation of luciferin in fireflies... With so many materials and methods to generate light, it is not surprising that many kinds of light emitting devices have been thought of, e.g.: incandescent bulbs, Xenon/Mercury/Sodium lamps, inorganic LEDs, ... An exhaustive discussion of all lighting technologies is outside the scope of this work.

From a concept of operation for a light emitting device to an actual lighting solution for our society a long way has to be travelled. The lighting device has to be understood and optimized , so that the end product can be practical, efficient, safe, affordable,... In this work two light emitting devices that are currently on the route from proof-of-concept to large scale/real world technology are studied, OLEDs and CLC lasers. But first the motivation behind research on OLEDs and CLC lasers is discussed.

1.2 Organic LEDs

Viewed from the outside OLEDs are thin tiles which light up uniformly over the area of the tile. Colours appear natural under illumination by white OLEDs due to their broad spectrum, but OLEDs of any colour can be made. It is even possible to make flexible or transparent OLEDs. All of this makes OLEDs a promising light source for home and office lighting. OLEDs and their working principles are discussed in more detail in Chapter 3

1.2.1 Energy efficiency in OLEDs and other light sources

A very important factor in lighting is the energy efficiency. Around 20% of the worldwide electrical energy consumption is used for lighting. In a push to reduce global energy consumption it is necessary to reduce the energy needed for lighting as well. So more efficient light sources are highly desired. Traditional incandescent light bulbs are already banned in the European Union because of their poor efficiency. OLEDs have the potential to be efficient light sources. Research has already shown that OLEDs can be made with the same or higher efficiency as compact fluorescent tubes, commonly known as “energy saving lamps”[1]. In Table 1 the energy efficiency of several light sources is compared.

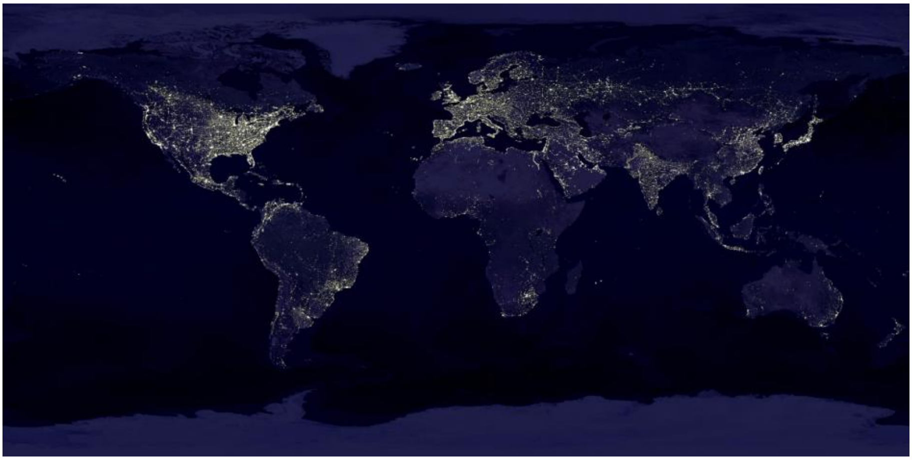

Figure 1.2 Satellite photograph of the earth at night. A classical illustration of the enormous amount of lighting used.

Table 1 Efficiency of various lighting technologies[4].

Technology	*Efficiency range (Lm/W)*
Incandescent	10-18
Halogen	15-20
Compact fluorescent	35-60
Fluorescent tube	50-100
LED	27-92
Metal Halide	50-90

OLED lighting is still in a research stage and a direct comparison with commercial technologies is difficult. Because factors like device lifetime, price, colour rendering, turn-on time, etc. have to be considered too. In Table 2 the efficiencies of some state of the art high-efficiency white OLEDs are given. OLEDs are developing quickly and the record numbers may become outdated soon.

Table 2 Efficiency of state of the art white OLEDs.

Institution/Company	*Reported efficiency (Lm/W)*
Technical University of Dresden	90
Universal display corporation	72
Novaled	60
OLED100-project	>60

Osram	87
Konica Minolta	64

1.2.2 OLED displays

OLED displays are already more developed than OLED lighting. In principle an OLED display is a grid of individual OLEDs next to each other. Each tiny OLED forms a pixel of the display. In recent years OLED displays have been introduced commercially in mobile phones and tablet PCs (see for example Figure 1.3). Several companies have already shown prototypes of OLED televisions and announced they will start selling OLED TVs.

Figure 1.3 A tablet PC with OLED display and a prototype OLED TV. Pictures from [5].

OLED displays have some important advantages over the dominant LCD displays. Because each pixel of an OLED display is an individual light source that is turned off when the pixel should be black, OLED displays have a "deeper" black than LCDs which use a backlight. OLEDs also emit light in all directions and have a very large viewing angle. In LCDs specially engineered compensation films are needed to increase the viewing angle. The switching time of OLEDs is also much faster than that of LCDs.

The energy efficiency of OLED and LCD displays is a matter of some debate. In an OLED only those pixels which have to be on are switched on, the power consumption of OLED displays depends on the image that is shown. For an LCD the backlight is always on and the power consumption is the same for all images. Two comparisons are sometimes made for the energy efficiency of OLED displays and LCDs, one for white images (like a text document or web-page) and one for darker images (like movies).

1.3 Liquid crystal lasers

A second light source investigated in this work is the liquid crystal laser. Laser light is very different from everyday (sun- or other) light. Lasers emit an intense, coherent, monochromatic beam instead of a diffuse, broad-spectrum, distribution of light. Lasers are used for various applications like measuring and sensing, surgery and medicine, precision manufacturing, telecommunication. Several different types of laser exist for all these applications already. Liquid crystal lasers are attractive because they are of microscopic size, tuneable over a broad range and especially cheap to manufacture. Such a cheap tuneable laser opens up many possibilities for all kinds of low cost sensors and laser projectors. Liquid crystal lasers are discussed in-depth in chapter 4.

1.3.1 Liquid crystal lasers: possibilities & state of the art

Lasers are relatively new devices. Although the possibility of a laser was already predicted by Einstein in 1916 [6]. The first working laser was only built in 1960 by Maiman [7]. Since then lasing has been achieved in many different ways.

Liquid crystal lasers are a new class of laser devices which combines some properties of two laser types. The small sizes of semiconductor lasers and tuneability and wide wavelength range of dye lasers. Probably the most interesting is the low fabrication cost of liquid crystal lasers.

Semiconductor lasers differ from other laser because of their miniature dimensions. Most laser systems are an assembly of many bulky components, in a semiconductor lasers all components are integrated on a semiconductor chip. The popular Vertical Cavity Surface Emitting Laser (VCSEL) has an actual laser area of only a few μm^2. In a VCSEL light is emitted perpendicular to the chip surface. The wavelength of emission of semiconductor lasers is determined by the bandgap of the semiconductor gain-material. Typically lasing is only possible in a narrow spectral region in the infra-red (IR).

Traditional dye lasers can achieve lasing over the entire visible range (400-800nm) and near-IR (800-1000nm). The active component of a dye laser is a solution of organic dye molecules in a suitable solvent. Many different laser dyes are available with different emission bands. By combining these dye molecules lasing is obtained in a wide wavelength range. A crucible containing the dye mixture is placed in an optical microcavity formed by two mirrors. The dye mixture is optically pumped by a shorter wavelength laser.

Liquid crystal lasers can be considered a special type of dye lasers with some appealing advantages. They are simple and cheap to produce and are very small. A typical liquid crystal laser is a few μm thin and consist of a single layer of a liquid crystal and laser dye mixture. Liquid crystal laser maintain the tuneability and wide range of wavelengths of conventional dye lasers.

Like VCSELs, liquid crystal lasers are also only a few μm wide and thick and emit light perpendicular to the LC surface. Because of their small dimensions liquid crystal lasers can be integrated on-chip. For example a lab-on-a-chip spectrometry device where a liquid crystal laser, pumped by an external source, is used as an on-chip monochromatic light source could be made. Such a low cost, disposable, measurement device would greatly improve the possibilities for medical diagnostics and other sensing/monitoring applications.

A second area of application for liquid crystal lasers are laser projection displays. Since the three primary colours of a laser display are monochromatic, a very large colour gamut can be achieved in such displays. And due to the nature of the laser beams the image of a laser projector is always in-focus. Liquid crystal lasers are interesting for this application due to their low cost [8]. Up till now laser projection has been hindered by the lack of an affordable fast switching green laser source. An additional advantage is the low speckle of liquid crystal lasers.

1.4 About this work

The next chapters are concerned with modelling the optical behaviour of light emitting devices using the method of plane wave expansion. The focus is on modelling the effects of optical anisotropy and molecular orientation. Each chapter deals with a separate topic.

In chapter 2 the theoretical foundations of the plane wave expansion method for anisotropic thin film microcavities are developed. First some fundamental concepts and notations are introduced. Then the electric field of an oscillating dipole antenna in an infinite anisotropic medium is decomposed as a sum of plane waves. In section 2.3 the effect of embedding the dipole in a microcavity is discussed. The calculation of reflection and transmission in uniaxially anisotropic microcavities is discussed in section 2.4. Finally the change in exciton decay rates by optical effects is explained.

Chapter 3 deals with the optical behaviour of OLEDs. First an overview of the light generation process in an OLED is given together with the key factors determining the efficiency of an OLED. In the rest of chapter 3 outcoupling of light from OLEDs are treated. First for conventional OLEDs with isotropic emitters and then for OLEDs with oriented emitters. The favourable outcoupling behaviour and different decay rate of oriented emitters is discussed in-depth.

The emissive properties of cholesteric liquid crystals (CLCs) are treated in chapter 4. Section 4.1 introduces the basics of cholesteric liquid crystals and liquid crystal lasers. Spontaneous emission from CLCs is discussed in section 4.2. The device is modelled by plane wave expansion and the modelling results are verified by measurements of the spectrum and polarization. A model for stimulated emission and lasing in CLCs is developed in section 4.3. Simulation of the wavelength and polarization of the laser emission as well as the threshold gain required for lasing are explained. The simulated gain and wavelength is compared to experimental findings. Furthermore the effects of pitch, dye spectrum, thickness and orientation order are discussed.

A conclusion and some final remarks are given in chapter 5. Together with some suggestions for further development of both modelling tools, OLED device and liquid crystal lasers.

2. Plane Wave Expansion in uniaxial media

In this chapter the theory of plane wave expansion is explained. First a few important concepts of plane wave optics are introduced (section 2.1). Then the plane wave decomposition of a dipole antenna in a uniaxial anisotropic medium is derived in section 2.2. In section 2.4 the reflection and transmission coefficients of a stack of planar anisotropic layers are calculated. The effects of interference in the cavity on the dipole emission are calculated in section 2.3. The decay rate of excitons is discussed in section 2.5.

2.1 Basics of plane and evanescent waves

2.1.1 Definitions

A plane wave is an electromagnetic wave that extends over all directions with constant amplitude. The phase of a plane wave is constant in a certain infinite plane (see Figure 2.1). The wave propagates in the direction normal to that plane and its phasefronts (surfaces of equal phase) are also parallel infinite planes.

The amplitude of an evanescent wave decreases exponentially. In contrary to a plane wave, an evanescent wave only has a non-zero electric field in a certain part of space.

The electric field of both plane and evanescent waves is written as:

$$\mathbf{E}(x,y,z)=\mathbf{E}_o\exp\left[-j(k_x x+k_y y+k_z z)\right] \tag{1}$$

Omitting the time dependence $\exp(j\omega t)$, ω is the angular frequency of the wave. Each plane or evanescent wave is characterized by its wave-vector $\mathbf{k}$.

$$\mathbf{k}=\begin{bmatrix}k_x & k_y & k_z\end{bmatrix} \tag{2}$$

Using $\nabla\times\mathbf{E}=-j\omega\mu\mathbf{H}$, the magnetic field $\mathbf{H}$ is found:

$$\mathbf{H}(x,y,z)=\frac{\mathbf{k}\times\mathbf{E}_o}{\omega\mu}\exp\left[-j(k_x x+k_y y+k_z z)\right] \tag{3}$$

The amplitude of $\mathbf{k}$ (also called the wavenumber) is given by:

$$k=\omega\sqrt{\mu\varepsilon}=\frac{2\pi}{\lambda}n \tag{4}$$

It can be seen that eq. (1) is indeed a solution of Maxwell's equations by inserting it in the (Fourier transformed w.r.t. t) wave equation:

$$\nabla^2\mathbf{E}+\omega^2\mu\varepsilon\mathbf{E}=0 \tag{5}$$

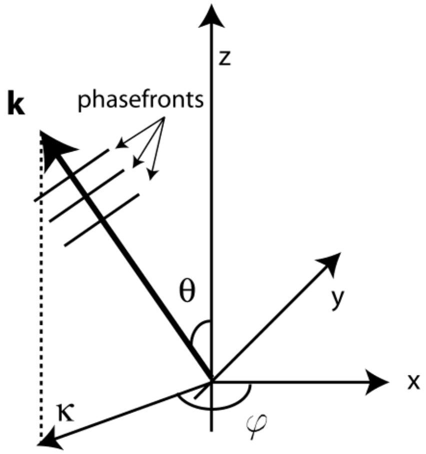

Figure 2.1 The propagation direction of a plane wave is defined by its wavevector $\mathbf{k}$ or by an inclination θ and azimuth φ angle with respect to the z-axis. The phasefronts are parallel planes perpendicular to $\mathbf{k}$.

When we consider an axis system as depicted in Figure 2.1, the propagation direction of the plane wave can be described by an inclination angle θ and azimuth angle φ. The in-plane wave vector $\boldsymbol{\kappa}$ (amplitude κ) is the projection of **k** onto the xy -plane. These quantities may be calculated from **k** using:

$$\kappa = \sqrt{k^2 - k_z^2} \tag{6}$$

$$\sin\theta = \frac{\kappa}{k} \tag{7}$$

$$\tan\varphi = \frac{k_y}{k_x} \tag{8}$$

The power flux carried by plane wave is given by Poyntings vector[9]:

$$\mathbf{S} = \frac{1}{2}\mathrm{Re}\left[\mathbf{E}\times\mathbf{H}^*\right] \tag{9}$$

Where $*$ denotes the complex conjugate. The power flux through a plane is calculated by projecting **S** onto the normal of that plane and multiplying by the surface of that plane.

2.1.2 Propagating and evanescent waves

The amplitude k of the wavevector is given by eq. (4), the in-plane part κ can be any real positive number. When $\kappa > k$ the z-component k_z becomes imaginary.

$$\begin{aligned} k_z &= \sqrt{k^2 - \kappa^2} && \text{for } \kappa < k \\ k_z &= -j\sqrt{\kappa^2 - k^2} && \text{for } \kappa > k \end{aligned} \tag{10}$$

Waves with a real k_z are called propagating waves. Waves with a complex k_z are called evanescent. The electric field of a propagating wave is oscillating with constant amplitude. The electric field of an evanescent wave decreases exponentially with increasing z (see Figure 2.2).

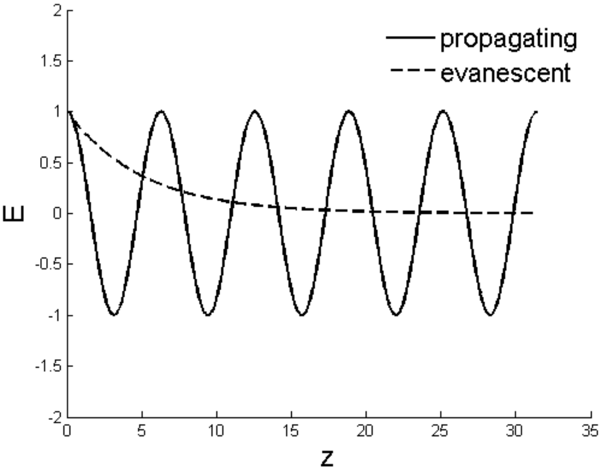

Figure 2.2 Electric field of propagating and evanescent waves. The field of an evanescent wave is non-zero only in a finite region.

A propagating wave extends over the entire medium whereas an evanescent wave is only non-zero in a certain region. In a lossless medium only propagating waves can transfer energy. Evanescent fields create a local electric field that doesn't transfer energy in a lossless medium. In a lossy medium energy can be transferred through the absorption of evanescent waves.

The inclination and azimuth angle (θ and φ) of a propagating wave can be found with eq. (7) and (8). For an evanescent wave only the azimuth φ has physical meaning.

2.1.3 Refraction of a plane wave

When a wave enters a medium with a different refractive index at a flat interface (parallel to the xy-plane), it is refracted according to Snells law. From the viewpoint of plane waves, Snells law states that both k_x and k_y do not change when the wave enters a medium with different refractive index. Snells law is derived from this using Eq. (7).

$$\frac{2\pi}{\lambda} n_1 \sin(\theta_1) = \kappa_1 = \kappa_2 = \frac{2\pi}{\lambda} n_2 \sin(\theta_2) \tag{11}$$

The electric and magnetic field at the interface are subjected to the boundary condition that their components parallel to the interface must be continuous (see e.g. chapter 1 in [10]), this condition will allows to determine the reflection and transmission coefficients at the interface (see section 2.4).

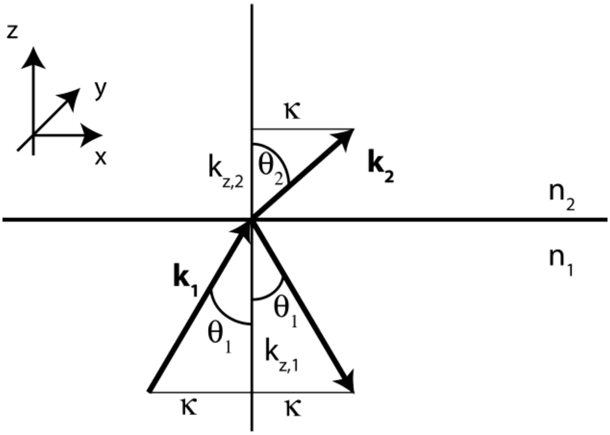

Figure 2.3 The in-plane wave vector is preserved when a plane wave is transmitted/reflected at a plane interface.

A well known consequence of Snell's law is the phenomenon of total internal reflection (TIR). When $n_1 > n_2$ a wave with incidence angle above a critical value $\theta > \theta_{TIR}$ is completely reflected at the interface between the two media. From the perspective of plane waves this occurs when $\kappa > k_2$ and the transmitted wave becomes evanescent (so no power is transmitted).

2.2 Plane wave expansion of a dipole antenna

The cornerstone of the plane wave expansion method is the principle that in a homogeneous medium any monochromatic electric field can be written as a superposition of plane waves [10]. Consider an arbitrary electric field in xyz-coordinates but with a single frequency ω.

In a source free region, $\mathbf{E}$ obeys the wave equation:

$$\nabla^2 \mathbf{E} + \omega^2 \mu \varepsilon \mathbf{E} = 0 \tag{12}$$

The spatial inverse fourier transforms of $\mathbf{E}$ along x, y and z can be taken.

$$\mathbf{A}(k_x, k_y, k_z) = \int_{-\infty}^{+\infty} \int_{-\infty}^{+\infty} \int_{+\infty}^{+\infty} \mathbf{E}(x, y, z) \exp\left[j(k_x x + k_y y + k_z z) \right] \mathrm{d}x\mathrm{d}y\mathrm{d}z \tag{13}$$

The wave equation (eq. (12)) provides a relation between ω and $\mathbf{k}$ so that k_z can be written as a function of ω, k_x and k_y.

$$\mathbf{A}(k_x,k_y)=\int_{-\infty}^{+\infty}\int_{-\infty}^{+\infty}\int_{+\infty}^{+\infty}\mathbf{E}(x,y,z)\exp\left[j(k_x x+k_y y+k_z z)\right]\mathrm{d}x\mathrm{d}y\mathrm{d}z \qquad (14)$$

The original field can be found by performing the fourier transform:

$$\mathbf{E}(x,y,z)=\int_{-\infty}^{+\infty}\int_{-\infty}^{+\infty}\mathbf{A}(k_x,k_y)\exp\left[-j(k_x x+k_y y+k_z z)\right]\mathrm{d}k_x\mathrm{d}k_x \qquad (15)$$

Thus any monochromatic electric field $\mathbf{E}$ can be written as a superposition of its fourier components $\mathbf{A}(k_x,k_y)$. Each fourier component represents a plane or evanescent wave.

The optical behaviour of an entire system can be studied by evaluating the behaviour of each plane wave separately and taking the sum of all plane waves at the end. A problem of particular interest is the radiation of an elementary dipole antenna. Light emission by decay of excited states usually takes place via an electrical dipole transition. The classical electromagnetic problem of a radiating elementary dipole is equivalent to the emission of photons by an ensemble of excited states decaying through an electric dipole transition [11, 12]. In an isotropic medium the plane wave expansion of a dipole is well known and can be found for example in [8, 9].

In a uniaxial anisotropic medium the PWE of an elementary dipole is less known. In this section we will derive the PWE of an elementary dipole antenna in a uniaxial anisotropic medium. Only the essential steps of the derivation are given here. A detailed calculation can be found in Appendix A. An expression for the field of a dipole of arbitrary orientation in a uniaxial medium with arbitrary orientation of the optical axis is derived. Such a general formulation is preferred here in order to easily combine the plane wave expansion formulas with thin film cavities. The dipole field can be found in a more elegant way by the scaling procedure of Clemmow [13]. This scaling requires a specific choice of coordinate system and dipole orientation. It can be shown that the results obtained by both methods are in agreement.

2.2.1 Definitions and notations

A uniaxial medium is characterized by the orientation of the optical axis $\mathbf{c}$ and the two eigenvalues of the dielectric tensor $\varepsilon_\perp$ and $\varepsilon_\parallel$, where $\varepsilon_\perp$ and $\varepsilon_\parallel$

are the eigenvalues respectively in a plane perpendicular (ordinary polarization) and parallel (extra- ordinary polarization) to $\mathbf{c}$. The orientation of $\mathbf{c}$ is also determined by an inclination angle β and azimuth angle γ. A sketch of the coordinate system is presented in Figure 2.4.

The dielectric tensor $\overset{=}{\varepsilon}$ becomes a diagonal tensor if we choose a basis along the principal axes of the material. When $\mathbf{z} \parallel \mathbf{c}$ $\overset{=}{\varepsilon}$ is given by Eq. (16) . The ordinary n_o and extra-ordinary n_e refractive index is then defined below. ε_0 is the dielectric permittivity of vacuum.

$$\overset{=}{\varepsilon} = \begin{bmatrix} \varepsilon_\perp & 0 & 0 \\ 0 & \varepsilon_\perp & 0 \\ 0 & 0 & \varepsilon_{||} \end{bmatrix} \tag{16}$$

$$n_o = \sqrt{\frac{\varepsilon_\perp}{\varepsilon_0}} \tag{17}$$

$$n_e = \sqrt{\frac{\varepsilon_{||}}{\varepsilon_0}} \tag{18}$$

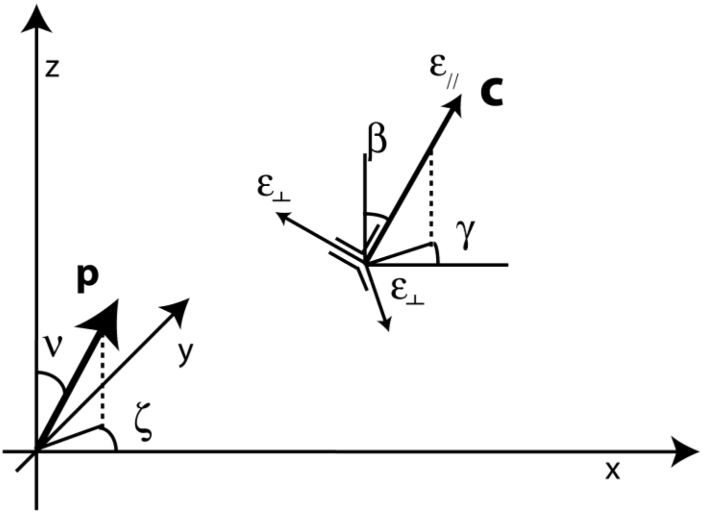

Figure 2.4 Orientation of the optical axis $\mathbf{c}$ and the dipole moment $\mathbf{p}$.

The orientation of the dipole moment $\mathbf{p}$ is defined by an inclination angle ν (with respect to the z-axis) and an azimuth angle ζ in the xy-plane. We choose the origin of the xyz-system to coincide with the location of the dipole.

For uniaxial anisotropic media there is a different refractive index for the ordinary polarized waves n_o and extra ordinary polarized waves n_e. The electric field of the ordinary polarization is perpendicular to $\mathbf{c}$, the extra-ordinary polarization has an electric field component parallel to $\mathbf{c}$. The value of n_o is the same for every direction in the medium but n_e depends on the direction of propagation. The wave-vector can also be written as a sum of a part perpendicular $\mathbf{k}_\perp$ and a part parallel $\mathbf{k}_\parallel$ to $\mathbf{c}$. In anisotropic media k is different for ordinary and extra-ordinary polarized waves $k_{e/o} = 2\pi n_{e/o} / \lambda$, the z-component can be found with $k_{z,e/o} = \sqrt{k_{e/o}^2 - \kappa^2}$. From eq. (7) we can see that the ordinary and extra-ordinary waves with the same κ propagate with different θ.

Throughout the next chapters the subscripts $\parallel$, $\perp$ and z are used to denote components respectively parallel to $\mathbf{c}$, perpendicular to $\mathbf{c}$ and parallel to z.

2.2.2 Scalar Hertz potentials

The electric field of the dipole antenna is a solution to Maxwells equation. We will solve Maxwells equations following the approach given in [14]. First we rewrite the equations using scalar Hertz potentials and then insert the appropriate source terms for an elementary dipole.

$$\nabla.(\overset{=}{\varepsilon}\mathbf{E}) = \rho \tag{19}$$

$$\nabla \times \mathbf{E} = -\frac{\partial \mu \mathbf{H}}{\partial t} \tag{20}$$

$$\nabla.(\mu \mathbf{H}) = 0 \tag{21}$$

$$\nabla \times \mathbf{H} = \frac{\partial (\overset{=}{\varepsilon}\mathbf{E})}{\partial t} + \mathbf{J} \tag{22}$$

In our case the only source is an oscillating elementary dipole and the corresponding charge density ρ and current density $\mathbf{J}$ are given by:

$$\rho = -\nabla \cdot \mathbf{p}\delta(\mathbf{r}) \tag{23}$$

$$\mathbf{J} = \frac{\partial \mathbf{p}}{\partial t}\delta(\mathbf{r}) \tag{24}$$

We split all vector quantities ($\mathbf{E}$, $\mathbf{H}$, $\mathbf{J}$ and ∇) in their components parallel and perpendicular to $\mathbf{c}$.

$$\mathbf{E} = \mathbf{E}_{\perp} + E_{\|}\mathbf{c} \tag{25}$$

$$\mathbf{H} = \mathbf{H}_{\perp} + H_{\|}\mathbf{c} \tag{26}$$

$$\mathbf{J} = \mathbf{J}_{\perp} + J_{\|}\mathbf{c} \tag{27}$$

$$\nabla = \nabla_{\perp} + \frac{\partial}{\partial c}\mathbf{c} \tag{28}$$

In this coordinate system $\overline{\overline{\varepsilon}}$ is a diagonal tensor and :

$$\overline{\overline{\varepsilon}}\mathbf{E} = \varepsilon_{\perp}\mathbf{E}_{\perp} + \varepsilon_{\|}E_{\|}\mathbf{c} \tag{29}$$

We now express the four components of the perpendicular fields (two components of $\mathbf{E}_{\perp}$ and two of $\mathbf{H}_{\perp}$) using four scalar potentials Φ, Θ, Π and Ψ.

$$\mathbf{E}_{\perp} = \nabla_{\perp}\Phi + \nabla_{\perp} \times (\Theta\mathbf{c}) \tag{30}$$

$$\mathbf{H}_{\perp} = \nabla_{\perp}\Pi + \nabla_{\perp} \times (\Psi\mathbf{c}) \tag{31}$$

Using these potentials the vector equations (20) and (22) can be rewritten as six scalar equations (see Appendix A Eq. (185)-(186) and (199)-(202)).The auxiliary functions u and v are introduced:

$$\nabla_{\perp}^2 u = \nabla_{\perp} \cdot \mathbf{J}_{\perp} \tag{32}$$

$$\nabla_{\perp}^2 v = -\mathbf{c} \cdot \left(\nabla_{\perp} \times \mathbf{J}_{\perp}\right) \tag{33}$$

A system of uncoupled differential equation is obtained for Θ and Ψ (Eq. 74 and 75 in [14]) by substitution in this system of six equations:

$$\nabla_{\perp}^2\Theta + \frac{\partial^2\Theta}{\partial c^2} - \mu\varepsilon_{\perp}\frac{\partial^2\Theta}{\partial t^2} = \mu\frac{\partial v}{\partial t} \tag{34}$$

$$-\nabla_{\perp}^2\Psi - \frac{\varepsilon_{\|}}{\varepsilon_{\perp}}\frac{\partial^2\Psi}{\partial c^2} + \mu\varepsilon_{\|}\frac{\partial^2\Psi}{\partial t^2} = -\frac{\varepsilon_{\|}}{\varepsilon_{\perp}}\frac{\partial u}{\partial c} + J_{\|} \tag{35}$$

A single oscillating dipole antenna imposes the following current:

$$\mathbf{J} = \frac{\partial \mathbf{p}}{\partial t}\delta(\mathbf{r}) \tag{36}$$

And corresponding expressions for $J_{\|}$, u and v.

$$\mathbf{J}_{\|} = \frac{\partial \mathbf{p}_{\|}}{\partial t}\delta(\mathbf{r}) \tag{37}$$

$$\nabla_{\perp}^{2} u = \nabla_{\perp}\cdot\frac{\partial \mathbf{p}_{\perp}}{\partial t}\delta(\mathbf{r}) \tag{38}$$

$$\nabla_{\perp}^{2} v = -\mathbf{c}\cdot\left(\nabla_{\perp}\times\frac{\partial \mathbf{p}_{\perp}}{\partial t}\delta(\mathbf{r})\right) \tag{39}$$

2.2.3 Solution via Fourier domain

A solution for Θ and Ψ can be found by performing a spatial and temporal Fourier transform on Eq. (34) to (39). Using the relations: $\partial/\partial t \rightarrow j\omega$, $\partial/\partial c \rightarrow -jk_{\|}$ and $\nabla_{\perp} \rightarrow -j\mathbf{k}_{\perp}$, an expression for Θ and Ψ in the Fourier domain can be easily derived:

$$\Theta = \frac{j\mu\omega^{2}}{k_{\perp}^{2}}\frac{\mathbf{c}\cdot\left(\mathbf{k}_{\perp}\times\mathbf{p}_{\perp}\right)}{-k_{\perp}^{2}-k_{\|}^{2}+\mu\varepsilon_{\perp}\omega^{2}} \tag{40}$$

$$\Psi = \frac{j\dfrac{\omega k_{\|}}{k_{\perp}^{2}}(\mathbf{k}_{\perp}\cdot\mathbf{p}_{\perp}) - j\dfrac{\varepsilon_{\perp}}{\varepsilon_{\|}}\omega p_{\|}}{-\dfrac{\varepsilon_{\perp}}{\varepsilon_{\|}}k_{\perp}^{2}-k_{\|}^{2}+\mu\varepsilon_{\perp}\omega^{2}} \tag{41}$$

From the scalar Hertz potentials Θ and Ψ the remaining quantities $E_{\|}$ and Φ can be found (by performing the Fourier transform of respectively Eq. (204) and (201)). With this information and eq. (25) and (30) we can write an expression for $\mathbf{E}$ in the fourier domain.

$$\begin{aligned}\mathbf{E}(\mathbf{k}) = {} & \frac{\dfrac{\mathbf{k}}{\varepsilon_{\|}}(\mathbf{k}\cdot\mathbf{p})-\mathbf{k}_{\perp}(\mathbf{k}_{\perp}\cdot\mathbf{p}_{\perp})\dfrac{\mu\omega^{2}}{k_{\perp}^{2}}-\dfrac{\mu\varepsilon_{\perp}}{\varepsilon_{\|}}\omega^{2}p_{\|}\mathbf{c}}{-\dfrac{\varepsilon_{\perp}}{\varepsilon_{\|}}k_{\perp}^{2}-k_{c}^{2}+\mu\varepsilon_{\perp}\omega^{2}} \\ & -j\mathbf{k}_{\perp}\times\left[\frac{j\mu\omega^{2}}{k_{\perp}^{2}}\frac{\mathbf{c}\cdot\left(\mathbf{k}_{\perp}\times\mathbf{p}_{\perp}\right)}{-k_{\perp}^{2}-k_{\|}^{2}+\mu\varepsilon_{\perp}\omega^{2}}\right]\mathbf{c}\end{aligned} \tag{42}$$

Eq. (42) can be split in two different terms. The first term is called the extraordinary field $\mathbf{E}_e$ and the second term is the ordinary field $\mathbf{E}_o$.

$$\mathbf{E}_e = \frac{\frac{\mathbf{k}}{\varepsilon_{||}}\left(\mathbf{k}\cdot\mathbf{p}\right)-\mathbf{k}_{\perp}\left(\mathbf{k}_{\perp}\cdot\mathbf{p}_{\perp}\right)\frac{\mu\omega^2}{k_{\perp}^2}-\frac{\mu\varepsilon_{\perp}}{\varepsilon_{||}}\omega^2 p_{||}\mathbf{c}}{-\frac{\varepsilon_{\perp}}{\varepsilon_{||}}k_{\perp}^2-k_c^2+\mu\varepsilon_{\perp}\omega^2} \tag{43}$$

$$\mathbf{E}_o = -j\mathbf{k}_{\perp}\times\left[\frac{j\mu\omega^2}{k_{\perp}^2}\frac{\mathbf{c}\cdot\left(\mathbf{k}_{\perp}\times\mathbf{p}_{\perp}\right)}{-k_{\perp}^2-k_{||}^2+\mu\varepsilon_{\perp}\omega^2}\right]\mathbf{c} \tag{44}$$

2.2.4 Coordinate transformation and inverse fourier transform

Eq. (42) expresses the electric field of a dipole antenna in the coordinate system along the principal axes. The electric field in an arbitrary xyz-system is found by expressing all quantities using their xyz-components. The wave vector obeys the following equations:

$$k = k_{\perp}^2 + k_{||}^2 = \kappa^2 + k_z^2 \tag{45}$$

$$\mathbf{k} = \mathbf{k}_{\perp} + \mathbf{k}_{||} = \boldsymbol{\kappa} + \mathbf{k}_z \tag{46}$$

2.2.4.1 Plane wave expansion of the ordinary field

We can rewrite the denominator of eq. (44) by inserting eq. (45).

$$\mathbf{E}_o(\mathbf{k}) = -j\mathbf{k}_{\perp}\times\frac{j\mu\omega^2}{k_{\perp}^2}\frac{\mathbf{c}\cdot\left(\mathbf{k}_{\perp}\times\mathbf{p}_{\perp}\right)}{-k_z^2+\mu\varepsilon_{\perp}\omega^2-\kappa^2}\mathbf{c} \tag{47}$$

The electric field in xyz-space is found by performing the inverse fourier transform of eq.(47).

$$\mathbf{E}_o = \frac{\mu\omega^2}{8\pi^3}\int_{-\infty}^{+\infty}\int_{-\infty}^{+\infty}\int_{-\infty}^{+\infty} dk_x dk_y dk_z \left\{-j\mathbf{k}_{\perp}\times\frac{j}{k_{\perp}^2}\frac{\left[\mathbf{c}\cdot\left(\mathbf{k}_{\perp}\times\mathbf{p}_{0,\perp}\right)\right]\mathbf{c}}{-k_{\perp}^2-k_c^2+\mu\varepsilon_{\perp}\omega^2}\right\} \exp\left[-j(k_x x+k_y y+k_z z)\right] \tag{48}$$

Only the inverse Fourier transform along the variable k_z is explicitly calculated to obtain the plane wave decomposition $\mathbf{E}_o(k_x,k_y)$. The complex integral in the inverse fourier transform can be solved using the Cauchy residue theorem. Finally the following equation is obtained for $z > 0$ and $\kappa < \omega^2 \mu \varepsilon_\perp$.

$$\mathbf{E}_o = \frac{-j\mu\omega^2}{8\pi^2} \int_{-\infty}^{+\infty} \int_{-\infty}^{+\infty} dk_x dk_y \frac{\left[\mathbf{c} \cdot \left(\mathbf{k}_\perp \times \mathbf{p}_\perp\right)\right]}{k_{z,o}} \frac{\mathbf{k}_\perp \times \mathbf{c}}{k_\perp^2} \exp\left[-j(k_x x + k_y y + k_{z,o} z)\right] \quad (49)$$

Where $k_{z,o} = \sqrt{\omega^2 \mu \varepsilon_\perp - \kappa^2}$, like in eq. (10) for isotropic media. When $z < 0$ a different contour must be chosen for the integration but the resulting formula is is identical to eq. (49) when the negative root is taken for $k_{z,o}$. The orientation of the ordinary field $\mathbf{E}_o$ is then:

$$\mathbf{1}_o = \frac{\mathbf{k} \times \mathbf{c}}{\left|\mathbf{k} \times \mathbf{c}\right|} \quad (50)$$

For all ordinary waves: $\mathbf{1}_o \perp \mathbf{c}$.

2.2.4.2 Plane wave expansion of the extra-ordinary field

The same procedure can be applied to eq. (43) for the $\mathbf{E}_e$ term. For the extra ordinary polarization the poles are no longer independent of the direction of $\mathbf{k}$. For $z > 0$, $k_{z,e}$ becomes:

$$k_{z,e} = \frac{\sqrt{\mu \varepsilon_\perp \varepsilon_{||} (\varepsilon_\perp + \Delta\varepsilon c_z^2)\omega^2 - \kappa^2 \varepsilon_\perp \left[\varepsilon_\perp + \Delta\varepsilon(c_z^2 + c_t^2)\right]}}{\varepsilon_\perp + \Delta\varepsilon c_z^2} - \frac{\Delta\varepsilon c_t c_z \kappa}{\varepsilon_\perp + \Delta\varepsilon c_z^2} \quad (51)$$

With $\Delta\varepsilon = \varepsilon_{||} - \varepsilon_\perp$, $c_t = \mathbf{c} \cdot \boldsymbol{\kappa}$ and $c_z = \mathbf{c} \cdot \mathbf{z}$. From eq. (51) we can see that for the extra-ordinary polarization the poles depend on the orientation of $\mathbf{k}$ and $\mathbf{c}$. The inverse fourier transform can be performed for $\mathbf{E}_e$ (for $z > 0$).

$$\mathbf{E}_e = \frac{-j}{8\pi^2} \int_{-\infty}^{+\infty} \int_{-\infty}^{+\infty} dk_x dk_y \frac{\mathbf{k}_\perp - \dfrac{k_\perp^2 \varepsilon_\perp}{k_{||}^2 \varepsilon_{||}} \mathbf{k}_{||}}{\dfrac{\varepsilon_\perp + \Delta\varepsilon c_z^2}{\varepsilon_{||}} \left(k_{z,e} + \dfrac{\Delta\varepsilon c_t c_z \kappa}{\varepsilon_\perp + \Delta\varepsilon c_z^2}\right)} \left[\frac{k_{||} p_{||}}{\varepsilon_{||}} - \frac{k_{||}^2 \left(\mathbf{k}_\perp \cdot \mathbf{p}_\perp\right)}{k_\perp^2 \varepsilon_\perp}\right] \exp\left[-j(k_x x + k_y y + k_{z,e} z)\right] \quad (52)$$

Only the inverse Fourier transform along the variable k_z is explicitly calculated to obtain the plane wave decomposition $\mathbf{E}_e(k_x, k_y)$. When $z < 0$ a different contour must be chosen for the integration but the resulting formula is identical to eq.(52) when the negative root is taken in eq. (51). for $k_{z,e}$ .The unit vector of the extra ordinary polarization is:

$$\mathbf{1}_{\mathbf{e}} = \frac{\mathbf{k}_{\perp} - \dfrac{\mathbf{k}_{\perp}^{2}\boldsymbol{\varepsilon}_{\perp}}{\mathbf{k}_{\|}\boldsymbol{\varepsilon}_{\|}}\mathbf{c}}{\left|\mathbf{k}_{\perp} - \dfrac{\mathbf{k}_{\perp}^{2}\boldsymbol{\varepsilon}_{\perp}}{\mathbf{k}_{\|}\boldsymbol{\varepsilon}_{\|}}\mathbf{c}\right|} \tag{53}$$

Which can have both a component parallel and perpendicular to $\mathbf{c}$, as expected for the extra-ordinary polarization.

2.3 Dipole radiation inside microcavities

The radiation of a dipole inside a microcavity can be very different from that of a dipole in an infinite medium. Microcavities allow enhancing or decreasing the dipole radiation in a chosen direction.

The change in dipole radiation is caused by interference between the emitted field and its reflections on nearby interfaces. When a dipole is inside a layer structure each layer interface will give rise to reflections. When the emitted and reflected field are in phase, the electric field at the dipole location is enhanced (constructive interference). When the emitted and reflected field are out of phase, the electric field at the dipole location is decreased (destructive interference).

From the viewpoint of light emission by decay of excited states (from state s to state f), the power emitted with a certain wavevector k is given by Fermi’s golden rule [12, 13]. Where $\rho(k)$ (unit m) is a distribution over all wavevectors (and thus frequencies) the excited state can emit.

$$P(k) = \frac{2\pi\omega}{c\hbar}\left| < f\,|\,\mathbf{p}\,|\,s > .\mathbf{E}(k)\right|^{2} \rho(k) \tag{54}$$

Where $< f\,|\,\mathbf{p}\,|\,s >$ is the transition dipole moment. The electric field $\mathbf{E}(k)$ is an integral over the plane wave contributions (k_x, k_y) covering all space angles of emission [15].

$$P(k) = \iint dk_x dk_y \frac{2\pi\omega}{c\hbar}\left| < f\,|\,\mathbf{p}\,|\,s > .\mathbf{A}(k_x, k_y)\right|^{2} \rho(k) \tag{55}$$

From eq. (54) it is seen that if $\mathbf{E}$ is increased at the dipole position, the emitted power is also increased. This is consistent with the equivalence between a classical dipole antenna and an ensemble of excited states decaying via electric dipole transitions.

2.3.1 Multiple beam & wide angle interference

Interference effects can be divided in two categories: multiple beam interference (MBI) and wide angle interference (WAI). A schematic representation of the two is given in Figure 2.5.

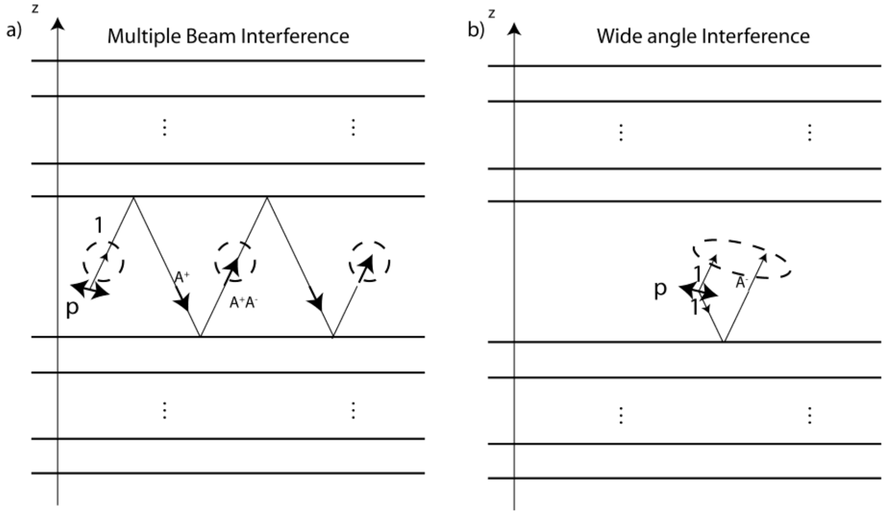

Figure 2.5 a) Multiple beam interference between the infinite reflections between two interfaces. b) Wide angle interference between a wave and the reflection of a wave with the same k_x and k_y.

MBI is the result of reflections of the same wave between two interfaces (see Figure 2.5a). The wave is partly reflected at the top interface and then propagates (in the –z direction) through the layer to the bottom interface where it is again reflected. Again the wave propagates (in the +z direction) through the layer and is reflected at the top interface and so on. The sum of the infinite number of reflections is known as MBI.

WAI occurs between a wave travelling in the +z direction (in Figure 2.5b) and the reflection of a second wave with equal k_x and k_y,which was travelling in the opposite direction prior to reflection.. Constructive interference is seen for those angles where the reflection of the second wave is in phase with the first wave. Since the optical path length depends on the angle, there is constructive interference for some angles and destructive interference for others.

In a cavity both WAI and MBI are observed. Which of the two processes is most important depends on the lay-out of the cavity. When two highly reflecting surfaces are present, one on each side of the cavity, MBI can become strong because the many reflections only slowly decrease in amplitude. When only one side of the cavity is significantly reflecting WAI will be more important.

2.3.2 Radiation of a dipole in a cavity

2.3.2.1 Isotropic cavities

For isotropic microcavities a model for dipole radiation based on plane wave decomposition was developed by Lukosz [16] and has been applied to simulate a wide range of applications [17]. The starting point of Lukosz' method is the plane wave decomposition of the field of a dipole antenna in an infinite medium [18]. The electric field of the dipole in an infinite medium is then altered by WAI and MBI. The various reflected waves are represented in Figure 2.6.

The combined reflections lead to the following formula for the amplitudes $E_{cav,TE/TM}$ of the TE and TM waves in an isotropic microcavity based on the amplitude E_∞ of the dipole field in an infinite medium (found with Eq. (49) and (52)) and the complex field reflection coefficients of the top and bottom parts of the cavity A^+ and A^-:

$$E^+_{cav,TE/TM} = \frac{E^+_{\infty,TE/TM} + A^-_{TE/TM} E^-_{\infty,TE/TM}}{1 - A^+_{TE/TM} A^-_{TE/TM}} \tag{56}$$

$$E^-_{cav,TE/TM} = \frac{E^-_{\infty,TE/TM} + A^+_{TE/TM} E^+_{\infty,TE/TM}}{1 - A^-_{TE/TM} A^+_{TE/TM}} \tag{57}$$

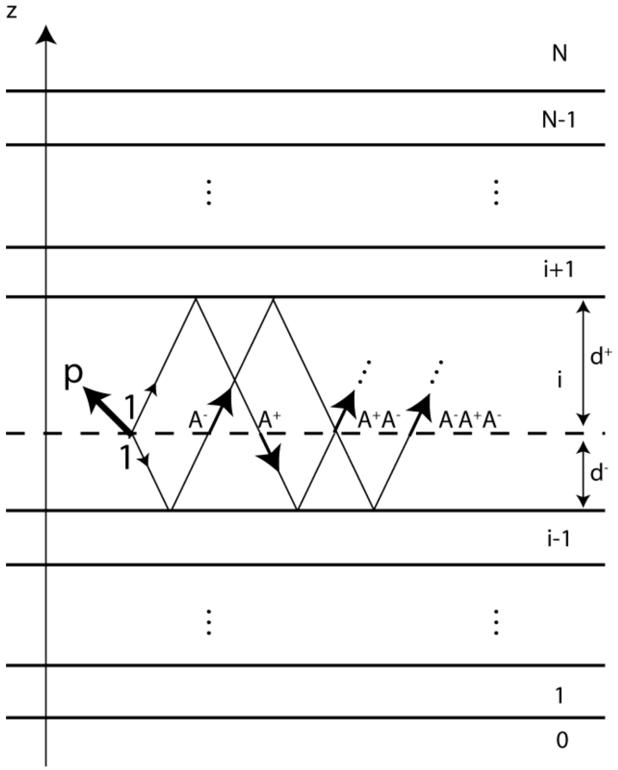

Figure 2.6 A stack of anisotropic films with a dipole antenna $\mathbf{p}$. The dipole radiation is modified by interference with reflections of the cavity interfaces above and below the dipole.

The numerator $E_\infty^{+/-} + A^{-/+} E_\infty^{-/+}$ of equations (56) and (57) expresses WAI. The denominator $1 - A^{+}_{TE/TM} A^{-}_{TE/TM}$ expresses MBI.

In an isotropic medium $A^\pm$ and $E_\infty^\pm$ are different for the transverse magnetic (TM) and transverse electric (TE) polarization, but coupling between TE and TM waves does not occur. A separate calculation can be done for each polarization. The reflection coefficients $A^\pm$ express both the reflection at interfaces and phase changes due to propagation through the layers.

The power flux through the plane $z = 0$ can be found by taking the z-component of the Poynting vector (Eq. (9)). The power flux K per κ^2 (unit m^2) for a dipole parallel to z (vertical) or the xy-plane (horizontal) is given by Eq. (58)-(61) [17], normalized by the emission of a dipole in an infinite medium.

$$K^{TM}_{vertical,\lambda}(\kappa,\lambda)=\frac{3}{4}\mathrm{Re}\left[\frac{\kappa^2}{k_i^3 k_{z,i}}\frac{\left(1+A^+_{TM}\right)\left(1+A^-_{TM}\right)}{1-A^+_{TM}A^-_{TM}}\right] \tag{58}$$

$$K^{TE}_{vertical,\lambda}(\kappa,\lambda)=0 \tag{59}$$

$$K^{TM}_{horizontal,\lambda}(\kappa,\lambda)=\frac{3}{8}\mathrm{Re}\left[\frac{k_{z,i}}{k_i^3}\frac{\left(1-A^+_{TM}\right)\left(1-A^-_{TM}\right)}{1-A^+_{TM}A^-_{TM}}\right] \tag{60}$$

$$K^{TE}_{horizontal,\lambda}(\kappa,\lambda)=\frac{3}{8}\mathrm{Re}\left[\frac{1}{k_i k_{z,i}}\frac{\left(1+A^+_{TE}\right)\left(1+A^-_{TE}\right)}{1-A^+_{TE}A^-_{TE}}\right] \tag{61}$$

These equations do not depend on the azimuth of the wave φ or the dipole ς, because the isotropic cavity is invariant to rotation around the z-axis. The formulas for horizontal dipoles (Eq. (60) and (61)) are an average for a uniform distribution of dipoles in the xy-plane. Also note that the emission of a vertical dipole is purely TM polarized.

2.3.2.2 Anisotropic cavities

For an anisotropic microcavity a similar method can be applied to calculate the radiation of a dipole in the cavity. The eigenmodes of uniaxial materials are two linearly polarized waves, the ordinary (o) and the extraordinary (e) wave (instead of the TE and TM polarization). The normalized fields ($\mathbf{1}_o$ and $\mathbf{1}_e$) of the eigenmodes are given by Eq. (50) and (53). The complex amplitude $E^+_{\infty,e/o}$ of each mode in an infinite medium is given by Eq. (49) and (52). The amplitude $E^-_{\infty,e/o}$ of modes travelling in the $-z$ direction is found with the corresponding expression for $z<0$. The total polarization state of the light is determined by the complex amplitudes of the ordinary and extraordinary waves and their difference in phase.

In anisotropic media e- and o-waves are coupled when reflection or transmission at an interface takes place. Therefore the reflection coefficients have to be replaced by reflection matrices. One must be careful to simulate all changes in polarization that occur during propagation, reflection and transmission in an anisotropic cavity. Eq. (56) and (57) should be replaced by:

$$\begin{bmatrix} E^{+}_{cav,o} \\ E^{+}_{cav,e} \end{bmatrix} = \left(1 - \overline{\overline{A^{-}}}\,\overline{\overline{A^{+}}}\right)^{-1} \left(\begin{bmatrix} E^{+}_{\infty,o} \\ E^{+}_{\infty,e} \end{bmatrix} + \overline{\overline{A^{-}}} \begin{bmatrix} E^{-}_{\infty,o} \\ E^{-}_{\infty,e} \end{bmatrix} \right) \tag{62}$$

$$\begin{bmatrix} E^{-}_{cav,o} \\ E^{-}_{cav,e} \end{bmatrix} = \left(1 - \overline{\overline{A^{+}}}\,\overline{\overline{A^{-}}}\right)^{-1} \left(\begin{bmatrix} E^{-}_{\infty,o} \\ E^{-}_{\infty,e} \end{bmatrix} + \overline{\overline{A^{+}}} \begin{bmatrix} E^{+}_{\infty,o} \\ E^{+}_{\infty,e} \end{bmatrix} \right) \tag{63}$$

The reflection matrices $\overline{\overline{A^{\pm}}}$ are 2x2 matrices describing the coupling upon reflection between the ordinary and extra-ordinary polarized waves.

$$\overline{\overline{A^{\pm}}} = \begin{bmatrix} A^{\pm}_{oo} & A^{\pm}_{eo} \\ A^{\pm}_{oe} & A^{\pm}_{ee} \end{bmatrix} \tag{64}$$

where A_{lm} is the amplitude reflection coefficient for an incoming wave with polarization l into a reflected wave with polarization m. For isotropic layer stacks o- and e-waves are uncoupled ($\mathrm{A}_{eo} = \mathrm{A}_{oe} = 0$) and Eq. (62) and (63) become identical to (56) and (57) respectively.

The field amplitudes emitted to the outside layer (N or 0) E_{out} can be calculated from E_{cav}:

$$\begin{bmatrix} E^{\pm}_{out,o} \\ E^{\pm}_{out,e} \end{bmatrix} = \overline{\overline{T^{\pm}}} \begin{bmatrix} E^{\pm}_{cav,o} \\ E^{\pm}_{cav,e} \end{bmatrix} \tag{65}$$

$\overline{\overline{T^{\pm}}}$ is a 2x2 matrix which describes the transmission of waves like $\overline{\overline{A^{\pm}}}$ describes the reflection. Starting from E_{out} the corresponding magnetic field H_{out} ($-j\mathbf{k}\times\mathbf{E}_{\mathbf{e/o}} = -j\omega\mu\mathbf{H}_{\mathbf{e/o}}$) and Poynting vector (Eq. (9)) can be calculated.

2.4 Reflection and transmission of anisotropic thin film stacks

With formula (62) and (63) the radiation of a dipole in anisotropic 1D microcavities can be calculated provided that the reflection matrices $\overline{\overline{A^{\pm}}}$ of the microcavity are known. This section shows how to obtain the reflection and transmission matrices of a stack of uniaxially anisotropic films using the scattering matrix approach introduced by Ko [19]. Alternatively the Berreman 4x4 matrix method [20] can be used. We have chosen the scattering matrix method because it is numerically more stable when dealing with evanescent waves and total internal reflection.

The scattering matrix method calculates a 4x4 scattering matrix $\overline{\overline{S_{iN}}}$ that relates incoming waves to the outgoing waves (see Figure 2.7). There are four incoming waves: two in layer i travelling upward $\left[\mathrm{E}_{o,i,+}, \mathrm{E}_{e,i,+}\right]$ and two in the top layer N travelling downward $\left[\mathrm{E}_{o,N,-}, \mathrm{E}_{e,N,-}\right]$. And four outgoing waves: two outgoing waves in the top layer N travelling upward $\left[\mathrm{E}_{o,N,+}, \mathrm{E}_{e,N,+}\right]$ and two in the layer i travelling downward $\left[\mathrm{E}_{o,i,-}, \mathrm{E}_{e,i,-}\right]$. $\overline{\overline{S_{iN}}}$ is a block matrix consisting of four 2x2 matrices.

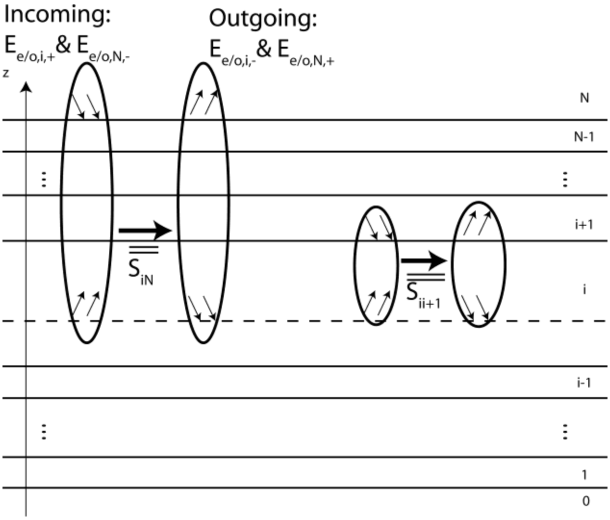

Figure 2.7 Sketch of the input-output relation of the scattering matrices. $\overline{\overline{S_{iN}}}$ is constructed by step by step addition of layers to $\overline{\overline{S_{ii}}}$.

$$\begin{pmatrix} E_{o,N,+} \\ E_{e,N,+} \\ E_{o,i,-} \\ E_{e,i,-} \end{pmatrix} = \overline{\overline{S_{iN}}} \begin{pmatrix} E_{o,i,+} \\ E_{e,i,+} \\ E_{o,N,-} \\ E_{e,N,-} \end{pmatrix} \tag{66}$$

Once the matrix $\overline{\overline{S_{iN}}}$ is determined, the reflection matrix $\overline{\overline{A^{+}}}$ and the transmission matrix $\overline{\overline{T^{+}}}$ can be identified. $\overline{\overline{A^{+}}}$ and $\overline{\overline{T^{+}}}$ link the outgoing waves to $E_{o,i,+}$ and $E_{e,i,+}$.

$$\overline{\overline{T^{+}}} = \overline{\overline{S_{iN,11}}} \tag{67}$$

$$\overline{\overline{A^{+}}} = \overline{\overline{S_{iN,21}}} \tag{68}$$

An analogous procedure is used to determine $\overline{\overline{A}}^{-}$ and $\overline{\overline{T}}^{-}$.

The scattering matrix of an entire stack $\overline{\overline{S_{iN}}}$ can be built by starting from $\overline{\overline{S_{ii}}}$ which is equal to the unity matrix and then adding extra layers step by step. When the matrices $\overline{\overline{S_{ij}}}$ and $\overline{\overline{I_j}}$ are known , the scattering matrix $\overline{\overline{S_{ij+1}}}$ of a stack with an additional layer can be calculated [19]. $\overline{\overline{I_j}}$ relates the fields above the (j+1)/j interface to the fields above the interface j/(j-1) (see Figure 2.8).

$$\begin{pmatrix} E_{o,j+1,+} \\ E_{e,j+1,+} \\ E_{o,j+1,-} \\ E_{e,j+1,-} \end{pmatrix} = \overline{\overline{I_j}} \begin{pmatrix} E_{o,j,+} \\ E_{e,j,+} \\ E_{o,j,-} \\ E_{e,j,-} \end{pmatrix} \tag{69}$$

Note that this definition of $\overline{\overline{I_j}}$ is the inverse of $\overline{\overline{I_j}}$ as defined in ref. [19], consequentially formulas (72)-(75) are identical to the formulas given in [19] except for the inverse of $\overline{\overline{I_j}}$.Multiplying eq. (69) by $\overline{\overline{I_j}}^{-1}$ yields an expression of the fields $\left[\mathrm{E}_{o,j,+},\ \mathrm{E}_{e,j,+}\right]$ and $\left[\mathrm{E}_{o,j,-},\ \mathrm{E}_{e,j,-}\right]$ in layer j in function of the fields in the next layer $(j+1)$ ($\left[\mathrm{E}_{o,j+1,+},\ \mathrm{E}_{e,j+1,+}\right]$ and $\left[\mathrm{E}_{o,j+1,-},\ \mathrm{E}_{e,j+1,-}\right]$).

$$\begin{pmatrix} E_{o,j,+} \\ E_{e,j,+} \\ E_{o,j,-} \\ E_{e,j,-} \end{pmatrix} = \overline{\overline{I_j}}^{-1} \begin{pmatrix} E_{o,j+1,+} \\ E_{e,j+1,+} \\ E_{o,j+1,-} \\ E_{e,j+1,-} \end{pmatrix} \tag{70}$$

Eq. (70) can then be substituted in:

$$\begin{pmatrix} E_{o,j,+} \\ E_{e,j,+} \\ E_{o,i,-} \\ E_{e,i,-} \end{pmatrix} = \overline{\overline{S_{ij}}} \begin{pmatrix} E_{o,i,+} \\ E_{e,i,+} \\ E_{o,j,-} \\ E_{e,j,-} \end{pmatrix} \tag{71}$$

After substitution, the components of $\overline{\overline{S_{ij+1}}}$ can be identified:

$$\overline{\overline{S_{ij+1,11}}} = \left(\overline{\overline{I_j}}^{-1}_{11} - \overline{\overline{S_{ij,12}}}\;\overline{\overline{I_j}}^{-1}_{21} \right)^{-1} \overline{\overline{S_{i,j,11}}} \tag{72}$$

$$\overline{\overline{S_{ij+1,12}}} = \left(\overline{\overline{I_j}}^{-1}{}_{11} - \overline{\overline{S_{ij,12}}}\,\overline{\overline{I_j}}^{-1}{}_{21}\right)^{-1}\left(\overline{\overline{S_{i,j,12}}}\,\overline{\overline{I_{j,22}}}^{-1} - \overline{\overline{I_j}}^{-1}{}_{12}\right) \tag{73}$$

$$\overline{\overline{S_{ij+1,21}}} = \overline{\overline{S_{ij,22}}}\,\overline{\overline{I_j}}^{-1}{}_{21}\,\overline{\overline{S_{ij+1,11}}} + \overline{\overline{S_{ij,21}}} \tag{74}$$

$$\overline{\overline{S_{ij+1,22}}} = \overline{\overline{S_{ij,22}}}\,\overline{\overline{I_j}}^{-1}{}_{21}\,\overline{\overline{S_{ij+1,12}}} + \overline{\overline{S_{ij,22}}}\,\overline{\overline{I_j}}^{-1}{}_{22} \tag{75}$$

We construct $\overline{\overline{I_j}}$ in the following way (a sketch is shown in Figure 2.8). First the input waves $\left[\mathrm{E}_{o,j,+}, \mathrm{E}_{e,j,+}, \mathrm{E}_{o,j,-}, \mathrm{E}_{e,j,-}\right]$ propagate from the (j-1)/j interface to the j/(j+1) interface, this causes a phase change proportional to the thickness of the layer d_j, expressed by the matrix $\overline{\overline{D_j}}$:

$$\overline{\overline{D_j}} = \exp(-jd_j\begin{bmatrix} k_{z,o,j,+} & 0 & 0 & 0 \\ 0 & k_{z,e,j,+} & 0 & 0 \\ 0 & 0 & k_{z,o,j,-} & 0 \\ 0 & 0 & 0 & k_{z,e,j,-} \end{bmatrix}) \tag{76}$$

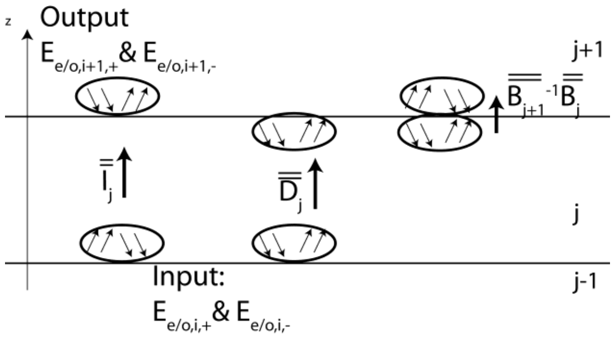

Figure 2.8 Sketch of the input and output waves of the matrix $\overline{\overline{I_j}}$. The phase propagation matrix $\overline{\overline{D_j}}$ and the matrices $\overline{\overline{B_j}}$ and $\overline{\overline{B_{j+1}}}$ relating the waves in medium j to the waves in medium (j+1).

At the interface j/(j+1) all transverse fields have to be constant, this is expressed by the following boundary conditions: $E_{x,j} = E_{x,j+1}$, $E_{y,j} = E_{y,j+1}$, $H_{x,j} = H_{x,j+1}$ and $H_{y,j} = H_{y,j+1}$. From the complex amplitudes of the four eigenmodes in medium (j+1) at the j/(j+1) interface and the unit fields of the four eigenmodes (given by Eq. (50) and (53)), the field components E_x, E_y, H_x and H_y at the j/(j+1) interface can be calculated. The matrix that links the amplitudes of the four eigenmodes in medium (j+1) with the four field components E_x, E_y, H_x and H_y at the j/(j+1) interface is written as $\overline{\overline{B_{j+1}}}$.

$$\begin{pmatrix} E_x \\ E_y \\ H_x \\ H_y \end{pmatrix} = \begin{bmatrix} 1_{o,+,j+1,x} & 1_{e,+,j+1,x} & 1_{o,-,j+1,x} & 1_{e,-,j+1,x} \\ 1_{o,+,j+1,y} & 1_{e,+,j+1,y} & 1_{o,-,j+1,y} & 1_{e,-,j+1,y} \\ Y_{o,+,j+1,x} & Y_{e,+,j+1,x} & Y_{o,-,j+1,x} & Y_{e,-,j+1,x} \\ Y_{o,+,j+1,y} & Y_{e,+,j+1,y} & Y_{o,-,j+1,y} & Y_{e,-,j+1,y} \end{bmatrix} \begin{pmatrix} E_{o,j+1,+} \\ E_{e,j+1,+} \\ E_{o,j+1,-} \\ E_{e,j+1,-} \end{pmatrix} = \overline{\overline{B_{j+1}}} \begin{pmatrix} E_{o,j+1,+} \\ E_{e,j+1,+} \\ E_{o,j+1,-} \\ E_{e,j+1,-} \end{pmatrix} \tag{77}$$

The matrix elements of the first two rows of $\overline{\overline{B_{j+1}}}$ are the x- and y components of Eq. (50) and (53). The corresponding magnetic field (per unit electric field) is found with $\mathbf{Y_{e/o}} = \mathbf{k} \times \mathbf{1_{e/o}} / (\omega\mu)$ (unit $1/\Omega$), the x- and y-component are the respective matrix elements of the third and fourth row.

In summary (see Figure 2.8), $\overline{\overline{D_j}}$ relates the amplitudes of the eigenmodes in medium j at the $(j-1)/j$ interface to the amplitude of the eigenmodes in medium j at the $(j+1)/j$ interface, $\overline{\overline{B_j}}$ (or $\overline{\overline{B_{j+1}}}$) relates the amplitudes of the four eigenmodes to the four transverse field components in medium j (or $j+1$) and $\overline{\overline{I_j}}$ relates the amplitudes of the eigenmodes at the $(j-1)/j$ interface in medium j to the amplitudes of the eigenmodes at the $(j+1)/j$ interface in medium $j+1$. The boundary condition at the $(j+1)/j$ interface can then be expressed as:

$$\overline{\overline{B_{j+1}}}\,\overline{\overline{I_j}} \begin{pmatrix} E_{o,j,+} \\ E_{e,j,+} \\ E_{o,j,-} \\ E_{e,j,-} \end{pmatrix} = \begin{pmatrix} E_{x,j+1} \\ E_{y,j+1} \\ H_{x,j+1} \\ H_{y,j+1} \end{pmatrix} = \begin{pmatrix} E_{x,j} \\ E_{y,j} \\ H_{x,j} \\ H_{y,j} \end{pmatrix} = \overline{\overline{B_j}}\,\overline{\overline{D_j}} \begin{pmatrix} E_{o,j,+} \\ E_{e,j,+} \\ E_{o,j,-} \\ E_{e,j,-} \end{pmatrix} \tag{78}$$

This equation has to hold for any input amplitudes $\left[\mathrm{E}_{o,j,+}, \mathrm{E}_{e,j,+}, \mathrm{E}_{o,j,-}, \mathrm{E}_{e,j,-}\right]$, so that:

$$\overline{\overline{I_j}} = \overline{\overline{B_{j+1}}}^{-1}\,\overline{\overline{B_j}}\,\overline{\overline{D_j}} \tag{79}$$

With $\overline{\overline{B_j}}$, $\overline{\overline{B_{j+1}}}$ and $\overline{\overline{D_j}}$ given by Eq. (77) and (76), this equation allows to calculate $\overline{\overline{I_j}}$ for every layer. $\overline{\overline{S_{iN}}}$ is found with Eq. (72)-(75) after successively adding all layers. $\overline{\overline{T^+}}$ and $\overline{\overline{A^+}}$ are identified with Eq. (67) and (68).

The matrix calculation presented in this section allows to determine the reflection matrices $\overline{\overline{A}}^{+/-}$ of a stack of anisotropic layers. Inserting the reflection matrix into (by eq. (62) and (63)) then yields the field emitted by a dipole inside the cavity.

2.5 Exciton decay rates

The power emitted by a dipole embedded in the microcavity depends on the design of the microcavity itself. From the viewpoint of decaying excitons, the change in power emitted means that the rate of exciton decay is altered. A single exciton will only emit a single photon, but more/less excitons will decay in a given time, so the power is accordingly increased/decreased. The power given by Fermi's golden rule (eq. (54)) can be factorized into the energy of a photon ($E_{photon} = \hbar\omega$) and the radiative decay rate Γ_r, which is the amount of excitons decaying per second (unit s^{-1}).

$$P = E_{photon}\Gamma_r = \hbar\omega\rho(k)\frac{2\pi}{c\hbar^2}\left| < f\,|\,\mathbf{p}\,|\,s > .\mathbf{E}(k)\right|^2 \tag{80}$$

The decay rate of excitons is not only a property of the emitting material itself but also of the optical environment of the material. If we call $\Gamma_{r,0}$ the intrinsic decay rate of an emitter in an infinite medium. The radiative decay rate Γ_r in a cavity is proportional to F the power radiated by the equivalent dipole in the cavity normalized by the power of the dipole in an infinite medium.

$$\Gamma_r = F\Gamma_{r,0} \tag{81}$$

For wavelength λ, F_λ is found by integrating the z-component S_z of the Poynting vector for all k_x and k_y and divided by $S_{z,0}$ for a dipole in an infinite medium.

$$F_\lambda = \int_{-\infty}^{+\infty}\int_{-\infty}^{+\infty}\frac{\mathbf{S}_{z,cav}}{\mathbf{S}_{z,0}}dxdy = \int_{-\infty}^{+\infty}\int_{-\infty}^{+\infty}\frac{Re\left[\mathbf{E}_{cav}(k_x,k_y)\times\mathbf{H}_{cav}(k_x,k_y)^*\right]_z}{Re\left[\mathbf{E}_0(k_x,k_y)\times\mathbf{H}_0(k_x,k_y)^*\right]_z}dk_xdk_y \tag{82}$$

The total generated power across all wavelengths is then found by integrating F_λ weighted with the intrinsic spectrum of the emitter.

$$F = \int d\lambda S_0(\lambda)F_\lambda(\lambda) \tag{83}$$

Apart from radiative decay there can also be non-radiative decay, with a decay rate Γ_{nr}. The total decay rate Γ_{tot} is the sum of both the radiative and non-radiative decay rates.

$$\Gamma_{tot} = F\Gamma_{r,0} + \Gamma_{nr} \tag{84}$$

The amount of excitons that decay per second is proportional to the amount of excitons N_{exc} present.

$$\frac{\partial N_{exc}}{\partial t} = -\Gamma_{tot} N_{exc} \tag{85}$$

When no additional excitons are generated N_{exc} will decrease exponentially.

$$N_{exc}(t) = N_{exc}(t=0)\exp\left(-\Gamma_{tot} t\right) \tag{86}$$

The amount of excitons decreases by a factor $1/e$ in the decay time $\tau = 1/\Gamma_{tot}$. The decay time of excitons can be observed by measuring the intensity after turning off the excitation source (either in electro- or photoluminescence). The intensity detected after removing the excitation source is proportional to $\partial N_{exc} / \partial t$ and also decays exponentially with time. Γ_{tot} can be extracted from the exponentially decreasing intensity over time.

Out of all excitons, only a part η_{rad} decays radiatively. η_{rad} is called the radiative efficiency of the emitter.

$$\eta_{rad} = \frac{F\Gamma_{r,0}}{F\Gamma_{r,0} + \Gamma_{nr}} \tag{87}$$

η_{rad} is not simply a property of the emitting system (guest/host material) but also of the optical environment, this is known as the Purcell effect (see section 2.3) [2-5].

2.6 Conclusion

In this chapter the radiation of dipole antennas in anisotropic one-dimensional layer stacks was calculated starting from Maxwell's equation. The field of a dipole is decomposed as a sum of plane waves. Using these formulas it is possible to study a whole range of devices where light is emitted via dipole transitions.

In planar microcavities the dipole field is significantly influenced by interference effects. Formulas were deduced to simulate the effect of uniaxial planar microcavities on the dipole field. The reflection and transmission of anisotropic layer stacks is calculated using the scattering matrix method. Finally the relation between dipole emitted power and exciton decay rate is explained.

The formulas in this chapter are generally applicable because the orientation of the dipole moment and the optical axes of the layers are not limited. In the next chapters these formulas will be used to study and design two different types of light emitting thin film devices: organic LEDs and liquid crystal lasers.

3. Organic Light Emitting Diodes

In chapter 2 the theory of the plane wave expansion method has been explained. In this chapter we will demonstrate the use of plane wave expansion to design the optical characteristics of OLEDs. First the basic properties of OLEDs are explained. Then we take a closer look at the problem of optical outcoupling. The aim is to improve outcoupling efficiency by tuning the interference in the cavity and/or by using oriented emitters with an appropriate radiation pattern.

3.1 Basic properties of OLEDs

3.1.1 Structure of an OLED

Conceptually an OLED operates in the same way as an inorganic LED (see Figure 3.1). When the potential difference over the electrodes is sufficiently high, electrons and holes are injected into the device by respectively the negative and the positive electrode.

Electrons and holes are then transported through the organic layers to the recombination zone. Organic materials with a high mobility for electrons/holes are respectively used to conduct the electrons and holes. These layers are respectively called electron transport layer (ETL) and hole transport layer (HTL), analogous to n and p-type semiconductor layers in an inorganic LED.

In the recombination zone electrons and holes form electron-hole pairs, also called excitons. Subsequently the electron-hole pairs recombine and the excess energy can be emitted as photons. The recombination zone is confined to the emissive layer (EML) by introducing hole and electron blocking layers (HBL/EBL) respectively between cathode/anode and the EML.

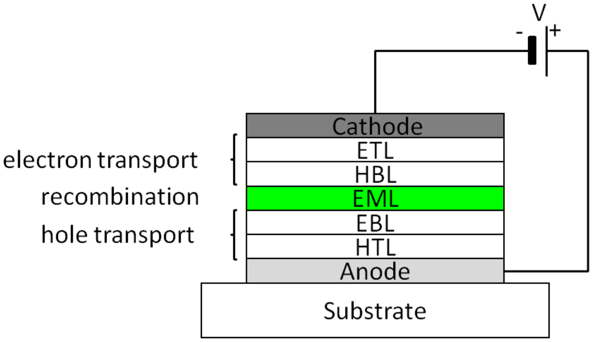

Figure 3.1 Typical layer structure of an OLED. The device consists of an anode/hole transport layer/electron blocking layer/emissive layer/hole blocking layer/electron transport layer/cathode evaporated on top of each other.

3.1.2 Electrical properties of OLEDS

The difference between an OLED and an inorganic LED is that in an OLED the charge transporting materials are organic layers with semiconductor-like properties rather than conventional semiconductors. In an organic semiconductor the electrons and holes do not occupy states in the conduction and valence bands that are defined by the crystal lattice. Instead the electrons and holes are confined to molecular orbitals, respectively the lowest unoccupied molecular orbital (LUMO) and the highest occupied molecular orbital (HOMO). In Figure 3.2 the HOMO and LUMO levels of the materials inside an OLED and the transport of holes and electrons is illustrated.

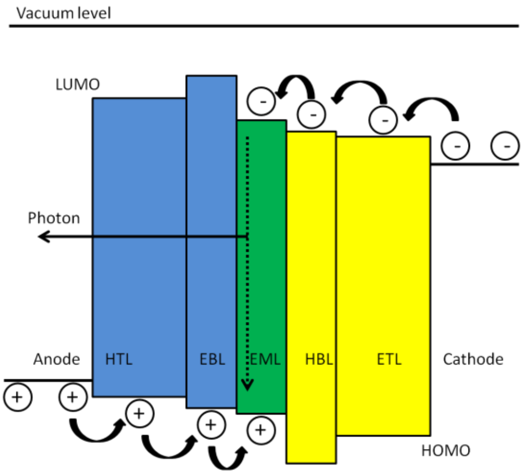

Figure 3.2 Diagram of the HOMO and LUMO levels of different materials in an OLED.

Different molecules are used to conduct electrons in the ETL or to conduct holes in the HTL. ETL materials have a high electron mobility but a low hole mobility, and vice versa for HTL materials[21, 22]. In the emitting layer (EML) electrons and holes can bind to each other and form excitons. Excitons are able to diffuse throughout the EML and eventually the electron and hole recombine releasing the excess energy. When the exciton recombines by a radiative process, a photon is emitted.

An important parameter for the efficiency of an OLED is the charge balance η_{cb}. If the holes are not effectively blocked, some of them can travel through the electron transport layer and reach the cathode. In this case fewer electrons will be injected than holes. In a typical OLED the hole mobility in the HTL is higher than the electron mobility in the ETL and as a consequence an excess of holes is injected. η_{cb} is defined as the number of electrons N_{e^-} injected at the cathode divided by the number of holes N_{h^+} injected at the anode (or vice versa if $N_{e^-} > N_{h^+}$). η_{cb} is a measure for the amount of excitons N_{exc} formed per injected charge. When $N_{e^-} = N_{h^+}$, equal amount of electrons and holes are injected and $\eta_{cb} = 1$.

$$\eta_{cb} = \min\left(\frac{N_{e^-}}{N_{h^+}}, \frac{N_{h^+}}{N_{e^-}}\right) \tag{88}$$

To prevent holes (and electrons) from traversing the device electron and hole blocking layers (EBL/HBL) are often deposited between the EML and the HTL/ETL respectively. Blocking layers improve η_{cb} and ensure that excitons are formed inside the EML.

The current voltage characteristic of an OLED is similar to that of a diode. An example is shown in Figure 3.3. When the voltage exceeds the "turn-on" voltage V_{on} the current density J increases exponentially. Below V_{on} a small leakage current is observed. The total power consumed (per m^2) by the OLED is given by:

$$P = VJ \tag{89}$$

Dopants can be introduced to decrease the resistivity of the ETL and HTL and thereby lower V_{on} and reduce ohmic losses [19, 20].

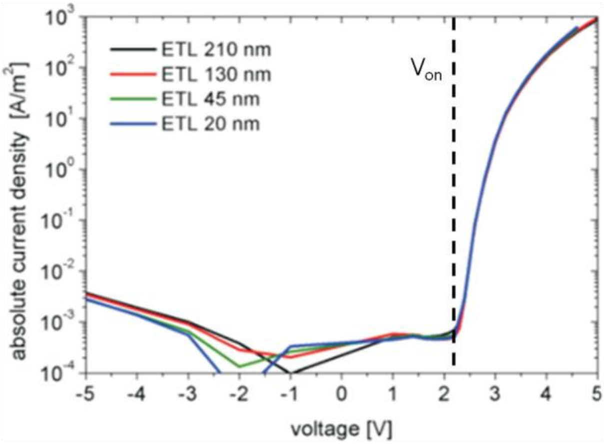

Figure 3.3 Current density vs. voltage in a number of OLEDs. The current density increases quickly once the voltage exceeds the "turn on" voltage [23].

3.1.3 Light Generation inside OLEDs

3.1.3.1 Fluorescent & phosphorescent emitters

Inside the EML the electrons and holes form excitons. These excitons can then decay back to the ground state and emit the excess energy as a photon. The EML often consists of an organic semiconductor "host" material and a percentage of "guest" emitting dye material. In a guest/host system excitons recombine when they are localized on an emitting guest molecule. The excitons on a host site diffuse through the EML until they recombine on a guest site. Two types of emitters are distinguished: fluorescent and phosphorescent emitters.

The difference between fluorescent and phosphorescent emitters originates from the type of excited state that can decay radiatively. In Figure 3.4 the energy levels and allowed transitions in a fluorescent and phosphorescent emitter are schematically represented. In a fluorescent emitter photons are emitted by excitons that decay from the singlet state (25% of all excitons) to the ground state, while the excitons in the triplet state (75% of all exitons) decay non-radiatively. The fraction of excitons that is in the singlet state is one quarter and therefore the singlet/triplet efficiency is $\eta_{st} = 0.25$ for fluorescent emitters.

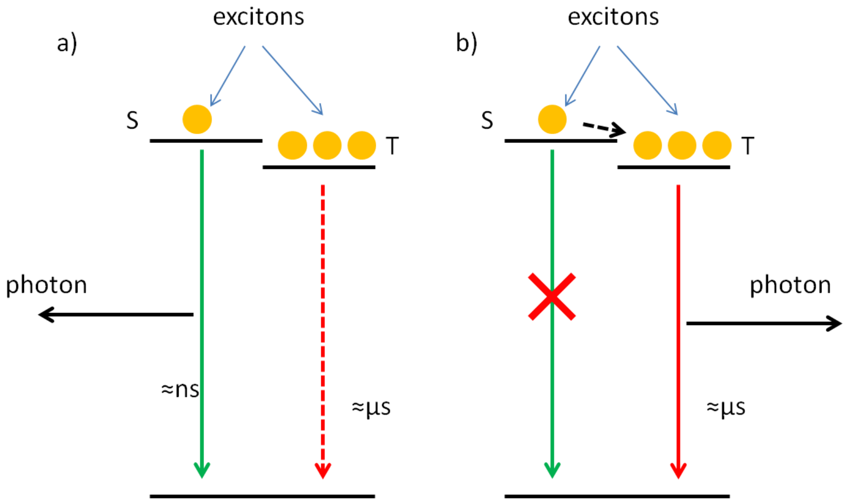

Figure 3.4 Exciton decay mechanisms: a) Fluorescent emitter: only singlet excitons can generate a photon. b) Phosphorescent emitter: triplet excitons decay with light emission. Singlet excitons decay indirectly via the triplet state. Nearly all excitons can generate a photon.

In a phosphorescent emitter the transition from the singlet state to the ground state does not occur but the triplet excitons decay radiatively. The excitons in the singlet state first transfer into a triplet state in a process known as intersystem crossing and then decay to the ground state. In this way both singlet and triplet excitons can decay radiatively and nearly all excitons decay radiatively [24]. For a phosphorescent emitter $\eta_{st} = 1$.

Fluorescent decay processes are much faster than phosphorescent processes. Fluorescent decay times are of the order of ns. The timescale for phosphorescent decay is in the μs-range.

3.1.3.2 Radiative and non-radiative decay

Even if an exciton is in a state (singlet or triplet) where it can emit a photon (radiative decay), recombination through other (non-radiative) processes is still possible. Furthermore the radiative decay rate is influenced by the optical environment (see section 2.5). Non-radiative decay is an additional loss mechanism inside organic LEDs.

Out of all excitons, only a fraction η_{rad} decays radiatively. η_{rad} is called the radiative efficiency of the emitter.

$$\eta_{rad} = \frac{F\Gamma_{r,0}}{F\Gamma_{r,0} + \Gamma_{nr}} \tag{90}$$

The effect of the optical environment on the exciton decay time and the OLED efficiency is discussed in more detail in section 3.3.

3.1.4 Outcoupling

3.1.4.1 Light trapping inside OLEDs

Another important factor in the efficiency of an OLED is the optical outcoupling. Effective outcoupling ensures that the generated light reaches the outside world and is not re-absorbed somewhere in the device. The optical outcoupling efficiency η_{out} is defined as optical power which escapes into air I_{air} (normalized with the power emitted in an infinite medium) or into the substrate I_{sub} divided by the total generated power F. In a conventional OLED without outcoupling structures $\eta_{out} \approx 20\%$.

$$\eta_{out,sub/air} = \frac{I_{sub/air}}{F} \tag{91}$$

The reason for the low outcoupling is that the light is generated inside organic layers which have a high refractive index of around 1.8. The emitted light can be viewed as a series of plane and evanescent waves emitted in all directions inside the organic layers. When a plane wave enters a medium with a lower refractive index (for example from glass $n_{glass} = 1.5$ to air $n_{air} = 1$) it is refracted according to Snell's law Eq. (11) (see Figure 3.5).

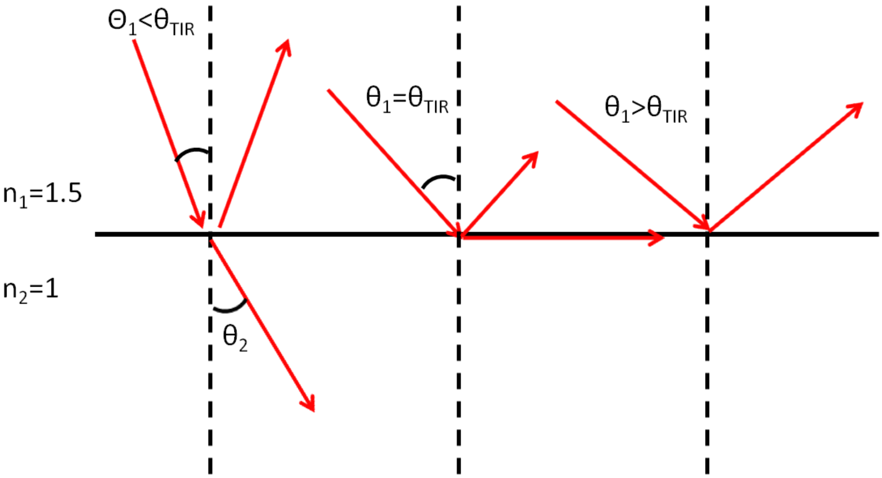

Figure 3.5 Refraction and total internal refraction of light when a beam passes from a high index to a low index medium.

When the angle of incidence is above the total internal reflection angle θ_{TIR} the plane wave is 100% reflected and cannot propagate in the low index medium. Plane waves with an incident angle below θ_{TIR} are transmitted with partial reflection. θ_{TIR} defines an escape cone. Only rays inside the escape cone can escape the higher index medium.

$$\theta_{TIR} = \mathrm{Arcsin}\left(\frac{n_2}{n_1}\right) \tag{92}$$

Inside an OLED light is generated inside the organic layers with refractive index 1.8. The rays should then escape to the substrate, which is usually glass or plastic ($n_{sub} = 1.5$). Finally the light needs to reach air ($n_{air} = 1$). Inside the organic layers light is emitted in every direction (for the moment we assume that equal power is emitted in every direction) but only rays inside the escape cone are able to enter the substrate. In Figure 3.6 a schematic of the escape cones is drawn, for the escape from organics to substrate and from substrate to air. Typical values for the power trapped in the OLED layers, the substrate and escaping to air are given.

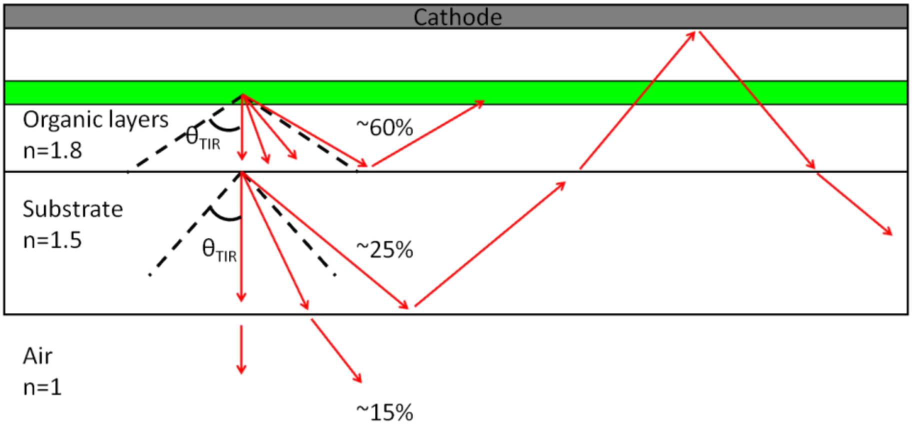

Figure 3.6 Light outcoupling is limited by total internal reflection at the organic/substrate and substrate/air interface. Only light inside the escape cone reaches the outside of the device.

In an OLED rays should escape from $n = 1.8$ to $n = 1$ and the escape cone is at an angle $\theta_{TIR} = 33.7°$. The maximum outcoupling efficiency can also be estimated based on the principle of étendue. The conservation of étendue is a fundamental concept in optics, see e.g. chapter 1 in [25] and [26]. As light passes through an optical system the étendue remains constant (it may also increase).

The étendue of a distribution of plane waves $P(\theta)$ is given by formula (93) where A is the area where the light passes through and n is the refractive index of the medium.

$$G = n^2 A \int_0^{2\pi} \int_0^{\pi/2} \cos\theta \sin\theta d\theta d\varphi \tag{93}$$

The maximum étendue in air is thus $A\pi$. Whereas the maximum étendue in the organic layers is $n_{org}^2 A\pi$. Since the étendue does not decrease as light passes through the outcoupling system, at most an étendue of $A\pi$ can be transmitted from the organics to air in a single pass. If we assume the emission pattern is Lambertian($P(\theta) = \cos(\theta)$) in the organic layers, the highest fraction of light that can be transmitted in a single pass is given by:

$$\frac{n_{air}^2 A \int_0^{2\pi} \int_0^{\pi/2} \cos\theta \sin\theta d\theta d\varphi}{n_{org}^2 A \int_0^{2\pi} \int_0^{\pi/2} \cos\theta \sin\theta d\theta d\varphi} = \frac{n_{air}^2}{n_{org}^2} \approx 30\% \tag{94}$$

Eq. (94) expresses the maximum outcoupling of a Lambertian emitter in a single pass by any optical system. Note that this restriction applies not only to planar layers but is valid for any outcoupling design (e.g. microlenses, scattering foils, ...).The outcoupling efficiency can be increased by multiple passes through the system (via reflection on the organic stack) or using a non-Lambertian emission. Eq. (94) demonstrates the importance of multiple reflections for obtaining high outcoupling.

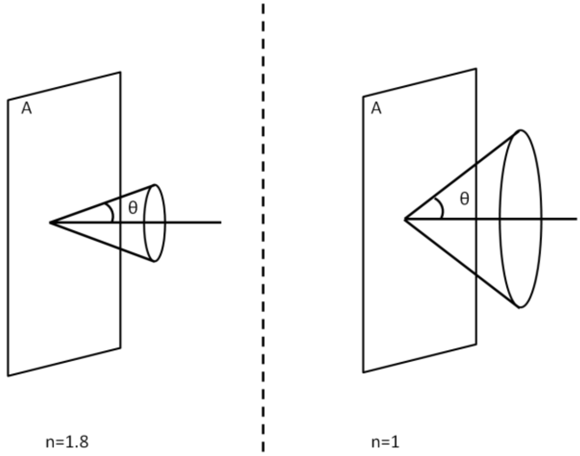

Figure 3.7 Radiation patterns of equal étendue in a medium with index 1.8 and 1. Etendue is conserved when light passes through an optical system.

3.1.4.2 Outcoupling solutions

The efficiency of OLEDs can be significantly increased by improving the light outcoupling. Several types of outcoupling enhancing mechanisms such as microcavity/interference effects [27], microlenses [28], scattering particles [29] or periodic gratings [30] have been demonstrated in literature. Here we will give a brief overview of the most common methods.

The approaches to improving outcoupling can be divided into two types. The first is to modify the angular emission pattern so that more light is emitted inside the escape cone. A second way to improve outcoupling is to use non-planar structures (microlenses, gratings, microparticles) which change the direction of light by scattering or refracting light into the escape cone. It is important to note that both approaches should be used simultaneously to obtain a high η_{out}.

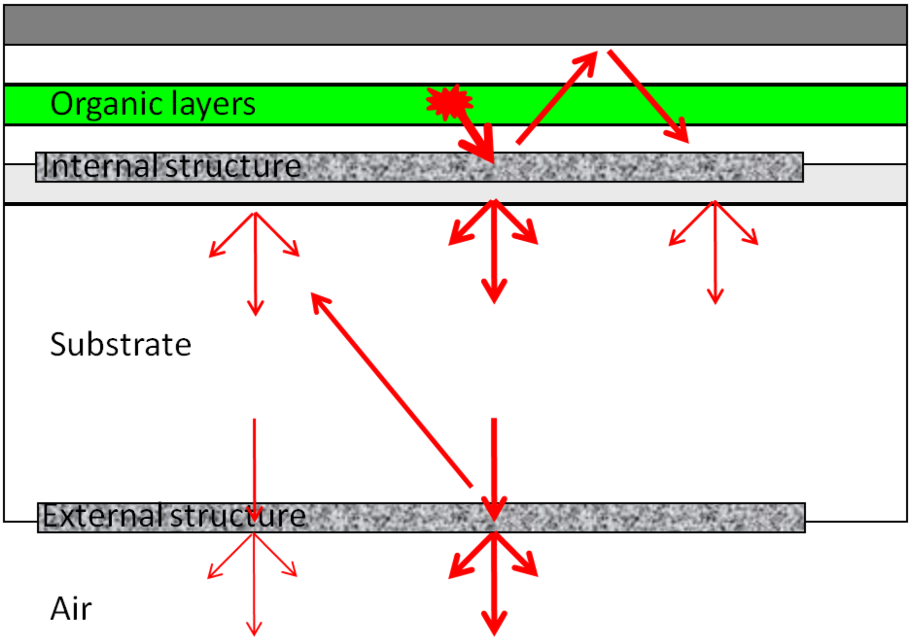

Figure 3.8 External structures increase substrate to air outcoupling. Internal structures extract light from the organic layers to the substrate and also influence extraction from the substrate to air.

A distinction between different structures is whether they improve outcoupling from the organic layers to the substrate (internal structure) or from the substrate to air (external structure). A sketch of the interaction between internal and external structures is shown in Figure 3.8.

Light generated inside the organic layers is partly extracted by the internal structures, another part is reflected back and forth in the organic layers where it can get a second chance of being extracted by the internal structure. The light in the substrate is partly extracted by the external structure and partly reflected back to the organic layers. The part that is reflected back to the cathode is scattered by the internal structure and again reflected into the substrate, where it gets a new chance to be extracted.

These multiple reflections between the substrate/air interface and the cathode are important for outcoupling improvement. When the direction of the ray is changed by the outcoupling structure (either internal or external), the light gets a second chance of being extracted. In this way an internal structure can also improve the outcoupling from substrate to air.

A final comment should be made about the absorption losses in the cathode and the organic layers. Every time the light is reflected back and forth between the substrate and the OLED a fraction of the light (around 20% for an Al cathode) will be absorbed. Since the substrate is optically thick (much thicker than the coherence length of the emitted light) we can treat these reflections incoherently. If 20% of the light is absorbed every time the light travels back and forth from the OLED layers to the substrate/air interface, the intensity will drop below 20% of its initial value after 8 passes. If the absorption is reduced to 10%, 16 passes occur before the intensity drops to 20%.

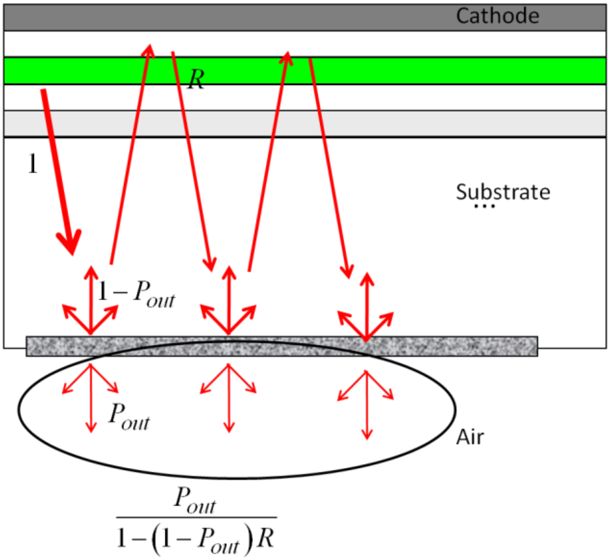

Figure 3.9 Outcoupling structures rely on multiple reflections between substrate and organic layers. Optimal outcoupling requires scattering and high reflectivity.

The lower the absorption, the more chances there are for extraction. This can be seen from a simplified model [31], sketched in Figure 3.9. Assume that every time the light reaches the glass/air interface a fraction P_{out} escapes the device by scattering or some other outcoupling structure. The remaining $1-P_{out}$ is reflected back to the cathode, where a part R is reflected (and $1-R$ is absorbed). The light reaches the glass/air interface a second time and again $(1-P_{out})RP_{out}$ is extracted. After infinite reflections we find:

$$\eta_{out} = \frac{P_{out}}{1-(1-P_{out})R} \tag{95}$$

If $R = 100\%$ (0% absorption), we find $\eta_{out} = 100\%$ even when P_{out} is small (a small scattering probability is sufficient to avoid trapping of the light). The outcoupling process is a competition between absorption and scattering. For optimal outcoupling light has to be scattered efficiently and absorption should be avoided.

3.1.5 Overall efficiency

A useful figure of merit for the overall performance of OLEDs is the external quantum efficiency (EQE). EQE is defined as the amount of photons $N_{ph,out}$ that is extracted per injected charge N_{h^+} (or N_{e^-}) injected. The EQE can be separated in four different factors[19, 26].

$$EQE = \frac{N_{ph,out}}{N_{h^+}} = \eta_{cb}\eta_{st}\eta_{rad}\eta_{out} \tag{96}$$

The four factors in formula (96) can each be linked to a different step of the light generation process, this is represented in Figure 3.10. The charge balance η_{cb} is determined by the electrical properties of the OLED (section 3.1.2). The singlet-triplet ratio η_{st} determines how many excitons are in a state that can decay radiatively . This is a material parameter of the dye dopant. It is either 0.25 or 1, respectively for fluorescent and phosphorescent emitter molecules (section 3.1.3.1). The radiative efficiency η_{rad} is the percentage of the excitons that actually emit a photon (section 3.1.3.2). η_{rad} depends on the material properties of the dye-host materials and on the organic layer stack. The amount of light that can escape from the device is given by η_{out} (section 3.1.4) and depends on the optical design of the OLED. In a state-of-the-art phosphorescent OLED without additional outcoupling mechanisms, the EQE is around 20% [24, 32].

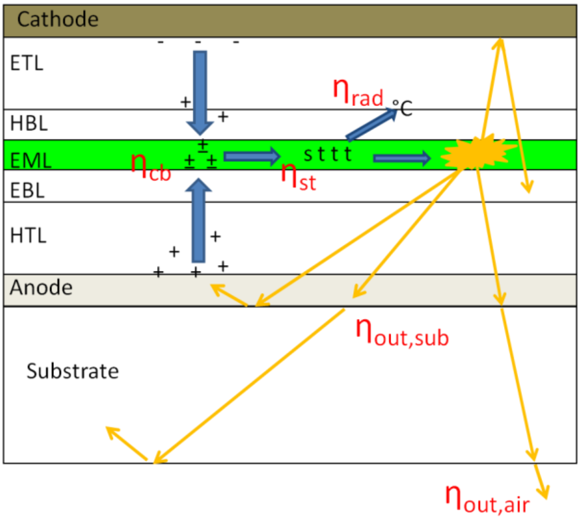

Figure 3.10 Schematic of the different contributions to the EQE: charge-balance, singlet-triplet ratio, radiative efficiency and outcoupling efficiency.

The EQE gives the percentage of injected charges which lead to a photon emitted from the device. However the human eye is not equally sensitive to photons of every wavelength. Green light appears much brighter than red light of equal power and IR and UV light are not visible at all. The relation between the power (in Watt) and the luminous flux LF (measured in lumen) for different wavelengths is given by the eye sensitivity curve $V_0(\lambda)$ (unit lm/W). For a broad spectrum light source the luminous flux LF (unit lm) can be found by the integrating the radiant flux $RF(\lambda)$ (unit W/m) with $V_0(\lambda)$.

$$LF = \int_0^\infty V_0(\lambda) RF(\lambda) d\lambda \tag{97}$$

Where $RF(\lambda)$ (unit W/m) is:

$$RF(\lambda) = \frac{J}{e^-} \eta_{cb} \eta_{st} \iint_{2\pi} S_0(\lambda) \frac{hc}{\lambda} \frac{\Gamma_{r,0}}{F\Gamma_{r,0} + \Gamma_{nr}} P_\lambda(\theta, \lambda) d\Omega \tag{98}$$

The luminous current efficacy LCE (unit lm/A) and luminous efficacy LE (lm/W) take into account the eye sensitivity and are a more complete measure for the efficiency of OLEDs. The LCE of an OLED can be calculated when the normalized intrinsic spectrum $S_0(\lambda)$ $(\int_0^\infty S_0(\lambda)d\lambda = 1)$ and the decay rates of the EML are known [23]:

$$LCE = \eta_{cb}\eta_{st}\int_0^\infty V_0(\lambda)S_0(\lambda)\iint_{2\pi}\frac{hc}{\lambda e^-}\frac{\Gamma_{r,0}}{F\Gamma_{r,0}+\Gamma_{nr}}P_\lambda(\theta,\lambda)d\Omega d\lambda \quad (99)$$

The LE can be found by dividing the LCE by the corresponding voltage.

3.2 Outcoupling in planar OLEDs

In this section we will take a closer look at the outcoupling and its limitations in planar OLEDs. In a planar OLED light is emitted in four different channels: evanescent waves, waves trapped in the organic layers, waves in the substrate and waves in air. Ultimately only the waves which escape to air are useful. The other three are eventually absorbed and should be seen as a loss mechanism in a planar OLED. However they may be outcoupled in non-planar OLEDs (see section 3.1.4.2).

Light emission inside the OLED is modelled as the emission of a dipole antenna. In the next paragraph the global radiation pattern inside an OLED is examined. The organic layer structure can be optimized to increase outcoupling. Finally we analyze the absorption of evanescent waves in more detail.

3.2.1 Dipole radiation in a planar OLED

The excitons inside an OLED can decay to the ground state via an electric dipole transition. The exciton decay is a quantum-mechanical process but the emission of photons from an ensemble of excitons is equivalent to the classical case of an ensemble of radiating dipole antennas [11, 12].

Inside an OLED the radiation pattern of a dipole is altered from that of a dipole in an infinite medium by interference effects from reflections on each of the layer interfaces in the OLED stack (see section 2.3). From the plane wave expansion (Eq. (58)-(61)) the normalized flux K (unit m^2) per κ^2 is known. Since $\kappa = k_o n_i \sin(\theta_i)$ the flux per space-angle $P_i(\theta_i)$ (unit sr^{-1}) in medium i can be related to $K_i(\kappa)$:

$$P_i(\theta_i,\lambda) = \frac{k_i^2\cos(\theta_i)}{\pi}K_{i,\lambda}(\kappa,\lambda) \quad (100)$$

The normalized total flux $I_i(\lambda)$ is then found by integrating over θ_i and φ (factor 2π).

$$I_{i,\lambda}(\lambda) = 2\pi \int_0^{\pi/2} P_{i,\lambda}(\theta_i, \lambda)\sin(\theta_i) d\theta_i \tag{101}$$

The total generated power F is the integral over all plane waves (propagating and evanescent):

$$F_\lambda(\lambda) = \int_0^\infty K_\lambda(\kappa, \lambda)\mathrm{d}\kappa^2 \tag{102}$$

The outcoupling efficiency is defined as the power that escapes to air (or the substrate) divided by the total generated power:

$$\eta_{out,sub/air} = \frac{I_{sub/air}}{F} \tag{103}$$

We can make a distinction between light coupled to air $\eta_{out,air}$ or to the substrate $\eta_{out,sub}$. The substrate light is not completely extracted in a planar OLED but this light is available for outcoupling by structures at the substrate/air interface. Light in the organic layers and evanescent waves can only be extracted by internal structures.

In Eq. (100)-(102) $P_i(\theta_i)$ $K_i(\kappa)$, I_i and F depend on the wavelength. The corresponding quantities for a broad spectrum can be found by taking the integral over λ weighted by the emitter intrinsic spectrum $S_0(\lambda)$ (unit m^{-1}).

$$P_i(\theta_i) = \int S_0(\lambda)\, P_{i,\lambda}(\theta_i, \lambda)(\lambda) d\lambda \tag{104}$$

$$K_i(\kappa) = \int S_0(\lambda)\, K_{i,\lambda}(\kappa, \lambda) d\lambda \tag{105}$$

$$I_i = \int S_0(\lambda)\, I_{i,\lambda}(\lambda) d\lambda \tag{106}$$

$$F = \int S_0(\lambda)\, F_\lambda(\lambda) d\lambda \tag{107}$$

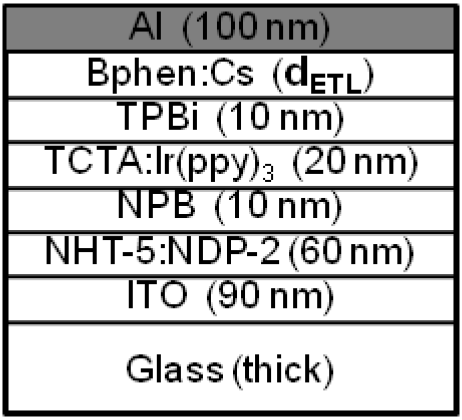

Figure 3.11 Layer structure of green OLED used for simulation.

As an example we calculate the radiation (integrated over all wavelengths) in the OLED depicted in Figure 3.11. The angular distribution in the EML layer is displayed in Figure 3.12 for ETL thicknesses of 50, 130 and 210nm (a, b and c). For 50nm the radiation is mostly directed into the escape cone for air and a smaller fraction remains trapped in the substrate. The side lobes at angles above $\theta_{substrate}$ are waveguided inside the organic layers. Since most of the radiation is inside the escape cone, this OLED will show good outcoupling. For an ETL thickness of 130nm (Figure 3.12b) most light is either trapped in the organics or the substrate. This OLED will be inefficient because of poor outcoupling. In Figure 3.12c (210nm ETL) again most light is directed into the escape cone, hence η_{out} will be high.

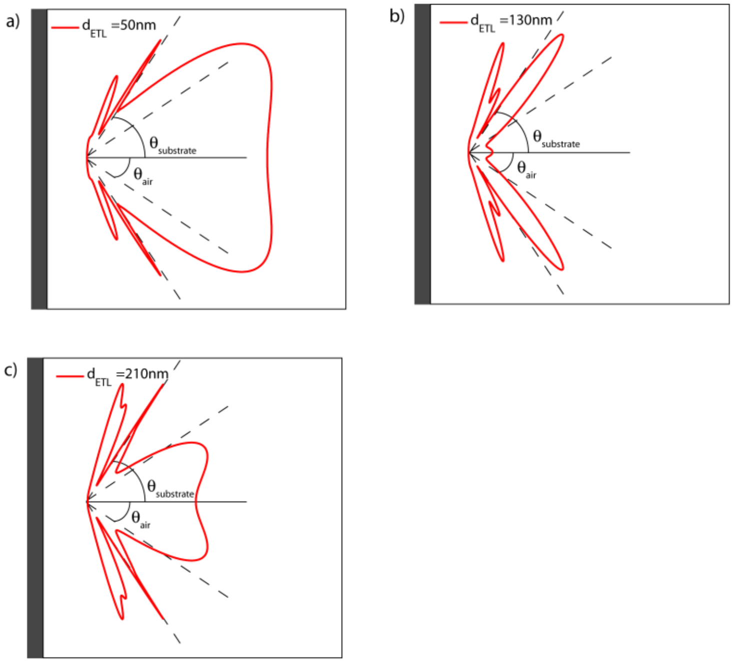

Figure 3.12 Angular distribution $P(\theta)$ of dipole radiation in OLEDs with various ETL thicknesses. Respectively 50nm, 130 and 210nm ETL (a, b and c)

The dipoles in the OLED do not only excite plane waves (which are portrayed in Figure 3.12) but also evanescent waves. In a loss free medium (no absorption) evanescent waves do not carry any power, in reality the OLED contains absorbing materials, most importantly the metal cathode (and some absorption in the organic layers and ITO anode).

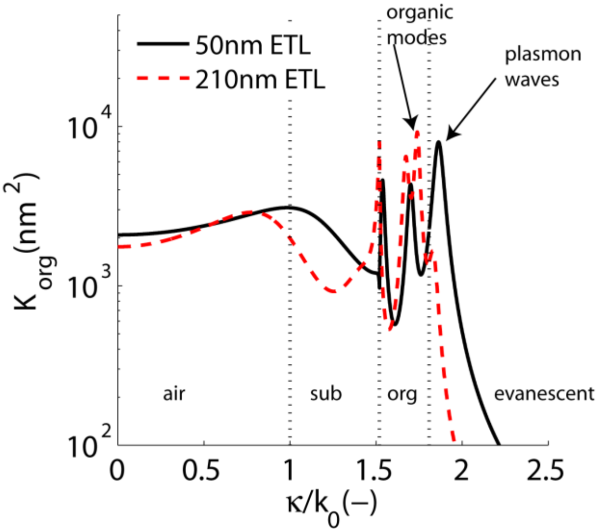

Figure 3.13 Distribution of plane waves vs. in-plane wave vector for OLEDs with ETL 50 and 210 nm. Light can be radiated in 4 channels: to air, to the substrate, to the organics, and as evanescent waves.

The distribution over plane and evanescent waves is displayed in Figure 3.13 for two ETL thicknesses. In the evanescent region a peak is seen in the emission. This is due to the excitation of surface plasmons (see section 3.2.3). It can be seen that the OLED with thin ETL radiates more power into evanescent waves. These near-field interactions between the dipole and the absorbing metal grow stronger as the dipole gets closer to the metal. Since all evanescent waves are eventually absorbed, they should be counted as a loss mechanism in OLEDs. In principle plasmon waves can also be extracted by scattering near the metal [33].

3.2.2 Outcoupling efficiency vs. ETL thickness

In the previous section the different radiation channels in an OLED were discussed. Depending on the ETL thickness the dipole radiation can be mainly inside or outside the escape cone.

Figure 3.14a shows the power emitted in air, substrate, organics as well the total emitted power as a function of the ETL thickness. We see a wavy pattern in the power vs. ETL thickness curve with maxima around 50 and 210nm (these are known as the first and second maximum for emission). A minimum is seen around d_{ETL} 130nm. This behaviour is in accordance with the angular distribution from Figure 3.12. For the two maxima the radiation is directed in the escape cone and $I_{air/sub}$ is high. For the minimum most radiation is directed to the trapped angles and $I_{air/sub}$ is low. The total emitted power F (solid curve) shows a similar oscillating behaviour but as d_{ETL} becomes small, F increases even though the power in the organics, substrate and air decrease. The rise in F is caused by increased coupling to evanescent waves as the dipole approaches the cathode. Note that the $I_{org} > I_{sub} > I_{air}$ since all light that enters air also enters the substrate/organic layers and all light that enters air also enters the organic layers.

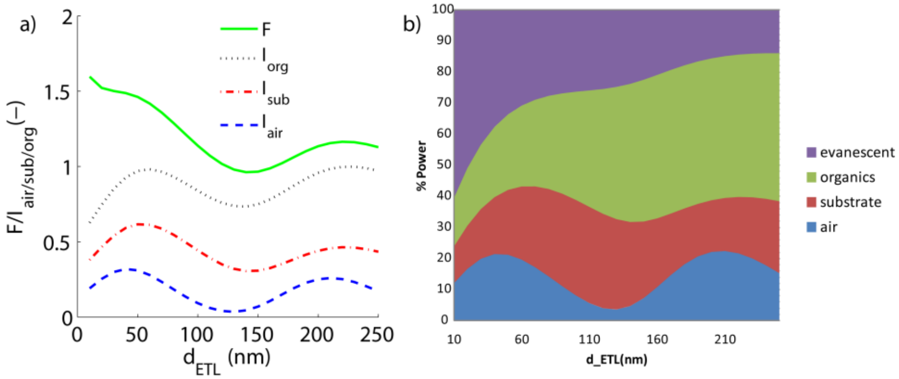

Figure 3.14 a) Power emitted into air, substrate and organic layers and total emitted power vs. ETL thickness. b) Distribution of emitted power in percentage vs. thickness.

Figure 3.14b shows the distribution in percentages of the normalized power into the four different channels. The four channels are shown in a cumulative way, the sum amounts to 100%. For very thin ETL layers most power is lost to evanescent waves. Two maxima are found for emission to air and the substrate.

3.2.3 Absorption of evanescent waves

In this section we take a closer look at the absorption of evanescent waves. The evanescent losses are caused by two processes: the excitation of surface plasmon waves and the absorption of the near-field of the dipole antenna [12]. Both the plasmon waves and the absorption of the near field are an interaction between the metal cathode and the evanescent waves emitted by the dipole. In Figure 3.15 the radiation pattern (as a function of κ) is shown for a vertical dipole near a glass/metal interface. The refractive index of the metal in this example is $n_m = -0.1 + 4j$[1]. For $\kappa > k_0 n_a$ the emission into evanescent waves can be seen.

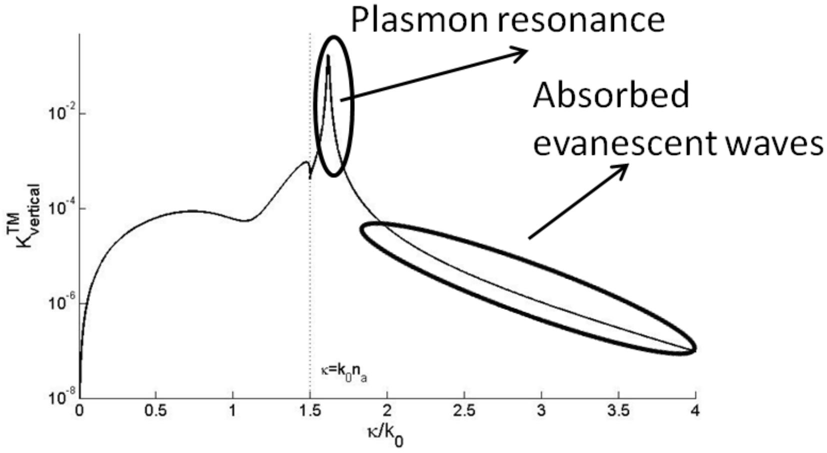

Figure 3.15 : Radiation pattern of a vertical dipole near a glass/metal interface. The near-field of the dipole (evanescent waves) excites a surface plasmon and is absorbed by the metal.

The plasmon resonance is seen as a narrow peak in the emission distribution for evanescent waves with a κ just above the transition ($\kappa = k_0 n$) from propagating to evanescent waves. Near-field absorption occurs for an extended region of quickly decaying evanescent waves (large κ). The power dissipated into the surface plasmon resonance or near-field absorption is dependent on the distance between the dipole and the metal. The peak of the plasmon resonance is several orders of magnitude higher than the near-field absorption, but near-field absorption extends over a wide κ-range. Both coupling to the plasmon resonance and near-field absorption can become dominant depending on the distance between the dipole and the metal.

---

[1] In section 3.2.3 the sign convention $\exp(+j\omega t - j\mathbf{k}.\mathbf{r})$ is assumed instead of $\exp(-j\omega t + j\mathbf{k}.\mathbf{r})$ in [12]. This different convention has no influence on the results obtained.

3.2.3.1 Plasmon waves

A surface plasmon is a guided electromagnetic wave which travels without changing its shape along the surface of a (non-absorbing) metal/dielectric interface. The electric field profile of the plasmon mode is evanescent in both the dielectric and the metal and is TM polarized [34]. The origin of the surface plasmon mode lies in resonances of the free electrons at the metal interface[35]. Mathematically this is expressed in the factor $1+A_{TM}$ in the numerator of eq. (58). The reflection coefficient A_{TM} contains the Fresnel reflection coefficient for TM polarization: $r_{a,m}^{TM}=(n_m^2 k_{z,a}-n_a^2 k_{z,m})/(n_m^2 k_{z,a}+n_a^2 k_{z,m})$.

If the metal is non-absorbing, $n_m^2 k_{z,a}+n_a^2 k_{z,m}$ can become zero for a particular value of $\kappa=\kappa'$ and $r_{a,m}^{TM}\rightarrow\infty$. Around this discrete plasmon resonance, K^{TM} behaves like a delta function. A finite power is radiated into the surface plasmon mode.

If the metal is absorbing, the absolute value of the denominator can become small (but not zero) and K^{TM} can reach a high value. In this case there is a range of values κ for which the radiation is ‘plasmon-like’. If the absorption of the metal increases or the dipole is located closer to the metal interface, the width of the plasmon peak increases and the identification as a resonant mode loses its meaning.

Because $k_{z,a}$ and $k_{z,m}$ are mainly imaginary for evanescent waves ($k_{z,m}$ has a small real part if the metal is absorbing) and n_a^2 and n_m^2 are mainly real (n_m^2 has a small imaginary part if the metal is absorbing), the denominator of $r_{a,m}^{TM}$ will reach a minimum near the κ where the imaginary part vanishes. The condition for κ' , the transverse part of the wavevector of the plasmon resonance, is defined as:

$$\mathrm{Im}(n_m^2 k_{z,a}+n_a^2 k_{z,m})=0 \tag{108}$$

which (after eliminating the k_z values using eq. (10)) leads to:

$$\kappa'^2=k_0^2\,\frac{n_a^2\,\mathrm{Re}(-n_m^2)}{\mathrm{Re}(-n_m^2)-n_a^2} \tag{109}$$

In the case of a non-absorbing metal, the refractive index is purely imaginary $n_m = -j\sigma$. The plasmon resonance yields a discrete, infinite peak at:

$$\kappa'^2 = k_0^2 \frac{n_a^2 \sigma^2}{\sigma^2 - n_a^2} \tag{110}$$

$$k'_{z,a} = j \frac{k_0 n_a^2}{\sqrt{\sigma^2 - n_a^2}} \tag{111}$$

When the metal is absorbing $n_m = -\varepsilon + j\sigma$. If $\varepsilon << \sigma$, eq. (58) and (60) can be approximated by a Lorentzian peak around κ' with $\kappa = \kappa' + \Delta\kappa$ and $\Delta\kappa << \sigma$. By using a linear approximation of $k_{z,a}$ and $k_{z,m}$ we find:

$$K^{TM}_{vertical,\lambda}(\kappa) \approx \frac{3\sigma^5 n_a \left|k'_{z,a}\right|}{2(\sigma^2 + n_a^2)k_0} \cdot \frac{\varepsilon \exp\left(-2\left|k'_{z,a}\right| d\right)}{\varepsilon^2 n_a^6 k_0^2 + \Delta\kappa^2 (\sigma^2 - n_a^2)^3} \tag{112}$$

$$K^{TM}_{horizontal,\lambda}(\kappa) \approx \frac{3\sigma^3 n_a^3 \left|k'_{z,a}\right|}{4(\sigma^2 + n_a^2)k_0} \cdot \frac{\varepsilon \exp\left(-2\left|k'_{z,a}\right| d\right)}{\varepsilon^2 n_a^6 k_0^2 + \Delta\kappa^2 (\sigma^2 - n_a^2)^3} \tag{113}$$

The power radiated by a dipole into the plasmon resonance can be found by evaluating the integral of Eq. (102) with K^{TM}_{λ} given by Eq. (112) . We can expand the integration area to ±∞, since only the region around the Lorentzian peak contributes to the value of the integral. For the power coupled to the plasmon resonance we find [12]:

$$P^{plasmon}_{vertical,\lambda} = \frac{3\pi\sigma^6 n_a \exp\left(-2\left|k'_{z,a}\right| d\right)}{(\sigma^4 - n_a^4)(\sigma^2 - n_a^2)^{3/2}} \tag{114}$$

$$P^{plasmon}_{horizontal,\lambda} = \frac{3\pi\sigma^4 n_a^3 \exp\left(-2\left|k'_{z,a}\right| d\right)}{2(\sigma^4 - n_a^4)(\sigma^2 - n_a^2)^{3/2}} \tag{115}$$

These equations do not depend on ε. It can be verified that the equations hold for a non-absorbing metal, $\varepsilon = 0$. The exponential dependency on the distance d of the power coupled to the plasmon mode has been pointed out in [36]. The above analytical formula provides in addition the dependency on the parameters σ and n_a.

Eq.(114) gives an analytical formula for the power coupled to the plasmon, which decreases exponentially with the distance d. This means a dipole should be within a few wavelengths of the metal in order to couple to the plasmon. A vertical dipole radiates $2\sigma^2 / n_a^2$ times more power to the plasmon than a horizontal dipole. This is because the plasmon electric field is mainly oriented along the z-axis.

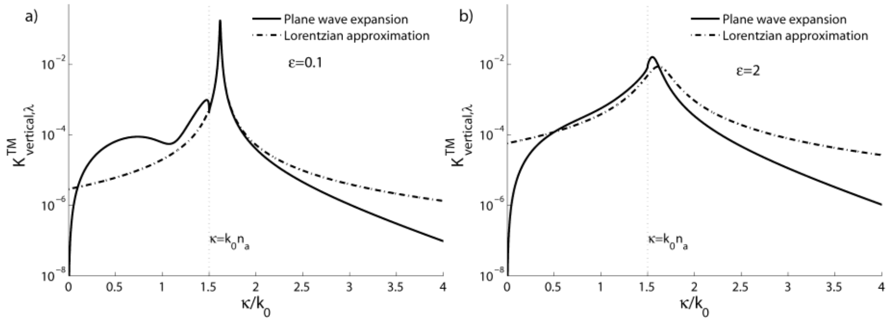

Figure 3.16 : Comparison of the Lorentzian approximation (Eq.(112)) of the plasmon resonance to the original plane wave expansion formula (Eq.(58)) for $\varepsilon = 0.1$ (left) and $\varepsilon = 2$ (right).

Figure 3.16 plots the power distribution as a function of κ in the Lorentzian approximation (dashed curve Eq.(112)) and for the exact expression (solid curve) in eq. (58). For ε=0.1 (Figure 3.16a) the Lorentzian peak matches the original formula around the plasmon resonance very well. For ε=2 (Figure 3.16b) the Lorentzian model deviates from the original formula, and there is no longer a well defined peak. This illustrates that a description with a single resonant mode is no longer appropriate when the absorption of the metal is significant.

3.2.3.2 Near-field absorption

Another effect occurs when a dipole antenna is within a few tens of nm of an absorbing metal: absorption of the near-field of the dipole. The near-field corresponds to the evanescent waves in the wave decomposition of the electric field (see Figure 3.15) . The closer the metal, the more interaction there will be between the fast decaying evanescent waves (with large κ) and the absorbing metal. The power coupled to the metal in this way can be calculated by evaluating the integral in eq. (102) for large values of κ . If κ is large, the integrand can be simplified by using the following approximations:

$$\begin{aligned} &\kappa >> k_0 n_a; \quad \kappa >> k_0 \left| n_m \right| \\ &k_{z,i} \approx j\kappa (1 - \frac{k_0^2 n_i^2}{2\kappa^2}) \\ &r_{a,m}^{TM} \approx \frac{n_m^2 - n_a^2}{n_m^2 + n_a^2}; \quad r_{a,m}^{TE} \approx 0 \end{aligned} \tag{116}$$

Eq. (58)-(61) can then be simplified to:

$$K_{vertical,\lambda}^{TM} \approx \frac{3\sigma\varepsilon\ \kappa \exp(-2\kappa d)}{n_a k_0^3 [(-\sigma^2 + \varepsilon^2 + n_a^2)^2 + 4\sigma\varepsilon]} \tag{117}$$

$$K_{horizontal,\lambda}^{TM} \approx \frac{3\sigma\varepsilon\ \kappa \exp(-2\kappa d)}{2 n_a k_0^3 [(-\sigma^2 + \varepsilon^2 + n_a^2)^2 + 4\sigma\varepsilon]} \tag{118}$$

$$K_{vertical}^{TE} \approx K_{horizontal}^{TE} \approx 0 \tag{119}$$

With this approximation, the integral in eq. (102) can be analytically solved. The relative power radiated by the near-field is then given by:

$$P_{vertical,\lambda}^{near\ field} = \frac{3\sigma\varepsilon \exp(-2k_0 n_a d)\left(\frac{1}{2} + k_0 n_a d + k_0^2 n_a^2 d^2\right)}{n_a k_0^3 d^3 [(-\sigma^2 + \varepsilon^2 + n_a^2)^2 + 4\sigma\varepsilon]} \tag{120}$$

$$P_{horizontal,\lambda}^{near\ field} = \frac{3\sigma\varepsilon \exp(-2k_0 n_a d)\left(\frac{1}{2} + k_0 n_a d + k_0^2 n_a^2 d^2\right)}{2 n_a k_0^3 d^3 [(-\sigma^2 + \varepsilon^2 + n_a^2)^2 + 4\sigma\varepsilon]} \tag{121}$$

For small distances $k_0 n_a d \ll 1$ and for small absorption coefficients $\varepsilon \ll \sigma$ Eq.(120)-(121) are reduced to:

$$P_{vertical,\lambda}^{near\ field} = \frac{3}{2} \frac{\sigma\varepsilon}{n_a k_0^3 (-\sigma^2 + n_a^2)^2} \frac{1}{d^3} \tag{122}$$

$$P_{horizontal,\lambda}^{near\ field} = \frac{3}{4} \frac{\sigma\varepsilon}{n_a k_0^3 (-\sigma^2 + n_a^2)^2} \frac{1}{d^3} \tag{123}$$

The near-field absorption for small distances between a dipole and an absorbing metal is proportional to d^{-3}, as previously derived in [17]. The formula above gives the detailed dependency of the near-field absorption on n_a and the optical properties of the metal.

Figure 3.17 compares the large κ approximation (Eq.(117)) to the original formula (Eq.(58)) with $d = 20nm$ and $\varepsilon = 2$. For large values of κ the approximated formula approaches the original equation. The integrated power emitted into waves with a large wave vector is given in Eq.(122) and is proportional to ε.

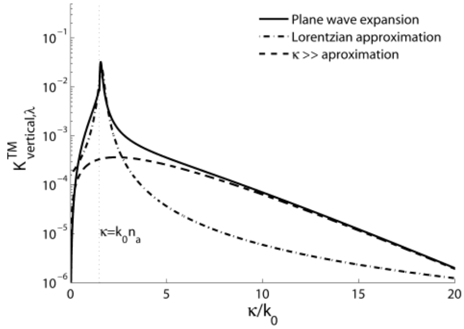

Figure 3.17 :Comparison of the large κ approximation (Eq.(117)) to the plane wave expansion (Eq.(58)) for a vertical dipole. The approximation matches the original formula for large κ.

3.2.3.3 Evanescent waves for an OLED example

Using the formulas described in the sections above we can calculate the radiative contributions of dipoles near metallic surfaces for all kinds of situations. As an example we will calculate the radiation of an electric dipole antenna in tris (8-hydroxyquinoline) aluminium(AlQ_3) near a planar Al surface, because these materials are often used in organic light emitting diodes(OLEDs) where AlQ_3 serves as an emitting material near an Al cathode.

We consider light with a wavelength $\lambda = 530nm$ which is the maximum of the emission spectrum of AlQ_3 [37]. At this wavelength the respective refractive indices of AlQ_3 and Al are $n_{AlQ_3} = 1.70$ [37] and $n_{Al} = -0.88 + 6.45j$ [38].

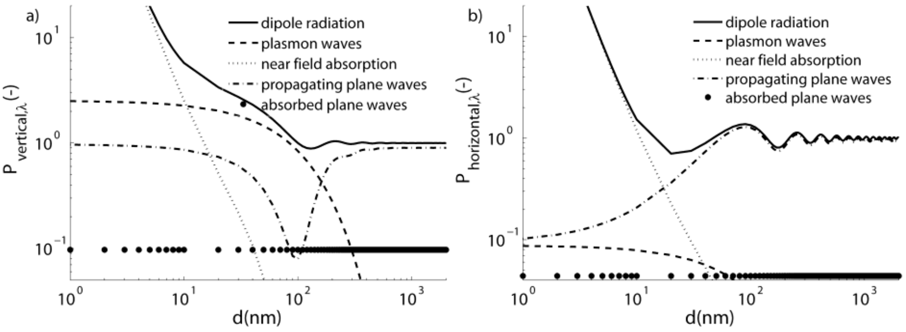

Figure 3.18 :Power radiated by a dipole in AlQ_3 near a planar Al surface for λ=530nm for a vertical(left) and a horizontal(right) dipole.

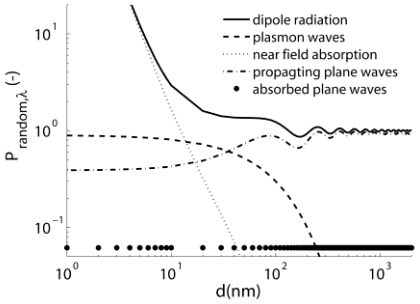

Figure 3.19 :Average power radiated by an ensemble of randomly oriented dipoles in AlQ_3 near a planar Al surface for λ=530nm.

In Figure 3.18 and Figure 3.19 the radiation into various channels is given as a function of the distance to the metal for a vertical (Figure 3.18a) and a horizontal dipole (Figure 3.18b) as well as the radiation by an ensemble of randomly oriented dipoles (Figure 3.19) for $d = 1..2000 nm$. For $d > 50 nm$ most of the light is radiated into propagating plane waves showing the typical oscillating pattern caused by WAI. This means that a dipole located at a maximum of this pattern will have enhanced radiation (and a higher decay rate) compared to a dipole in infinite AlQ_3 , a dipole that is located in a minimum will experience decreased radiation [17]. The coupling of evanescent waves to the metal is more important than the plasmon coupling when $d < 15 nm$. The coupling to the plasmon is important up to 200 nm.

3.3 Anisotropic emitters and organic layers

In the previous section we have analyzed the radiation of dipole emitters in isotropic OLEDs. The efficiency of the device can be improved by tuning the interference effects inside the microcavity and avoiding coupling to the cathode. But $\eta_{out,sub}$ remains limited to around 40% (see Figure 3.14b). In this section we discuss the use of oriented materials to further improve $\eta_{out,sub}$.

3.3.1 Oriented emitters for improved outcoupling

The emission of a dipole antenna is mainly directed around a plane perpendicular to the dipole moment (see Figure 3.20a). Along the dipole axis no power is emitted.

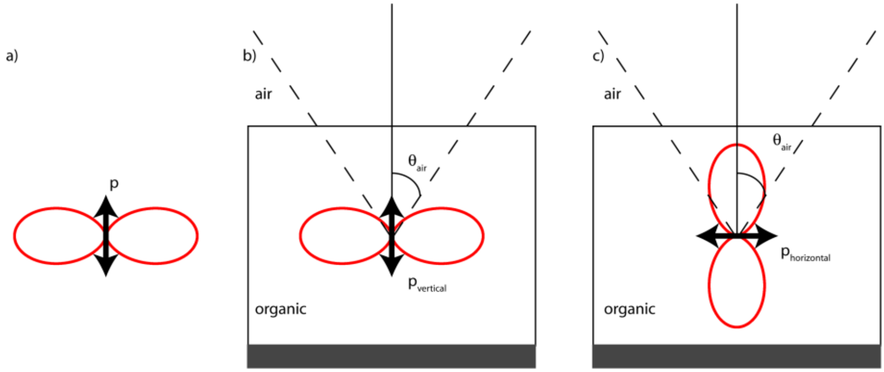

Figure 3.20 Angular emission pattern of a dipole antenna. a) dipole in an infinite medium. b) A vertical dipole in an OLED (without interference effects) c) A horizontal dipole in an OLED (without interference effects)

In Figure 3.20b) and c) the dipole is shown in an optically thick organic layer bounded by a metal mirror and air. When the dipole moment is perpendicular (a vertical dipole) to the layer interfaces (Figure 3.20b)), most light is radiated into angles outside the escape cone to air. When the dipole is parallel (a horizontal dipole) to the layer interfaces the emission pattern is more directed into the escape cone to air.

Most emitter materials used in OLEDs have a dipole moment which is randomly oriented. The emission from an ensemble of randomly oriented dipoles is modelled by averaging over all dipole directions. It can be shown that this average over all angles is equal to averaging the power emitted by three perpendicular dipoles: 1 vertical dipole and 2 horizontal dipoles (perpendicular to each other) [17]. Furthermore when the OLED is cylindrically symmetric the two horizontal dipoles are only different by a 90° rotation around the axis of the cylinder. For an ensemble of randomly oriented dipoles, the average F_{rnd} and all related qualities can be found by:

$$F_{rnd} = \frac{1}{3}F_{\perp} + \frac{2}{3}F_{\|} \tag{124}$$

It is clear from Figure 3.20 that an emitter which orients horizontally will radiate a greater portion of its light into the escape cone than a random one. Using oriented emitters the outcoupling efficiency can be greatly enhanced.

Oriented emitters have been reported in polymer OLEDs [39, 40], where the long polymer chains have a preferred orientation. But also in evaporated small molecule OLEDs oriented emitters can be found [41-43].

3.3.1.1 Outcoupling efficiency vs. degree of orientation

For a dipole with an angle ν to the direction normal to the layer interfaces, F is calculated from its projection onto parallel $F_{\|}$ and perpendicular $F_{\perp}$ dipoles [17]. This can be understood through the following argument. First consider an individual dipole antenna $\mathbf{p}$ with arbitrary inclination angle ν and azimuth angle ζ. For this dipole F can be expressed as the scalar product of the dipole moment with the imaginary contribution of the electric field at the location of the dipole [16]. The electric field can be expressed as the scalar product of a Greens tensor $\overline{\overline{G}}$ and the dipole moment (the exact form of this tensor is not important for this argument) [18].

$$F = \mathbf{p}.\mathrm{Im}\left[\mathbf{E}(\mathbf{r}=0)\right] = \mathbf{p}.\mathrm{Im}\left[\overline{\overline{G}}\right].\mathbf{p} \tag{125}$$

$\mathbf{p}$ can be written as a linear combination of $\mathbf{p}_x$, $\mathbf{p}_y$ and $\mathbf{p}_z$. And eq. (125) becomes:

$$F = \sum_{i=x,y,z}\ \sum_{j=x,y,z} G_{ij}p_i p_j \tag{126}$$

Where p_i is the projection of $\mathbf{p}$ on the i-axis. If we now consider the average power emitted by an ensemble of dipoles with the probability distribution ($\int_{\nu=0}^{\pi/2}\int_{\zeta=0}^{2\pi} H(\nu)\sin\nu d\nu d\zeta = 1$), we assume the dipole distribution is invariant to rotation around the z-axis.

$$F_{avg} = \int_{\nu=0}^{\pi/2} \int_{\zeta}^{2\pi} H(\nu) \sum_{i=x,y,z} \sum_{j=x,y,z} G_{ij} p_i(\nu,\zeta) p_j(\nu,\zeta) \sin\nu d\nu d\zeta \quad (127)$$

All cross-terms ($i \neq j$) contain a factor $\cos(\zeta)$ or $\sin(\zeta)$ and become zero upon integration over ζ (since the distribution is symmetric to rotation around z). Furthermore $G_{xx} = G_{yy}$ because of the symmetry of the OLED and eq. (127) reduces to:

$$F_{avg} = 2\pi \int_{\nu=0}^{\pi/2} (F_{\perp} \cos^2 \nu + F_{\|} \sin^2 \nu) H(\nu) \sin\nu d\nu \quad (128)$$

Eq.(128) can be simplified by introducing:

$$\alpha = 2\pi \int_{\nu=0}^{\pi/2} \sin^3 \nu H(\nu) d\nu \quad (129)$$

α is the fraction of effectively parallel emitters (in a random emitter $H(\nu)=1$ and $\alpha = 67\%$). F_{avg} is written as:

$$F = \alpha F_{\|} + (1-\alpha) F_{\perp} \quad (130)$$

When $\alpha = 100\%$ all dipoles are horizontal, $\alpha = 0\%$ corresponds to completely vertical dipoles. For a random emitter $\alpha = 67\%$.

The degree of orientation is taken into account in quantities like $I_{sub/air}$, $P_{sub/air}(\theta)$ in eq.(130)-(132). Eq. (124) is a special case of this weighted average for $\alpha = 67\%$.

$$I_{sub/air} = \alpha I_{sub/air,\|} + (1-\alpha) I_{sub/air,\perp} \quad (131)$$

$$P_{sub/air} = \alpha P_{sub/air,\|} + (1-\alpha) P_{sub/air,\perp} \quad (132)$$

And accordingly for EQE, η_{rad} and η_{out}.

$$\eta_{out,i}(\alpha) = \frac{\alpha I_{i,\|} + (1-\alpha) I_{i,\perp}}{\alpha F_{\|} + (1-\alpha) F_{\perp}} \quad (133)$$

With these equations η_{out} can be calculated for various degrees of orientation. In Figure 3.21 $\eta_{out,sub}$ and $\eta_{out,air}$ is drawn for the green OLED from previous simulations. The OLED structure is depicted in Figure 3.11.

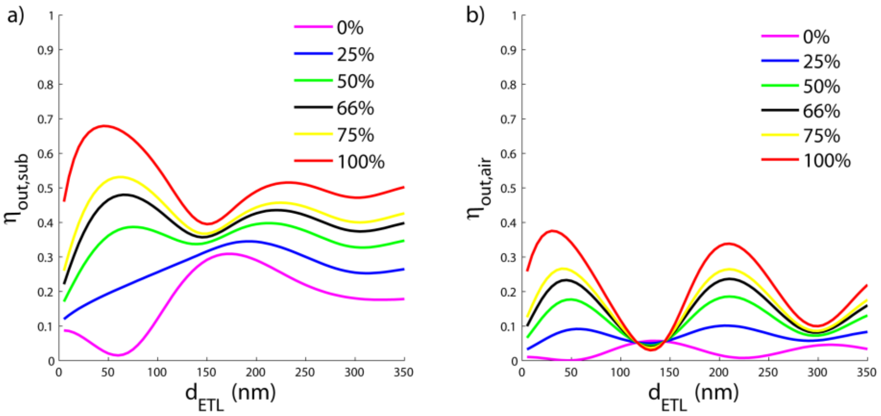

Figure 3.21 : η_{out} vs. d_{ETL} for various α for outcoupling (a) to the substrate and (b) to air. Simulation for the green OLED in Figure 3.11.

Figure 3.21 a) shows the outcoupling to the substrate. We see that the maximum $\eta_{out,sub}$ is 68% for $\alpha = 100\%$ and $d_{ETL} = 45nm$. For a randomly oriented emitter ($\alpha = 67\%$) the maximum $\eta_{out,sub}$ is 48%. As α decreases the maximum $\eta_{out,sub}$ shifts towards a thicker ETL. This is because vertical dipoles couple more strongly to plasmon modes [12]. As more vertical dipoles are present it becomes more important to avoid coupling to plasmons and the maximum $\eta_{out,sub}$ is obtained for thicker ETL layers. The maximum $\eta_{out,sub}$ for $\alpha = 100\%$ is a factor 1.42 higher than the maximum $\eta_{out,sub}$ for $\alpha = 67\%$.

Figure 3.21b shows $\eta_{out,air}$ as a function of ETL for various α. Again we see the maximum $\eta_{out,air}$ is highest for completely horizontal emitters. Again the first maximum shifts to thicker ETL for more vertical emitters. The maximum $\eta_{out,air}$ for $\alpha = 100\%$ is a factor 1.46 higher than the maximum $\eta_{out,air}$ for $\alpha = 67\%$.

In both figures a first and second maximum is seen. In air both maxima are about equal in height. In the substrate $\eta_{out,sub}$ is higher for the first maximum. This means that emitters in the first maximum will be more efficient when a substrate to air outcoupling foil is applied.

3.3.2 Determining orientation via decay time measurement

Not only the angular distribution but also F, the total emitted power, depends on the orientation of the dipole [44]. This is caused by the difference in the phase and polarization of the emission of vertical and horizontal dipoles. The F vs. d_{ETL} curve for different α is shown in Figure 3.22. The simulation configuration is the one shown in Figure 3.11.

A vertical dipole ($\alpha = 0\%$) couples strongly to the plasmon waves (see section 3.2.3.1) and F is large for vertical dipoles close to the cathode. For larger d_{ETL}, F shows a wavy curve due to WAI. For vertical dipoles F reaches a local maximum around 180nm from the cathode.

A horizontal dipole ($\alpha = 100\%$) couples weakly to the plasmon waves and F is relatively low for small d_{ETL}. For ETL thicknesses of around 60 and 230nm (see Figure 3.21) WAI causes a local maximum in F.

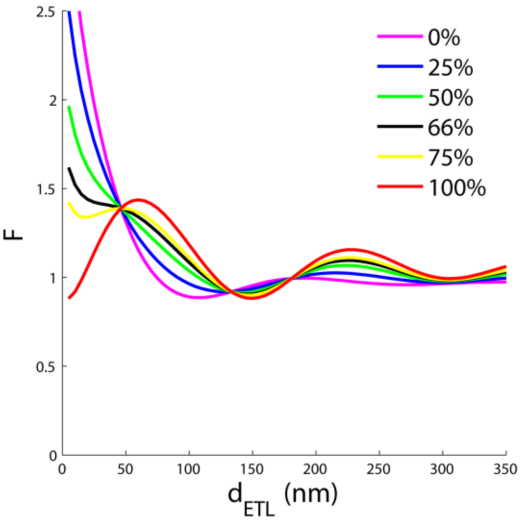

Figure 3.22 F as a function of ETL thickness for various degrees of horizontal orientation. Horizontal dipoles show weak coupling to plasmon waves and stronger interference effects. Vertical dipoles couple strongly to plasmons, the interference peak is less pronounced.

In section 2.5 the influence of F on the exciton decay rate and radiation efficiency has been discussed. Eq. (84) shows that the total decay rate Γ_{tot}

varies linearly with F. For oriented emitters the dependence of Γ_{tot} on α is given by:

$$\Gamma_{tot} = \left[\alpha F_{\parallel} + (1-\alpha) F_{\perp}\right] \Gamma_{r,0} + \Gamma_{nr} \tag{134}$$

When Γ_{tot} is measured for samples with different d_{ETL} the Γ_{tot} vs. d_{ETL} dependency will reveal the relative weight of horizontal and vertical dipoles. This dependency allows us to determine the degree of orientation of emitters in OLEDs experimentally. The measured Γ_{tot} vs. d_{ETL} curve should be well reproduced by a simulated curve where α, Γ_r and Γ_{nr} are fitted.

As an example the decay rate of Ir:(MDQ)$_2$(acac) and Ir:(ppy)$_3$,two popular OLED emitters, have been measured for the structure depicted in Figure 3.23. The fabrication and measurement of these samples was done by Frank Steinbacher and Ralf Krause from Siemens in Erlangen (Germany).

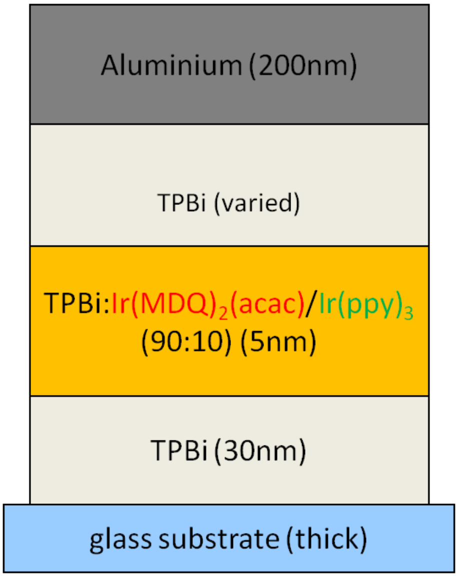

Figure 3.23 Organic layer stack used for decay time measurement with oriented emitters. The distance to the metal mirror is varied by changing the TPBi spacer thickness (0-120nm).

The samples are excited by a pulsed laser (0.5ns pulse width) with wavelength λ = 371 nm. TPBi was used as a host material because it shows low absorption at λ = 371 nm. The decay of photoluminescent intensity is measured by time-correlated single photon counting (TCSPC)[45]. A monochromator is used to measure at a specific wavelength and avoid detecting spurious luminescence of other materials. Figure 3.24 shows the measured decay of the green emission of Ir(ppy)$_3$ at λ = 510 nm and the red emission of Ir(MDQ)$_2$(acac) at λ = 600 nm.

The laser pulse excites a certain amount of molecules N_{exc} in the organic layers. After the pulse the exciton will decay back to the ground state. The excitons can hop from molecule to molecule, with slightly different states, in the EML layer before decaying back to the ground state. The emitted intensity does not show a decay rate specific for a single excited state, but the decay rate is an average over all possible states, this is known as homogeneous broadening. The result of homogenous broadening is that an ensemble of excitons exhibits a single decay rate and the measured intensity decay is a mono-exponential curve. The amount of excitons at a time t is given by:

$$N_{exc} = N_{exc,0} \exp(-\Gamma_{tot} t) \tag{135}$$

Two measured decay curves of Ir:(ppy)$_3$ and Ir:(MDQ)$_2$(acac) are shown in Figure 3.24 as an example. It is seen that the decay is in good approximation mono-exponential

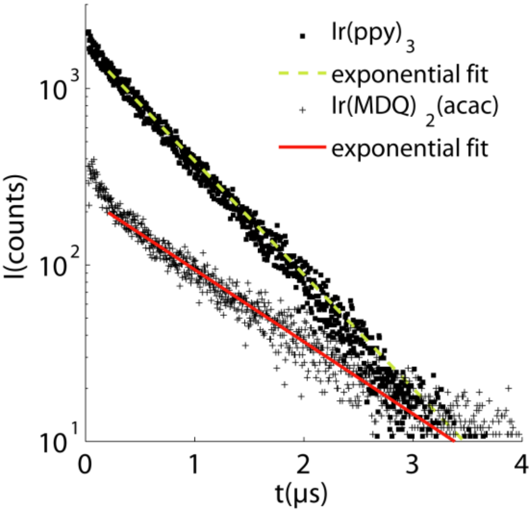

Figure 3.24 Example photoluminescent time decay signals. The characteristic decay rate is determined by fitting with an exponential curve. The characteristic decay time is determined with an accuracy of $\pm 0.01 \mu s$.

If we now compare the decay rates for various ETL thicknesses (and thus various F). The calculated $F_\perp$ and $F_{||}$, which are functions of the TPBi thickness, can be used to estimate α, $\Gamma_{r,0}$ and Γ_{nr} by fitting with Eq. (134) .

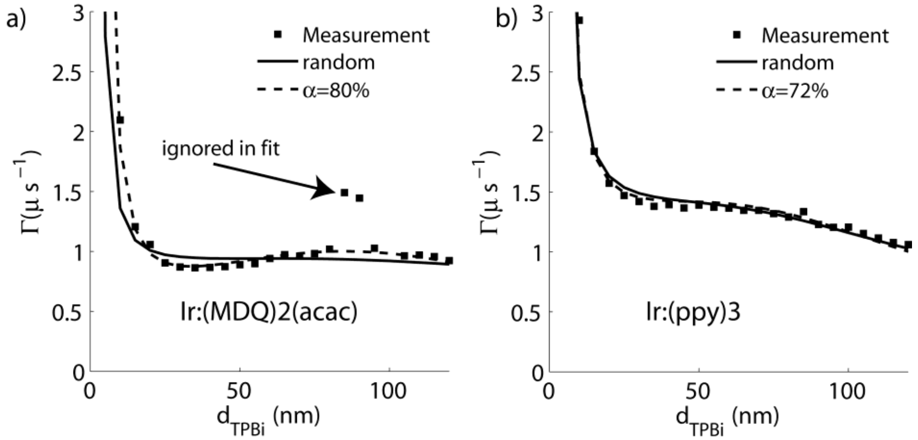

Figure 3.25 a) Measured and fitted decay rates for Ir(MDQ)$_2$(acac). With $\alpha = 80\%$ the measured decay rates are reproduced very well. With random emitters no convincing fit is obtained. b) Measured and fitted decay rates for Ir(ppy)$_3$. With $\alpha = 72\%$ the measured decay rates are reproduced very well. With random emitters the fit is reasonably well.

Figure 3.25 shows the measured and simulated (fitted) Γ_{tot} as a function of ETL thickness d_{TPBi}. The decay rate for Ir(MDQ)$_2$(acac) is fitted in Figure 3.25a) . When random emitters (solid curve) are assumed the simulated decay rate is unable to reproduce the measured results. When α is included as a fit parameter (dashed curve) the measured Γ_{tot} is very well reproduced. A preferential orientation of $\alpha = 79\%$ is found for Ir(MDQ)$_2$(acac). The best fit values of α, $\Gamma_{r,0}$ and Γ_{nr} are given in Table 3. The mean square error (MSE) is given for each fit as a measure for the quality of the fits. A small MSE means the simulation resembles the measurement well.

Figure 3.25b) shows the measured and simulated decay rate for Ir(ppy)$_3$. Both fits with random (solid curve) as oriented dipoles (dashed curve) describe the measurements well. Furthermore the oriented fit yields a near random($\alpha = 72\%$) dipole distribution. In the case of Ir(ppy)$_3$ a random dipole distribution is sufficient to accurately describe the dipole emission.

Table 3 : Best fit parameter values of α, $\Gamma_{r,0}$ & Γ_{nr}. MSE is a figure of merit for the quality of the fit.

Emitter	$\Gamma_{r,0}(\mu s^{-1})$	$\Gamma_{nr}(\mu s^{-1})$	$\alpha(\%)$	*MSE*
Ir(MDQ)$_2$(acac)	0.76	0	79	0.0008
Ir(MDQ)$_2$(acac)	0.26	0.59	67 (fixed)	0.010
Ir(ppy)$_3$	1.03	0	72	0.0017
Ir(ppy)$_3$	0.86	0.21	67(fixed)	0.0021

The measured decay rate is reproduced by the simulation with a standard deviation of $\pm 0.026\mu s^{-1}$. If we ascribe this small discrepancy solely to an uncertainty in the parameter α, then $\alpha = (79 \pm 5)\%$. If also a small error in the determination of $\Gamma_{r,0} = (0.76 \pm 0.01)\mu s^{-1}$ is assumed, then $\alpha = (79 \pm 2)\%$. This error for determining α is the same as for results obtained by analysis of the emitted spectrum versus angle [46].

3.4 Conclusion

The fundamental properties of OLEDs are explained in this chapter. Efficient light emission requires: formation of excitons by balanced injection of holes and electrons, all excitons should be capable to recombine using phosphorescent emitters, non-radiative emission should be as low as possible and finally the generated photons should be able to escape from the device.

In a standard planar OLED only 20% of the light is emitted to the outside world, the remaining 80% is trapped in the organic layers and the substrate. For efficient light outcoupling, light should be radiated in the escape cone. Trapped light can be outcoupled by scattering in the organic layers and the substrate. Furthermore absorption losses should be avoided where possible to increase the outcoupling after multiple reflections as much as possible.

The PWE is a fast modelling tool for the light emission from OLEDs. By tuning the interference effects (mainly due to reflection from the cathode) inside the cavity the angular emission can be directed into the escape cone. Additionally losses by excitation of plasmon waves and near-field absorption should be avoided. Analytical formulas for the coupling to plasmon waves and near-field absorption have been derived.

Some emitter materials have a preferential orientation of the emissive dipole moment. Dipoles with in-plane orientation emit more light into the escape cone than perpendicular dipoles. Additionally coupling to plasmon waves is reduced in horizontal dipoles. The orientation of dipoles can be determined by analyzing the luminescent decay signal of the emitter in different microcavities. This technique has been demonstrated for an oriented small molecule emitter $Ir(MDQ)_2(acac)$ and a random emitter $Ir(ppy)_3$. The outcoupling behaviour of oriented emitters has been compared to that of random emitters. Fully horizontal emitters can increase the outcoupling efficiency to the substrate from 48% to 68% and to air from 24% to 38%, for a reference green OLED.

4. Light emitting Cholesteric Liquid Crystals

This chapter is devoted to light emission from cholesteric liquid crystals (CLCs). The first section gives an introduction and overview of the nature and applications of CLCs. Then we turn our attention to the simulation and measurement of light emission from CLCs. Finally the modelling and design of cholesteric liquid crystal lasers is discussed.

4.1 Introduction

Liquid crystals are mainly known for their use in flat-panel displays. Liquid crystal displays are without question the most widely used display technology. The molecular ordering and electro-optic properties of liquid crystals also offer many opportunities for other optical devices. For example tuneable filters [47], tuning and trimming of waveguide devices [48], luminescent solar concentrators for smart windows [49, 50] and OLEDs [39, 51, 52].

This chapter is focussed on cholesteric liquid crystals and will only introduce those concepts required to understand the material presented in this chapter. Many books on the properties of liquid crystals are available. For a broader discussion of liquid crystals it is advised to consult reference works, for example [53, 54].

In this chapter we can consider a liquid crystal in the nematic state as a uniaxial material, with the extra-ordinary axis parallel to the LC-director. The origin of this uniaxial behaviour lies in the shape of the LC molecules. The molecules of a nematic liquid crystal have a cigar-like shape[53, 54]. Other types of liquid crystal can have different shapes such as disk or curved like a banana. Some examples of possible liquid crystal molecule shapes are shown in Figure 4.1.

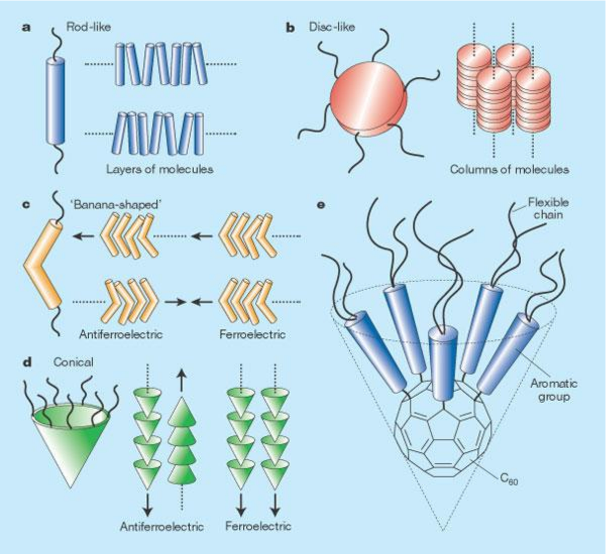

Figure 4.1 :Example of some liquid crystal phases. Liquid crystal molecules exist in many shapes: rods, discs, bananas, cones ... Original picture from [55].

The dielectric properties of the molecules are different in the directions along or perpendicular to the long axis of the molecule. This is the cause for the uniaxial anisotropy in nematic liquid crystals.

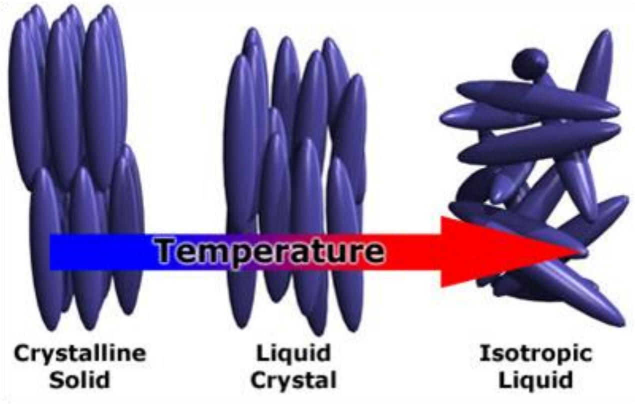

Figure 4.2 Phase transitions in thermotropic liquid crystals. Original picture from [5].

Thermotropic liquid crystals exhibit liquid crystal behaviour in a limited temperature range. When the temperature is too low the molecules are fixed in a lattice and the material is a solid. Above the melting point, the material is liquid but the long molecules tend to align in the same direction resulting in a macroscopic anisotropy, this is the nematic state. The orientation of the LC is given by the director $\mathbf{L}$. When the temperature is increased above the clearing point, the long molecules orient randomly. An individual molecule still has different properties along and perpendicular to the axis (microscopic) but the many molecules are randomly oriented. The macroscopic effect is that the material becomes a transparent isotropic liquid above the clearing point T_c. Apart from the nematic state, many other liquid crystal states like smecticA, smecticC, blue phase,... exist between the solid and isotropic state. In this chapter we only consider nematic and chiral nematic states.

4.1.2 Cholesteric liquid crystals

In chiral nematic or cholesteric liquid crystals the director (and thus the molecules) forms a screw-like structure (see Figure 4.3). For this reasons CLCs are also called chiral nematic liquid crystals. The molecules rotate a full $360°$ over a distance P, called the pitch. Some CLCs form a right-handed helix, others a left-handed helix. Some liquid crystals are cholesteric by nature, but nematic liquid crystals can be made cholesteric by adding a chiral dopant, to induce the helical rotation of the LC molecules.

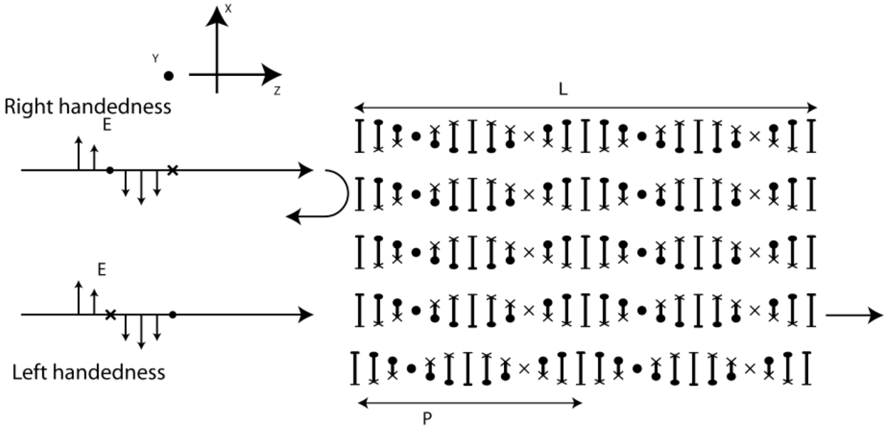

Figure 4.3 In a CLC the molecules are rotating in a screw-like structure. Circular polarized light with the same handedness is reflected. Dots and crosses are used to visualize the right handed helix formed by the molecules.

CLCs posses extra-ordinary optical properties. The rotation of the LC molecules creates a periodic refractive index profile, like in a dielectric mirror. When the period matches the wavelength of an incident lightwave, that wave is strongly reflected. The material is said to possess a one-dimensional photonic bandgap (PBG). The PBG is characterized by a band of high reflection in its reflection spectrum (see Figure 4.4). In a CLC the PBG only exists for circularly polarized light with the same handedness as the CLC. Circularly polarized light with opposite handedness passes through the CLC unhindered. The maximum reflection of a CLC for unpolarized light is thus limited to 50%.

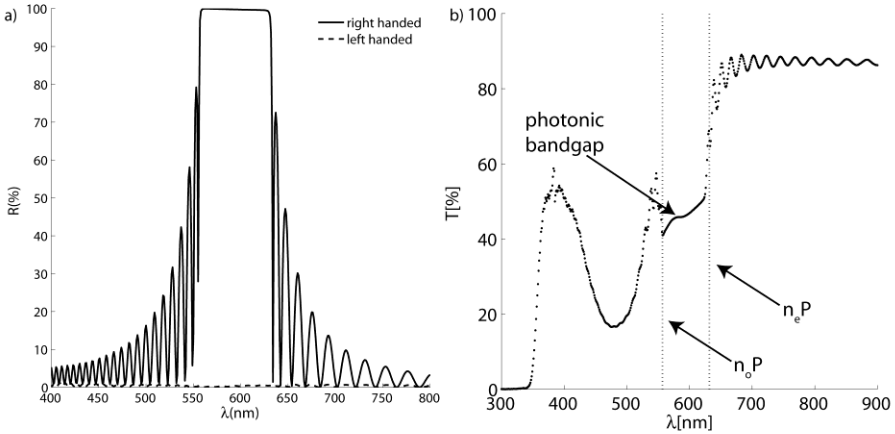

Figure 4.4 a) Simulated reflection of a CLC simulated for circular polarized light with right handed and left handed helicity b) Measured spectral transmission of a CLC for unpolarized light. Around $600nm$ the PBG limits the transmission to 50%.

4.1.3 Applications of CLCs

CLCs spontaneously form highly reflective films which are otherwise only achieved by carefully fabricated and well designed thin film stacks. Furthermore liquid crystals can be easily tuned by a number of means. The possibility of low cost, easily tuneable optical devices is the main motivation for the strong interest in CLCs over the years.

In applications CLCs can act as a passive component where it is used for its highly reflective and/or polarizing properties or as an active (emitting) component. Among the latter liquid crystal lasers are most promising.

4.1.3.1 Liquid crystal lasers

Laser emission in CLCs is realized by introducing a laser dye whose emission spectrum overlaps with the reflection band of the CLC. Liquid crystal lasing has also been achieved in other types of liquid crystals like smectic liquid crystals [56], polymer dispersed liquid crystals [57] and blue phases [58].

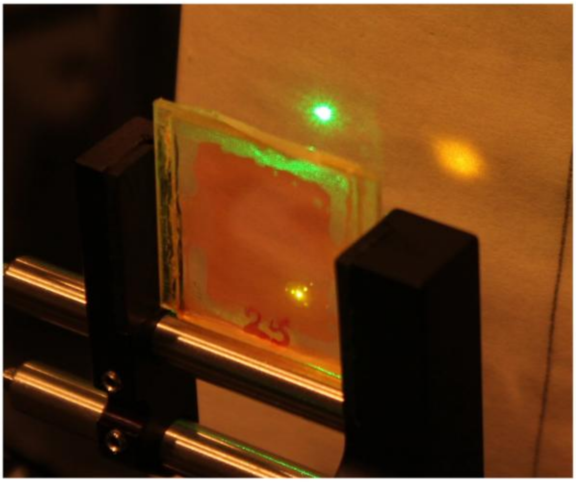

Figure 4.5 Lasing from a cholesteric liquid crystal. The material is pumped by the green laser and emits an orange laser beam. Picture taken from [59].

The driving force behind liquid crystal research is the very low fabrication cost of a liquid crystal laser cell [8]. In its simplest form a liquid crystal laser can be made by doping a liquid crystal with a small amount of laser dye (~1%) and a chiral dopant to induce a helix of the appropriate pitch. A cell consisting of two glass plates with an alignment layer and a few µm spacing is then filled with this mixture. The cell can be excited by wavelengths inside the absorption band of the laser dye. When the pump energy is sufficiently high the cell will emit laser light .

Another interesting feature of liquid crystal lasers is tuneability over a wide wavelength range. When the PBG of the CLC is tuned to different wavelengths, the laser emission is also tuned within the emission spectrum of the laser dye. Tuning can be achieved in a number of ways: by thermally [60] or mechanically [61] altering the pitch, by altering Δn [62] or by electrically tuning a liquid crystal defect layer [63]. Another tuning mechanisms is to move the emission spot in a cell with varying pitch[64].

Some hurdles still remain for the application of liquid crystal lasers in real devices. Currently liquid crystal lasers are pumped by high energy laser pulses. A lower threshold is needed to realize pumping by continuous wave (CW) or by LED. A second challenge is increasing the maximum power output. At high input power the laser dyes are bleached, leading to decreased output power and eventually destruction of the CLC laser[65, 66]. Finally the ultimate goal would be to achieve electrical pumping rather than optical pumping.

4.1.3.2 Reflective films for displays, ...

CLCs are very useful for filter applications because of their selective reflection properties. Most straightforward is their application in all kinds of reflective films. But the polarization selectivity can also be used in several other optical components.

Several ways exist to improve the reflectivity and bandwidth of CLC reflectors. Broadband reflection can be achieved by stacking CLC films with a different pitch. But also inside a single film by introducing a pitch gradient throughout the film [67]. Similarly reflection of both circular polarizations can be achieved by two CLC films of opposite handedness or by a single film containing CLCs of opposite handedness [68, 69]. CLCs can also be used as a polarization selective or converting component either alone or in combination with other optical components [70].

Another potential application for CLCs is in displays. Either as the reflecting element in a reflective display [71] or as a fast-switching (~0.1ms) liquid crystal in flexo-electric displays [72].

4.2 Spontaneous emission in CLCs

In this section spontaneous emission from dye molecules inside a CLC is analyzed [44]. The effect of the PBG on the spectrum and polarization of the emitted light is simulated and measured. Also the effect of dipole orientation and the profile of the electric field are simulated. In section 4.3 stimulated emission and lasing are modelled.

4.2.1 Interference effects in the CLC

The periodic variation of the director (with pitch P) creates a periodic variation in the dielectric tensor with period $P/2$. This one-dimensional variation generates a 1D photonic band gap (PBG) similar to a Bragg type mirror. The dispersion relation for the reflected circular polarization is drawn in Figure 4.6. Inside the PBG the refractive index of one of the eigenmodes of propagation becomes imaginary [73], meaning this mode becomes evanescent. The CLC acts as a perfect reflector for that mode.

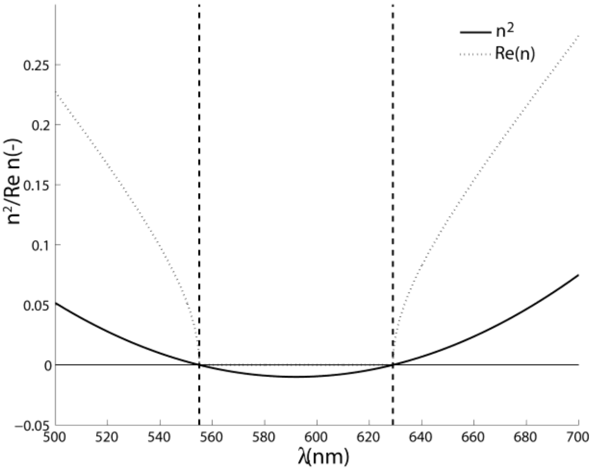

Figure 4.6 Squared refractive index and real part of the refractive index of the reflected mode around the PBG. For $n_o = 1.5$, $n_e = 1.7$ and $P = 370nm$. Inside the bandgap n^2 is negative and n is imaginary.

If the LC director rotates with right handedness, then the polarization with right handedness is reflected in a certain spectral region [53], the PBG. For an infinitely thick CLC, the reflection band in the perpendicular direction is defined by $n_o P < \lambda < n_e P$ where n_o and n_e are the ordinary and extra-ordinary refractive indices of the liquid crystal.

The PBG has a remarkable effect on the light emission of dye molecules inside the CLC. Because evanescent waves do not carry any power (in a loss free medium), no light can be emitted in the PBG. Another interpretation is that the density of states in the PBG is zero (at least in the perpendicular direction) and as a result, the excited dye molecule cannot decay via emission of a photon with wavelength and polarization in the PBG.

Just outside of the PBG, waves can be emitted. At the edge of the PBG the reflection coefficient oscillates rapidly with the wavelength (see Figure 4.4). Here the emitted light is subjected to strong interference effects which depend on the thickness of the CLC. When the reflections are in phase, a peak will occur in the emission. When reflections are in anti-phase, a minimum will be seen. This can also be interpreted as an increase/decrease in the optical density of states.

The spectrum emitted by a fluorescent dye perpendicular to the substrate can be calculated using the known eigenmodes of the CLC[74]. The CLC is characterized by the pitch P and the dielectric properties of the liquid crystal $\varepsilon_{avg} = (n_e^2 + n_o^2)/2$ and $\Delta\varepsilon = n_e^2 - n_o^2$.

The amplitude of the electric field of the plane wave component(in polarization state i) emitted by the dipole emitter at the location of the dipole is given by [75]:

$$E_{CLC,i}^{r} = \frac{E_{\infty,i}^{r} + r_i^l E_{\infty,i}^{l}}{1 - r_i^l r_i^r} \tag{136}$$

Assuming that the two circular polarization states are not coupled by any reflection. This condition holds for the eigenmodes (circular polarization) in the CLC. $r_i^{r/l}$ is the complex amplitude reflection coefficient (in the plane of the emitter) for a plane wave (amplitude $E_i^{r/l}$) travelling to the right or left in Figure 4.3 with polarization i.

When $\left|1 - r^l r^r\right|$ becomes zero, a discrete, infinite peak appears in the emitted spectrum. When $\left|1 - r^l r^r\right|$ is small a finite peak is visible. For the polarization where a PBG exists $r_i^{r/l}$ can be near unity and sharp peaks in the emission spectrum occur. For the polarization where no PBG exists, $r_i^{r/l}$ is small and the spectrum of a dye in an infinite medium will be emitted.

4.2.2 Plane wave modelling of the CLC

The emission from a CLC in the normal direction can be modelled with analytical methods [74]. However for more complicated optical designs (e.g. different director configurations or optical cavities) or emission in oblique angles the analytical approach becomes cumbersome. This is because the electric fields of the eigenmodes and/or reflection coefficients require lengthy calculations. In this section we simulate the emission from the CLC using the plane wave expansion method [75].

First the power emitted by a unit dipole $P(\lambda,\theta)$ in a given CLC stack is calculated for each angle and wavelength separately. The spectral density $S_{CLC}(\lambda,\theta)$ at an angle θ for a given CLC stack and dye is then obtained by weighting the emitted power with the normalized spectral density $S_0(\lambda)$ of the dye in the nematic liquid crystal E7, which is obtained by measuring the emission of a cell filled with a non-chiral mixture:

$$S_{CLC}(\lambda,\theta) = S_0(\lambda) P_\lambda(\lambda,\theta). \tag{137}$$

The cell is treated as a series of discrete slabs, each slab is characterized by its thickness, the refractive indices and the orientation of the optic axis (see Figure 4.7). Here 18 slabs per pitch are used, so the optical axis in each slab is rotated over 20° compared to the previous slab. The entire CLC thickness is assumed to be 18 pitches long. The two refractive indices of the CLC mixture are assumed to be equal to those of undoped E7 since only a small amount of dopant is added. In the simulation $P = 365nm$ is used, because for this pitch the simulated spectrum matches the measured spectrum best. The CLC region is bound by a 158nm ITO layer and a thick glass substrate on each side and the emission into the glass substrate is calculated. Alignment of the liquid crystal is assured by a rubbed polyimide layer on each side of the cell, because this layer is only a few nm thick (and has a refractive index comparable to the LC) it is ignored in simulation.

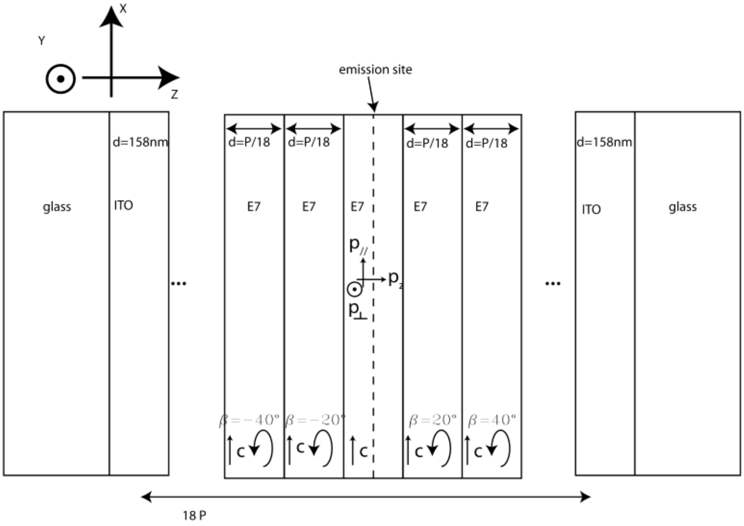

Figure 4.7 Layered approximation of the CLC structure. The CLC is divided in a series of thin slabs with a uniform optical axis. Three dipole orientations are simulated.

Simulations are carried out for three orientations of the transition dipole moment: $\mathbf{p}_{//}$ parallel to the local LC director, $\mathbf{p}_{\perp}$ perpendicular to the local LC director and the z-axis and $\mathbf{p}_{Z}$ parallel to the z-axis. The degree of molecular orientation of the dye along the LC director is expressed via the order parameter S_{dye}. A distribution of dipoles can be decomposed in 3 contributions (analogous to eq.(128)), parallel/perpendicular to the director and along the z axis. In this way the distribution is modelled considering 3 dipole orientations, with respective weights $\# p_{//}$, $\# p_{\perp}$ and $\# p_z$ [17, 43]. S_{dye} is given by Eq.(138). In this formula we assume $\# p_{\perp} = \# p_z$, this corresponds to a uniform distribution of dipoles in the plane perpendicular to the extra-ordinary axis and $\# p_{//} / \# p_{\perp} = \rho$.

$$S_{dye} = \frac{3 < \cos^2 \theta > -1}{2} = \frac{3 \frac{\# p_{||}}{\# p_{||} + 2\# p_{\perp}} - 1}{2} \tag{138}$$

θ is the angle between the dipole moment and the LC director. When the dipole moment is randomly oriented $S_{dye} = 0$. When the dipole moment aligns perfectly parallel (or perpendicular) to the director, S_{dye} becomes 1 (or -1/2). The order parameter is accounted for in simulations by taking a weighted average over the three dipole moments. The relative weight for the three dipoles is estimated by the measurement of the linear polarization ratio $I_{//} / I_{\perp} = \# p_{//} / \# p_{\perp}$ in the non-chiral mixture. The emission for a cell, homogeneously doped with dye molecules, is found by incoherently adding the powers emitted by a representative ensemble of dipoles, namely three orthogonal dipoles in the middle of each slab of the CLC.

4.2.3 Emission in the normal direction

4.2.3.1 Experimental procedure

To verify the results of the simulation model, the fluorescent spectrum of a CLC doped with a fluorescent dye has been measured. In the following paragraphs we briefly describe the measurement of the emitted spectrum and polarization.

A mixture of the nematic liquid crystal E7 (Merck) with a chiral dopant BDH1305 (Merck) and a laser dye DCM (Exciton) is used. The three materials are mixed in a ratio of 94.03/5.07/0.9 % by weight respectively. The chiral dopant induces a pitch in the nematic E7 and the DCM-dye provides the photoluminescence. To determine the molecular order parameter S_{dye} of the dye, a mixture without chiral dopant is made.

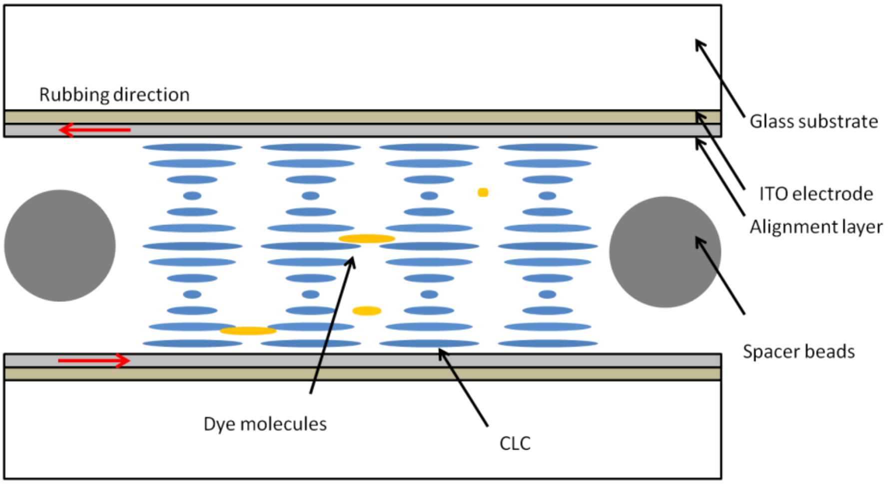

Figure 4.8 Structure of a liquid crystal cell with CLC. The cell consists of two glass substrates separated by spacer beads. Alignment at the surface is assured by rubbed alignment layers.

The mixtures are filled into single pixel cells (see Figure 4.8) by capillary action. The cells consist of two parallel glass plates, each covered with an ITO electrode and a planar alignment layer. The glass plates are separated by 6.8µm spacers and the rubbing direction is anti-parallel. The cells are filled at 70°C and then slowly cooled to room temperature. Slow cooling is performed to reduce the formation of multiple LC domains inside a cell.

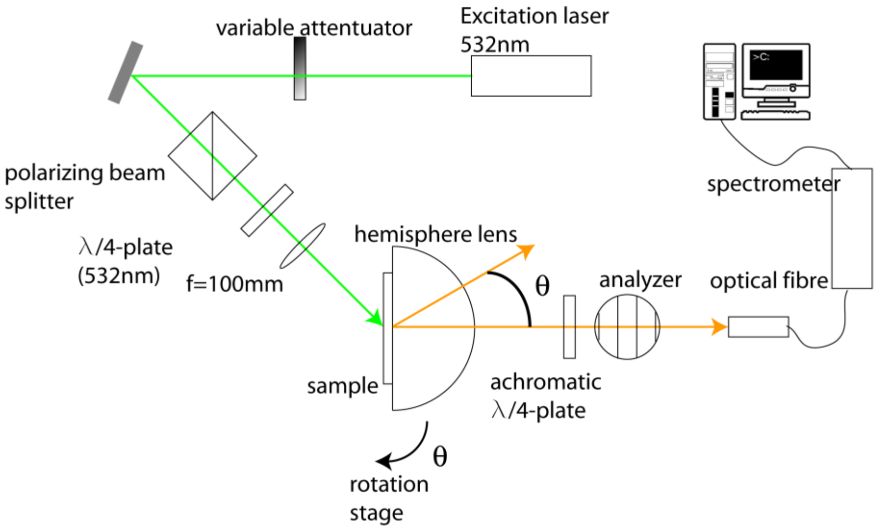

Figure 4.9 Spectral fluorescence measurement setup. The sample is excited by a circularly polarized laser beam. The emitted spectrum is detected by a spectrometer. The sample is placed on a rotating stage and optically coupled to a hemispherical lens.

The transmission spectrum at normal incidence is measured with a transmission spectrophotometer (Perkin Elmer Lambda 35). The emission spectrum is measured using the setup depicted in Figure 4.9. A CW frequency doubled Nd:YAG laser ($\lambda = 532nm$) is used to excite the sample. The laser is passed through a variable attenuator to control the incident power and a polarizing beam splitter cube and quarter wave plate to ensure left-handed circular polarization of the excitation beam. A left handed circular polarized beam avoids reflection by the bandgap (which shifts to shorter wavengths for oblique incidence) and thereby ensures a more uniform absorption of the excitation beam. The beam is then focussed onto the sample by a lens. The sample is mounted onto a rotating stage to detect emission into different inclination angles θ .

A glass hemisphere allows the measurement of light emitted under angles which are otherwise trapped in the glass substrates by total internal reflection. The hemisphere is optically coupled to the sample using an index matching gel. The refractive indices of the coupling gel, glass in the cell and the hemisphere are roughly the same. This technique allows to measure the emission into the glass substrate with minimal reflection at the glass/air boundary, since any ray emitted from the centre of the hemisphere impinges normally on the hemisphere surface. The emitted light is collected by an optical fibre and detected using a spectrometer (Qwave 390-950nm).

To measure the degree of left and right handed circular polarization, an achromatic quarter wave plate and rotatable analyzer are placed in the path of the emitted light. For the measurement of the degree of orientation of the dye in the non-chiral mixture, the quarter wave plate is omitted. The angle between excitation and detection is fixed at 135° to spatially separate the excitation beam from the emitted fluorescence. The excitation beam is incident at 45° for the measurement at $\theta = 0°$.

4.2.3.2 Determining the order parameter for emission

Figure 4.10 shows the measured fluorescence spectra of the dye in pure E7 for a cell with homogeneous planar alignment for two different polarizations: parallel and perpendicular to the director. The ratio $I_{//} / I_{\perp}$ is obtained from the ratio of the two emissions. For DCM in E7 the ratio is only weakly dependent on the wavelength and $I_{//} / I_{\perp} = 3.7$. This corresponds to an order parameter $S_{dye} = 0.47$ (using eq. (138)). .

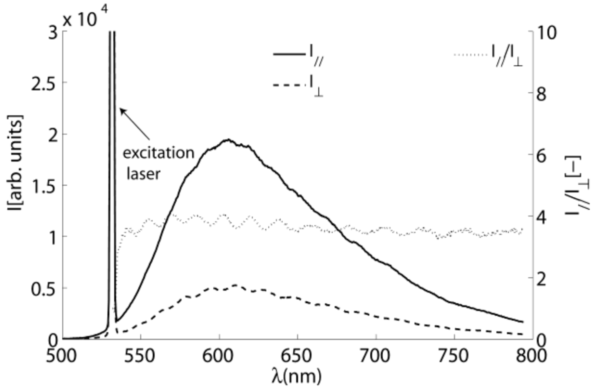

Figure 4.10 Emission spectra with polarization parallel and orthogonal to the director for DCM in E7 with homogeneous alignment. The dotted line gives the ratio of the two emission spectra.

4.2.3.3 Spectrum

Figure 4.11 displays the fluorescent emission from the CLC mixture in the normal direction. Figure 4.11a compares the simulated spectrum for dipoles oriented completely parallel (green dash-dotted curve), completely perpendicular (red dashed curve) and random (blue solid curve). It is seen that a dipole parallel to the LC couples dominantly to the peak on the long wavelength side of the PBG. For dipoles perpendicular to the LC, coupling to the short wavelength side is favoured. Randomly oriented dipoles couple to both peaks. In Figure 4.11b the measured spectrum is compared to the simulation for a random dipole (blue solid curve) and dipoles with order parameter $S_{dye} = 0.47$ (red dashed curve). The previously measured value $S_{dye} = 0.47$ yields a spectrum that more accurately matches the measured emission spectrum, in particular the peaks on the left and right hand side of the PBG.

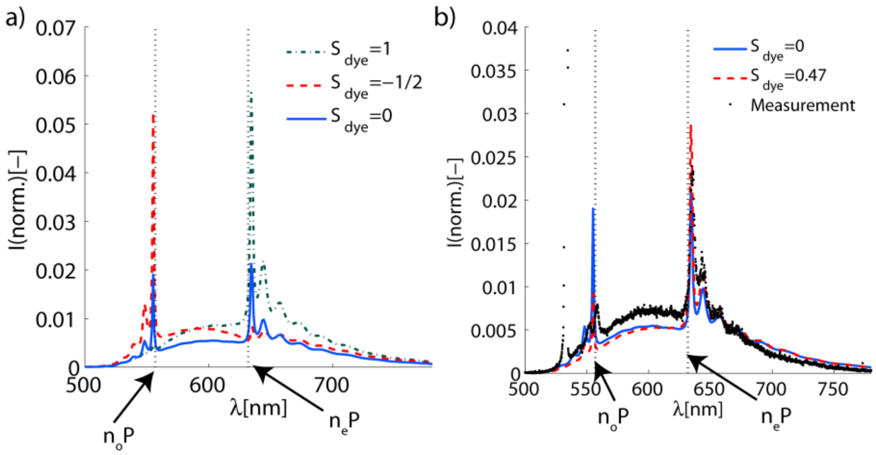

Figure 4.11 a) Simulation of emission in the normal direction for dipoles: parallel, perpendicular and random to the LC director ($S_{dye} = 1, -1/2, 0$) b) Measured emission spectrum vs. simulation. The simulation using the estimated $S_{dye} = 0.47$ matches the measured peak heights.

4.2.3.4 Polarization

The degree of circular polarization is expressed as the dissymmetry factor d_e.

$$d_e = 2\frac{I_l - I_r}{I_l + I_r} \tag{139}$$

$d_e = -2$ and $d_e = 2$ correspond to completely circularly polarized light, respectively with left and right handedness. Figure 4.12 plots the measured and simulated d_e. Inside the PBG only circular polarization with left handedness is emitted and d_e is close to -2. The dipoles at the borders of the cell only experience a PBG on one side and therefore contribute also to the other circular polarization. At the edges of the PBG the emission of circularly polarized light with right handedness is strongly enhanced, as a consequence the overall d_e becomes positive. The absolute value of d_e is not as high as inside the PBG region since all dipoles still emit into both circular polarization states.

Again the simulation which takes into account the order parameter (red dashed line) better matches the measured spectral dependency of d_e, in particular the relative height of the peaks at the right and left hand side of the PBG. For a randomly oriented dipole both peaks are equally excited and the polarization is symmetric around the centre of the PBG. For an emitter oriented along the LC director (higher S_{dye}), the long wavelength peak is more strongly excited and the long wavelength peak is more polarized.

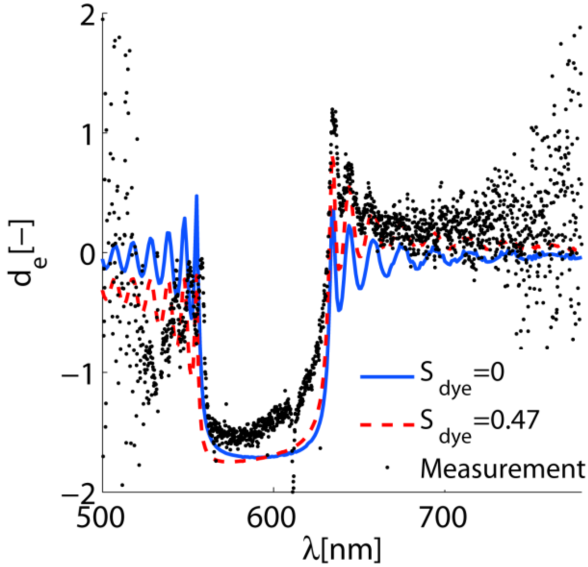

Figure 4.12 Measured and simulated dissymmetry factor d_e. $d_e = -2, 2$ correspond to circularly polarized light (respectively with left and right handedness). Inside the PBG only the allowed circular polarization is emitted. Outside of the PBG, the emission of the other polarization is enhanced and d_e changes rapidly as a function of the wavelength.

4.2.3.5 Electric field profile inside the CLC

In Figure 4.13a the spectrum emitted in the normal direction averaged over the entire cell is compared to that of a dipole in the middle (dashed curve) or at a quarter (dash-dotted curve) of the cell thickness. It is seen that a dipole in the middle of the cell couples strongly to peaks nr. 1 and 3 but only weakly to the 2^{nd} peak. On the other hand a dipole at $z = d_{cell} / 4$ couples strongly to the 2^{nd} peak (and less to peaks 1 and 3).

This position dependent coupling can be understood as follows. The coupling between a dipole antenna and a plane wave depends on the overlap between the local electric field and the dipole moment [15]. Thus a dipole will couple more to modes with a high amplitude at the position of the dipole. In this way the intensity profile of a mode can be estimated by plotting the emitted intensity as a function of dipole position. In Figure 4.13b this simulated emitted intensity is shown as a function of position for peaks nr. 1, 2 and 3 with respective wavelengths $\lambda = 644, 657$ and $673\, nm$.

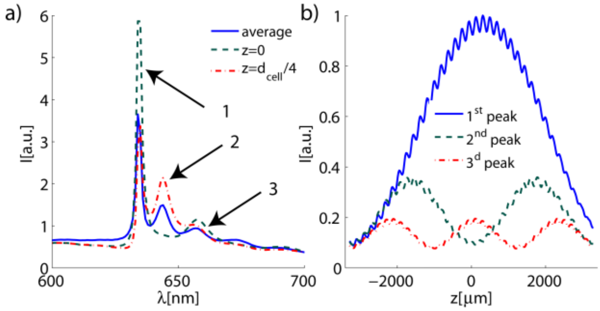

Figure 4.13 a) Simulated emitted spectrum, averaged over the entire cell and from specific positions. The contribution to different modes depends on the position. b) Simulated intensity emitted into peaks nr. 1, 2 and 3 for different positions in the cell. This method can be used to estimate the electric field profile of a resonant mode.

4.2.4 Emission in oblique angles

When a CLC is observed at more oblique angles, the PBG (and the central wavelength λ_c of the PBG) shifts towards shorter wavelengths. This is because the condition that the phase of the electric field changes by π over one period of the CLC, is fulfilled for shorter wavelengths as the inclination angle α_{CLC} in the CLC ($\theta_{CLC} \approx \theta_{glass}$) increases.

$$\frac{2\pi}{\lambda_c}\sqrt{\varepsilon_{avg}}\cos(\theta_{CLC}) = \frac{2\pi}{P} \tag{140}$$

The shift of the PBG to shorter wavelengths is apparent in the emission spectrum of a CLC at higher angles (Figure 4.14a, b, c and d show the emission spectrum at 10°, 20°, 30° and 40° respectively). As the angle increases the PBG and peaks in the emission spectrum shift towards shorter wavelengths. At an angle of 20° the left edge of the PBG is smaller than the excitation wavelength and this emission peak disappears. For even larger angles the entire PBG no longer overlaps with the emission spectrum of the dye and only a small modulation of the intrinsic spectrum (Figure 4.14d) is observed. The shift of the emission spectrum is accurately reproduced by the simulations (red solid curves).

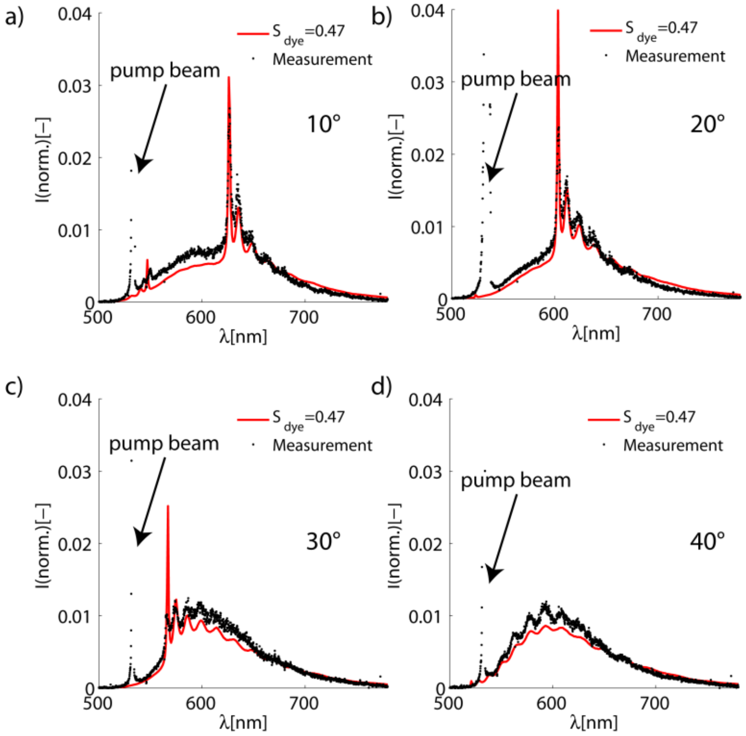

Figure 4.14 Angle dependency of emission spectrum a of CLC cell. Comparison of experiments (dots) and simulation (solid lines). a, b, c and d show measurements at an angle of 10, 20, 30 and 40° in glass respectively.

For large angles (40°) the measured spectrum shows a modulation with the wavelength. This is caused by interference of reflections between the cell edges (CLC/thin ITO/glass interfaces). The period of the fringes is the same in measurement and simulation and is related to the thickness of the CLC layer.

4.3 Stimulated emission in CLCs

In this section stimulated emission from CLCs is discussed. The gain threshold of CLC films with different thickness and pitch is simulated. The simulated threshold is compared to measured values for band-edge CLC lasers. The model described here can be used to estimate the threshold gain of complicated layer structures such as defect mode structures. The model also predicts the wavelength of lasing.

4.3.1 Simulating the gain threshold

Two ingredients are necessary for lasing to occur. First there must be optical gain. Second an optical cavity which confines the light is needed. In its simplest form an optical cavity is formed by two mirrors enclosing a certain volume. When amplification occurs inside an optical cavity light of a resonant wavelength will reflect back and forth in the optical cavity. Meanwhile the intensity is amplified by the optical gain. This process is illustrated in Figure 4.15. When the reflection and gain are sufficiently strong laser radiation will be emitted.

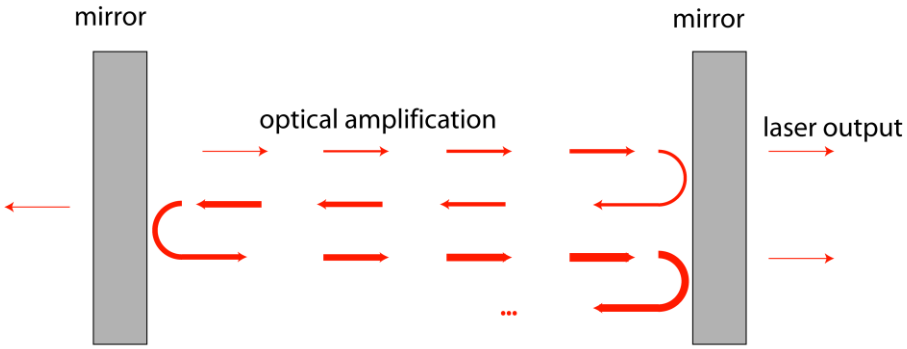

Figure 4.15 Optical amplification and an optical cavity are two necessary ingredients for lasing. As the light travels back and forth in the cavity the beam is amplified. The fraction transmitted by the mirrors is the laser output.

4.3.1.2 Amplification & population inversion

A first necessary ingredient for lasing is optical amplification. Optical gain does not occur for all excited materials. The material must be sufficiently excited to a state called ”population inversion”. When a material is in population inversion an additional emission process is seen: stimulated emission. Stimulated emission amplifies an existing electric field, opposed to spontaneous emission, which emits a field but does not amplify incoming waves.

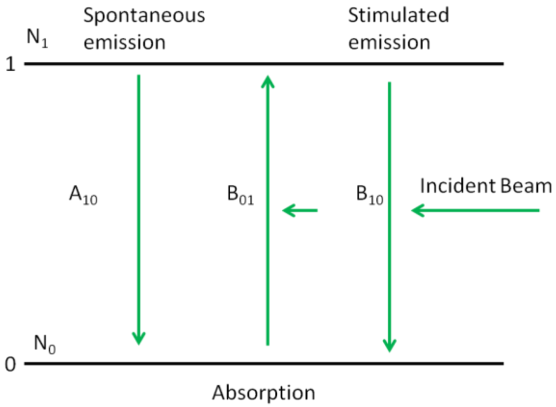

Figure 4.16 Transition mechanisms in a two level system. Molecules can change state by absorption, spontaneous or stimulated emission.

Population inversion and optical gain are determined by the occupation of states and the possible transitions between them in the gain medium. Consider for example the two-level system depicted in Figure 4.16. Transition from the ground state “0” to the excited state “1” can happen by absorption. Transition from the excited state “1” to the ground state “0” can happen via either spontaneous emission or stimulated emission. In this model system only two energy levels are present and the emitted and absorbed wavelengths are identical. In a realistic system the absorbed light has a shorter wavelength than the emitted light. The emission spectrum of spontaneous emission is distributed but stimulated emission is of the same wavelength as the incoming beam. The rate of each transition mechanism to occur is given by[15]:

$$\Gamma_{abs} = B_{01}\frac{I}{c} \tag{141}$$

$$\Gamma_{sp} = A_{10} \tag{142}$$

$$\Gamma_{st} = B_{10}\frac{I}{c} \tag{143}$$

The probabilities for each process are found by multiplying the rate (eq. (141)-(143)) with the population of the initial state. Stimulated emission and absorption are proportional to the intensity of the incident beam. The coefficients A_{10}, B_{10} and B_{01} are known as the Einstein coefficients. It can be proven that $B_{10} = B_{01}$ (if the two levels have the same degeneracy) [15].

In order for optical gain to occur it is necessary that more molecules decay via stimulated emission than are excited via absorption. This can only be the case if more molecules are in the excited state than are in the ground state $N_1 > N_0$. This condition is called "population inversion".

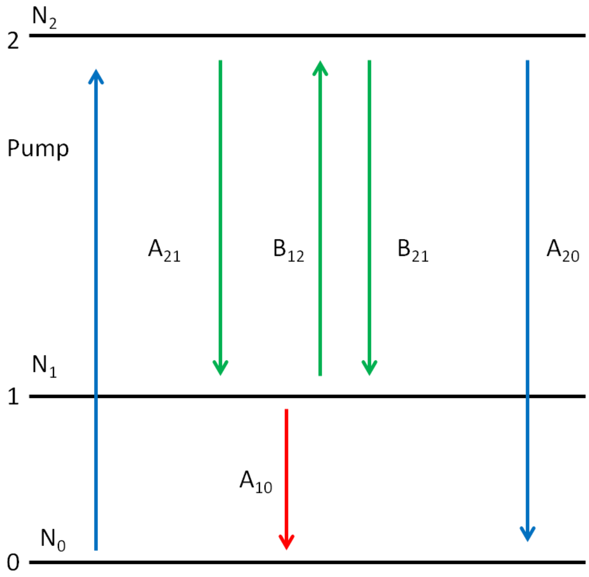

Figure 4.17 Transitions in a three level system. When $N_2 > N_1$, population inversion is achieved. If the decay from "1" to "0" is faster than decay from "2" to "1", population inversion is achieved at much lower pump power.

To achieve population inversion in practice a three (or four) level scheme is often used, like in Figure 4.17. Molecules are pumped from the ground state "0" to the highest excited state "2". The molecules can then decay to the first excited state "1". If the decay from state "1" to the ground state is faster than the decay from state 2 to state 1, population inversion is achieved. The advantage of the three level scheme is that it is much easier to create population inversion, since it is no longer needed to evacuate the ground state.

4.3.1.3 Gain in anisotropic media

The differential equation for the intensity I of a beam propagating (along the z-axis) through a medium with population inversion is given by Eq. 1.9.9 in [15]:

$$\left(1+\frac{I}{I_s}\right)\frac{\partial I}{\partial z}=G(\omega)I \tag{144}$$

Here $G(\omega)$ is the gain coefficient and I_s is the saturation intensity. $G(\omega)$ is proportional to the stimulated emission rate (the Einstein B_{21} coefficient), the normalized line shape $F(\omega)$ of the emitter $(\int F(\omega)d\omega=1)$ and the rate of excitation R from the ground state to the excited state.

$$G(\omega)=M\times R\times F(\omega)\times B_{21} \tag{145}$$

The proportionality factor M depends on the population and on the spontaneous decay rates of the excited states (Eq. (1.9.10) in [15]). When we assume, $I << I_s$. Eq. (144) can be simplified and solved.

$$I(z)=I(0)\exp\left[G(\omega)z\right] \tag{146}$$

Below the saturation regime I increases exponentially as the beam propagates through the gain medium.

In an isotropic medium optical gain can be modelled by adding an imaginary component to the refractive index [76]. Consider a plane wave travelling along the z-axis in a medium with complex refractive index $n+jg$.

$$\mathbf{E}(z)=\mathbf{E}_o\exp(-jk_0(n+jg)z)=\mathbf{E}_o\exp(-jk_0nz)\exp(+k_0gz) \tag{147}$$

If $g>0$ the amplitude of the wave increases with increasing z. This is optical gain. When $g<0$ the wave is attenuated. This corresponds to optical absorption. With $I=\frac{\varepsilon_0 c}{2}|E|^2$, $G(\omega)$ can be related to g [76].

$$g=\frac{G(\omega)\lambda}{4\pi}=\frac{\lambda M}{4\pi}\times R\times F(\omega)\times B_{21} \tag{148}$$

In an anisotropic medium there is a different refractive index n_o and n_e for the ordinary and extra-ordinary polarization. Also the imaginary part of the refractive index g_o and g_e , i.e. the gain and absorption coefficient, will be different for both polarizations.

For stimulated emission a relation between g_o and g_e can be found. The optical gain is a result of decay of excited states by stimulated emission. The decay rate for stimulated emission is given by Fermi’s golden rule. In case of an electrical dipole transition the decay rate is (eq. (80)):

$$\Gamma_{st} = B_{21}\frac{I}{c} = \frac{2\pi}{c\hbar^2}\left|< f\,|\,\mathbf{p}\,|\,s >.\mathbf{E}(k)\right|^2 \rho(k) \tag{149}$$

Γ_{st} is proportional to the square of the electric field. Because of this the stimulated decay rate is proportional to the incident power like in eq. (143). The decay rate also depends on the overlap between the electric field and the transition dipole moment $< f\,|\,\mathbf{p}\,|\,s >.\mathbf{E}$. This means the stimulated emission rate and gain coefficient are highest when the dipole moment and the electric field are parallel. When the dipole moment and the electric field are perpendicular the stimulated emission rate and gain coefficient drop to zero.

We can write the electric field as a sum of two orthogonal polarizations, one perpendicular to the director and one parallel to the director. In a liquid crystal/dye mixture there is a distribution of many dipoles and the stimulated emission rate for the electric field of the emissions parallel/perpendicular to the director will be proportional to the effective fraction of dipoles parallel/perpendicular to the director.

$$B_{21,||}\frac{I_{||}}{c} = \frac{2\pi}{c\hbar^2}\frac{\# p_{||}}{\# p_{||} + 2\# p_{\perp}}\left|< f\,|\,p_{||}\,|\,s > E_{||}\right|^2 \rho(k) \tag{150}$$

$$B_{21,\perp}\frac{I_{\perp}}{c} = \frac{2\pi}{c\hbar^2}\frac{\# p_{\perp}}{\# p_{||} + 2\# p_{\perp}}\left|< f\,|\,p_{\perp}\,|\,s > E_{\perp}\right|^2 \rho(k) \tag{151}$$

An equation for $B_{21,\perp/||}$ is found using $I_{||/\perp} = \frac{\varepsilon_0 c}{2}\left|E_{||/\perp}\right|^2$:

$$B_{21,||} = \frac{4\pi}{\varepsilon_0 c\hbar^2}\frac{\# p_{||}}{\# p_{||} + 2\# p_{\perp}}\left|< f\,|\,p_{||}\,|\,s >\right|^2 \rho(k) \tag{152}$$

$$B_{21,\perp} = \frac{4\pi}{\varepsilon_0 c\hbar^2}\frac{\# p_{||}}{\# p_{||} + 2\# p_{\perp}}\left|< f\,|\,p_{\perp}\,|\,s >\right|^2 \rho(k) \tag{153}$$

An expression for g_o and g_e is found by respectively substituting eq. (153) and (152) in eq.(148). $F(\omega)$ can be written as a function of λ by stating $\int F(\omega)d\omega = \int S_0(\lambda)d\lambda = 1$ and using $\omega = 2\pi c / \lambda$. g_o and g_e are proportional to the fraction of dipoles along the ordinary and extra-ordinary axes.

$$g_o = R' S_0(\lambda) \frac{\lambda^2}{2\pi c} \frac{\# p_\perp}{\# p_{||} + 2\# p_\perp} \tag{154}$$

$$g_e = R' S_0(\lambda) \frac{\lambda^2}{2\pi c} \frac{\# p_{||}}{\# p_{||} + 2\# p_\perp} \tag{155}$$

Where R' (unit s^{-1}) is a factor that depends on the gain material, the absorption of pump power, the transition dipole moment, and the distribution of molecules across the possible states. For modelling of liquid crystal lasers we call R' the pump factor. g_o and g_e can also be written using the order parameter S_{dye} (eq. (138)).

$$g_e = R' S(\lambda) \frac{\lambda^2}{2\pi c} \frac{2S_{dye} + 1}{3} \tag{156}$$

$$g_o = R' S(\lambda) \frac{\lambda^2}{2\pi c} \frac{1 - S_{dye}}{3} \tag{157}$$

Eq. (154) and (155) do not provide an absolute value for g_o and g_e since R' is not known. However to estimate and compare the lasing threshold in different structures it is sufficient to know how g_o and g_e relate to R'. The gain threshold is found at the lowest R' where the condition for lasing is met. This condition is the subject of the next section.

Eq. (149) for the stimulated emission rate is identical to eq. (54) for the spontaneous emission rate. The reason for this is that in quantum-optics spontaneous and stimulated emission are the same process [15]. From this point of view spontaneous emission is stimulated emission by the vacuum field. The vacuum field is the field that exists in the absence of photons and corresponds to the mode density.

4.3.1.4 Round trip gain

Laser action is a result of optical gain and confinement of light in an optical cavity as shown in Figure 4.15. At each mirror a part of the light will be transmitted, this amount of light is “lost”. Losses by absorption or scattering are also possible. As the light travels again through the gain medium the signal is amplified. At the second mirror a certain another fraction of power is lost. The reflected light travels through the cavity and is amplified until it reaches its initial position. This is called a “round trip”. The condition for laser threshold is that all losses (most important is the transmission at the mirrors) during a “round trip” are compensated by gain. In this way the power inside the cavity remains constant even though light is emitted by transmission at the mirrors.

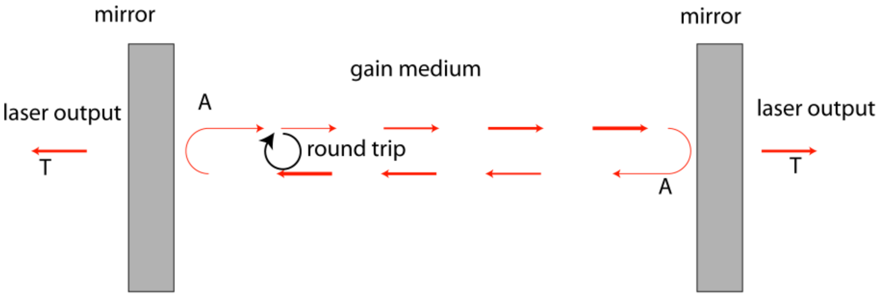

Figure 4.18 Round trip inside a laser cavity. The laser threshold is reached when the gain compensates the losses.

The threshold gain is defined as the smallest g_o or g_e where all losses are compensated by the gain. This is what is meant by stating that for lasing the round trip gain must be larger than 1.

Using this condition the threshold gain can be estimated. The reflection of plane waves in an anisotropic microcavity can be calculated using the method from section 2.4. The round trip gain is found by multiplying the reflection matrices of both sides of the cavity. The effect of gain is included in the reflection matrix $\overline{\overline{A}}^{+/-}$ by the imaginary parts g_o and g_e of the refractive indices. An example of this for a CLC is drawn in Figure 4.19.

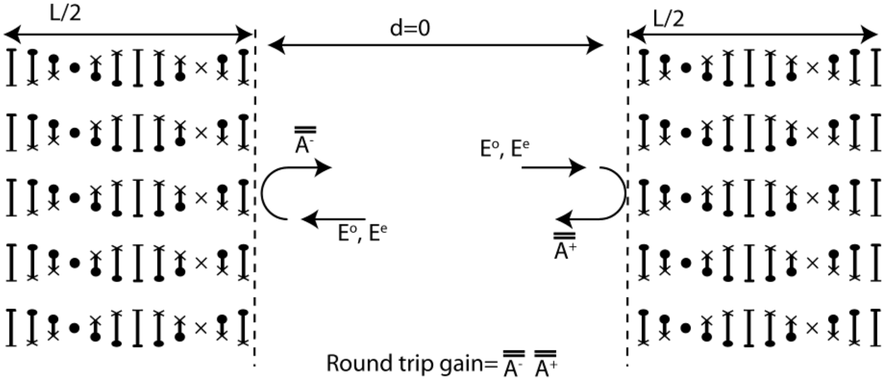

Figure 4.19 Simulation procedure to calculate the threshold gain in a CLC. The CLC film itself supports a resonant standing wave with a maximum in the middle of the film.

Notice that $\overline{\overline{A}}^{+/-}$ are 2x2 matrices containing the complex reflection coefficients of the ordinary and extra-ordinary polarized wave. The matrix product $\overline{\overline{A}}^{-}\,\overline{\overline{A}}^{+}$ is a 2x2 matrix with complex coefficients. For lasing to occur it is sufficient that the round trip gain is larger than 1 for only one polarization state, not for every polarization state. $\overline{\overline{A}}^{-}\,\overline{\overline{A}}^{+}$ can be written as the product of a diagonal matrix and two suitable transformation matrices:

$$\overline{\overline{A}}^{-}\,\overline{\overline{A}}^{+}=\begin{bmatrix} r_{oo} & r_{oe} \\ r_{eo} & r_{ee} \end{bmatrix}=\begin{bmatrix} E_{o,1} & E_{o,2} \\ E_{e,1} & E_{e,2} \end{bmatrix}\begin{bmatrix} \sigma_1 & 0 \\ 0 & \sigma_2 \end{bmatrix}\begin{bmatrix} E_{o,1} & E_{o,2} \\ E_{e,1} & E_{e,2} \end{bmatrix}^{-1} \tag{158}$$

Where $E_{o/e,1/2}$ are the respective ordinary and extra-ordinary component of the two eigenvectors of $\overline{\overline{A}}^{-}\,\overline{\overline{A}}^{+}$, $\sigma_{1/2}$ is the corresponding eigenvalue. All other polarization states can be expressed as a linear combination of the two eigenvectors. For waves polarized according to one of the eigenvectors the effect of a roundtrip is:

$$\overline{\overline{A}}^{-}\,\overline{\overline{A}}^{+}\begin{bmatrix} E_{o,1/2} \\ E_{e,1/2} \end{bmatrix}=\sigma_{1/2}\begin{bmatrix} E_{o,1/2} \\ E_{e,1/2} \end{bmatrix} \tag{159}$$

The eigenvectors are scaled after one round trip. The eigenvalues $\sigma_{1/2}$ describe the change in amplitude and phase and are complex numbers. The condition for lasing can be written as:

$$\sigma_{1/2}=1 \tag{160}$$

4.3.1.5 Algorithm to determine threshold

The gain threshold, lasing wavelength and polarization can now be found by a straightforward procedure.

- Calculate $\sigma_{1/2}$ for all wavelengths of interest
- Check if $\sigma_{1/2} = 1$ for any wavelength
- Increase/reduce the pump factor R'
- Repeat until $\sigma_{1/2} = 1$

When a value of R' is found where $\sigma_{1/2} = 1$ for a certain wavelength, the lasing wavelength is given by that wavelength, the polarization of the laser mode inside the stack is the eigenvector for which $\sigma_{1/2} = 1$. Finally the threshold gain is given by g_o and g_e for that R'.

This procedure is very useful because it allows to estimate the gain threshold, lasing wavelength and polarization in a very simple way. But the model is incapable of calculating other laser characteristics such as the slope efficiency or output power. The limitations of this model become clear when we examine the emission from a dipole in the middle of the cavity given by eq. (62):

$$\begin{bmatrix} E^+_{cav,o} \\ E^+_{cav,e} \end{bmatrix} = \left(1 - \overline{\overline{A^-}}\,\overline{\overline{A^+}}\right)^{-1} \left(\begin{bmatrix} E^+_{\infty,o} \\ E^+_{\infty,e} \end{bmatrix} + \overline{\overline{A^-}} \begin{bmatrix} E^-_{\infty,o} \\ E^-_{\infty,e} \end{bmatrix} \right) \tag{161}$$

When $\sigma_{1/2} = 1$ the denominator $\left(1 - \overline{\overline{A^-}}\,\overline{\overline{A^+}}\right)$ becomes 0 and the field emitted by the dipole would be infinitely large. This is clearly not physical. In reality the rate of stimulated emission will also increase when the electric field becomes larger. As a result the population of the excited states will be reduced and the optical gain will decrease accordingly. Furthermore as the intensity increases the assumption that $I \ll I_S$ made in eq. (146) will no longer be valid and the gain saturation will occur. This process is outside the scope of this simplified model. In equilibrium the amount of molecules excited by the pump is equal to the number decaying back to the ground state by stimulated emission.

4.3.2 Band-edge lasers

In this section we use the model developed in section 4.3.1 to estimate the gain threshold of CLC band-edge lasers. First some general properties of CLC band-edge lasers are given. Then the model is used to predict the influence of pitch, CLC-thickness, dye emission spectrum and orientation of dye molecules on the threshold and lasing wavelength of CLC laser. Finally the simulated threshold and lasing wavelength are compared to experimental data.

4.3.2.1 Properties of band-edge lasers

In Figure 4.20a) the output pulse energy versus input pulse energy of a CLC laser is shown. The curve shows the well known “S-shape” of laser emission. At low input power only fluorescence is observed and little or no emission is detected. As the input power increases the lasing threshold is reached and the output power increases linearly. The slope of the linear increase is called the slope efficiency of the laser. The laser threshold is found by the intersection between the linear input/output relation and the x-axis. At high input power the saturation regime is reached and the output power remains constant.

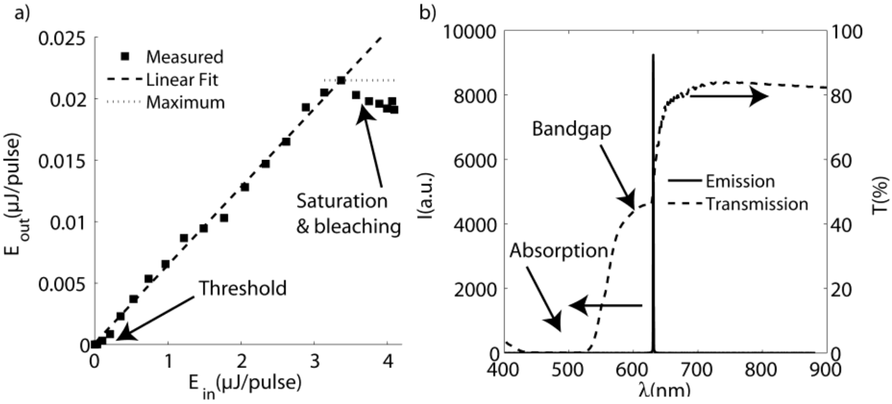

Figure 4.20 a) Output pulse energy vs. input pulse energy for a CLC band-edge laser. The curve shows the classical “S-curve” of a laser. b) emission spectrum of a CLC laser

The spectrum of the laser is shown in Figure 4.20b) together with the spectral transmission of the CLC. The wavelength of the lasing corresponds to one of the edges of the PBG, hence the name band-edge laser. Lasing occurs at the band edge because there the electric field is enhanced by interference inside the CLC as explained in section 4.2.

The emitted laser beam is circularly polarized with the same handedness as the CLC. This is again a logical consequence of the high reflection for this polarization.

4.3.2.2 Threshold of band-edge lasers

A first important parameter of a CLC band-edge laser is the pitch. The pitch determines the width and location of the bandgap. And since lasing occurs at the edges of the band-gap also the lasing wavelength.

Figure 4.21 displays the change in lasing wavelength as a function of the pitch. As expected the lasing wavelength follows the theoretical linear relationship for the band edges $\lambda_{la\sin g} = n_o P$ or $n_e P$. The simulation was performed assuming a CLC with the refractive indices of E7 doped with the laser dye DCM. The CLC thickness was taken to be the number of half pitches closest to 7.13µm . The emission spectrum of DCM in E7 is obtained by measurement (see Figure 4.10). In this simulation $S_{dye} = 0$ is assumed and re-absorption of the emitted light is neglected.

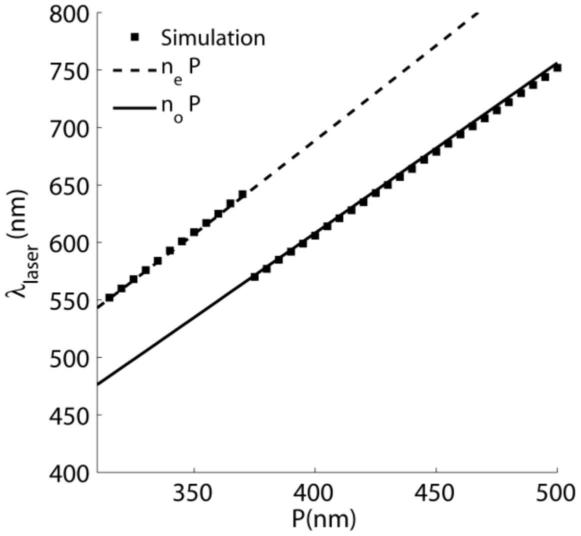

Figure 4.21 Simulated lasing wavelength versus pitch. The simulation matches the theoretical prediction that lasing occurs at the band edges.

At a pitch 375nm the lasing wavelength changes abruptly. This discontinuity marks the transition from lasing on the long wavelength bandedge to lasing on the short wavelength band-edge. The location of the discontinuity depends on the spectrum and order parameter of the dye as well as the CLC thickness.

In Figure 4.22 the pump factor R' at threshold is plotted as a function of the pitch (a) and the lasing wavelength (b). Figure 4.22 a) shows two local minima for the threshold gain around $P = 350$ and $P = 405$ nm. The local maximum in between is situated at $P = 375$ nm. This maximum coincides with the change of the lasing wavelength from the right bandedge to the left band edge (see Figure 4.21). The two valleys in Figure 4.22a describe the threshold of lasing on the right ($P < 375$ nm) and the left ($P > 375$ nm) edge of the bandgap.

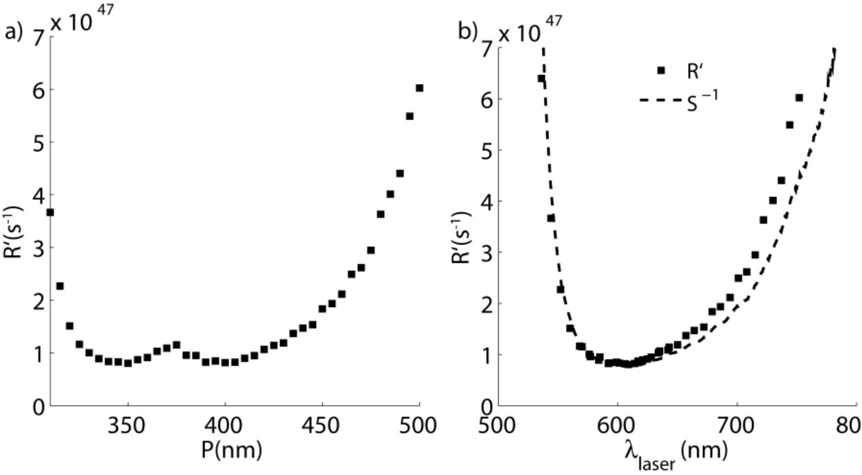

Figure 4.22 a) Threshold pump factor R' vs. pitch b) Pump factor R' vs. lasing wavelength (squares) and inverse of the emission spectrum of the laser dye(dashed line). The dashed curve has been rescaled in order to show the similar shapes of the two curves.

The threshold gain is compared to the emission spectrum of the dye in Figure 4.22b). It can be seen that the curve for the threshold gain has a shape similar to $1/S_0(\lambda)$. This means that the lasing threshold is lowest when one of the band-edges is matched to the maximum of the $S_0(\lambda)$.

The $1/S_0(\lambda)$ shape of the threshold curve can be understood by an intuitive calculation. The condition for lasing is that the round trip gain equals 1. The round trip gain is given by Eq. (159). In this intuitive argument we assume that the reflections are in-phase ($\arg(\sigma_{1/2})=0$), which holds for the resonant wavelengths. Then $\sigma_{1/2}$ can be written as:

$$\sigma_{1/2}=|A|\exp(R'S_0(\lambda)) \tag{162}$$

$\sigma_{1/2}$ is the product of the gain in the cavity $\exp(RS_0(\lambda))$ and a factor $|A|<1$ caused by the reflections in the cavity. We can then solve $\sigma_{1/2}=1$ for R':

$$R'=-\frac{\ln|A|}{S_0(\lambda)} \tag{163}$$

In reality g_o and g_e also influence the reflections of the cavity, but this effect is small and neglecting this provides some understanding about the relation between threshold and wavelength.

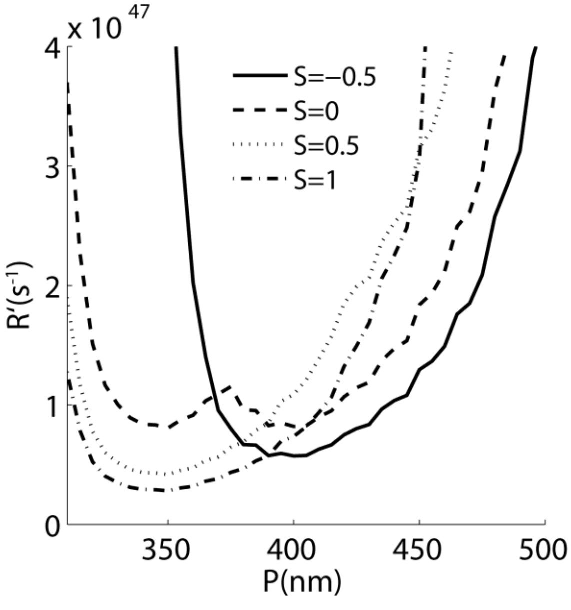

Figure 4.23 Threshold gain vs. pitch for different order parameters. Dye orientation varies from completely perpendicular to the LC (solid curve) to completely parallel (dash-dotted curve).

Figure 4.23 shows the effect of the order parameter S_{dye} on the gain threshold for various pitches. For a completely perpendicular oriented dye, the (solid) curve only shows one minimum around $P=400nm$. This corresponds to lasing at the left bandedge. Recall that also the spontaneous emission of a perpendicular dipole favours the left side of the bandgap

(Figure 4.11a). A completely parallel oriented dipole (dash-dotted curve) also yields a single minimum but for smaller $P = 350\,\text{nm}$, corresponding to lasing at the right bandedge. The spontaneous emission of a parallel dipole also prefers the right bandedge (Figure 4.11a).

The threshold for a randomly oriented dye (dashed curve) shows two minima. These minima correspond to lasing from the right or left bandedge as was discussed above. The spontaneous emission from a randomly oriented dipole indeed excites resonant wavelengths at both sides of the bandgap.

4.3.2.3 Comparison with experiment

In the previous section a model for the gain threshold of a CLC laser has been derived. In this section the results of the simulation model are compared to the empirically measured thresholds of band-edge CLC lasers with various pitch and thickness.

The absorption and emission spectrum of the liquid crystal dye mixture overlap for some wavelengths. For those wavelengths a part of the emitted light will be re-absorbed as the light propagates through the CLC-film. The absorption can be treated in simulation by adding imaginary absorption terms α_o and α_e to the refractive indices n_o and n_e. α_o and α_e can be determined from a measurement of the transmission in a planar aligned nematic liquid crystal cell of known thickness. The effect of reduced absorption due to the population inversion is neglected here.

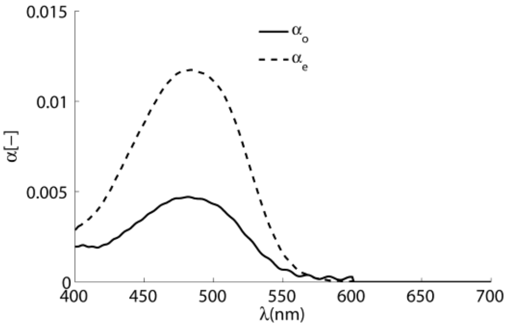

Figure 4.24 : Absorption terms α_o and α_e vs. λ determined from the transmission spectra of a nematic DCM/E7 mixture.

A series of liquid crystals cells were made filled with a CLC mixture doped with the laser dye DCM. The mixing and fabrication is explained in section 4.2.3.1. The composition of the mixtures is given in Table 4.

Table 4 Composition of laser dye/ chiral dopant/ liquid crystal mixtures. The concentration of chiral dopant BDH1305 determines the pitch. The more dopant the shorter the pitch.

Mixture	*DCM (weight %)*	*BDH1305(weight%)*	*E7(weight%)*
1	1.28	5.33	93.39
2	1.54	5.16	93.30
3	0.90	4.65	94.45
4	0.90	4.30	94.81
5	1.27	4.42	94.31
6	0.90	4.58	94.52

Laser emission was achieved in a total of 14 cells. Two cell thicknesses were targeted in fabrication, $15\mu m$ and $20\mu m$. The actual thickness of each cell varies due to fabrication uncertainties. The cell thicknesses are individually determined by the Fabry-Perot fringes of the transmission spectrum prior to filling the cell. The resulting average thicknesses (respectively for target thickness $15\mu m$ and $20\mu m$) are $15.5\mu m$ and $20.5\mu m$ with a standard deviation of $1.4\mu m$ and $1.9\mu m$ respectively. The cells were filled with the CLC mixtures. An overview of the different cell thicknesses and the CLC filling mixture is given in Table 5.

Table 5 CLC mixture and measured thickness of different cells

Sample ID	*Mixture*	*Thickness(μm)*	*Category*
C1	1	20.48	20μm
C2	2	20.56	20μm
C3	3	20.48	20μm
C4	4	20.58	20μm
C5	5	20.55	20μm
C6	6	20.55	20μm
E3	3	25.65	20μm
E4	4	21.14	20μm
D2	2	18.39	15μm
D1	1	12.53	15μm
D3	3	13.45	15μm
D4	4	14.71	15μm
E1	1	16.22	15μm
E2	2	14.81	15μm

For the simulation the boundary condition that the CLC can only be a discrete number of half pitches thick (imposed by the parallel rubbed alignment layers) is taken into account by choosing the CLC thickness as the number of half pitches closest to the measured average thickness (respectively 15.5 and 20.5µm).

The lasing threshold and wavelength is measured using the setup depicted in Figure 4.25. The sample is excited by a pulsed green laser ($\lambda_{pump} = 532nm$). The polarized laser pulses are sent through a half-wave plate and a polarizing beam splitter. The halfwave plate is rotated to control the power of the beam sent to the sample. Additional control of the input power is provided by two neutral density filters with a transmittance of 11.4% each at $532nm$. By placing one or both of these filters the input power can be further reduced. The pump beam is then sent through a quarter wave plate to obtain circular polarization and focussed onto the sample by a lens. The pump beam reaches the sample at angle of $45°$.

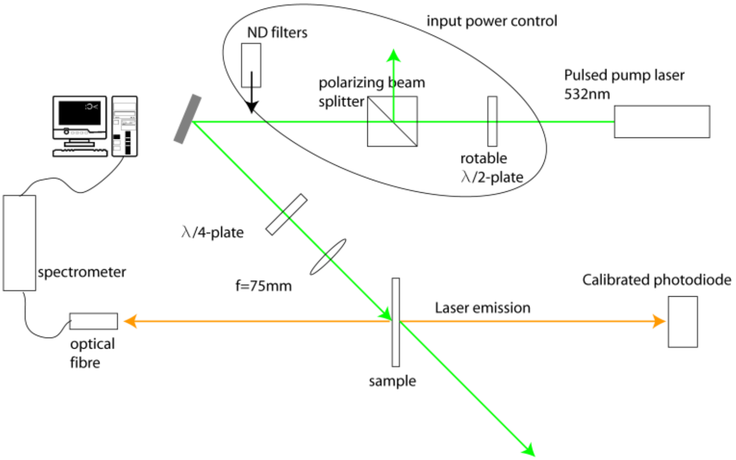

Figure 4.25 Setup for measuring laser threshold and wavelength.

When the input power is above the lasing threshold, the CLC cell emits two laser beams perpendicular to its surface into both directions. On one side the power of the emitted beam is measured by a calibrated photodiode. On the other side the light is collected by an optical fibre connected to a spectrometer. In this way the output power and spectrum can be measured simultaneously. The photodiode does not measure the total emitted power since not all emitted light is incident on the photodiode surface. The power measurement is intended to determine the lasing characteristics, mainly the threshold, not to provide an absolute value for the total emitted power.

An example of the output pulse energy vs. input pulse energy measurement is shown in Figure 4.20a). The typical laser characteristics of threshold, a linear increase above threshold and finally a saturation of the output pulse energy are seen. From these measurements the threshold can be determined by fitting a curve $E_{out} = aE_{in} + b$ to the linear increase region of the output vs. input pulse energy graph (from $E_{in} = 0.005 \mu J / pulse$ to $E_{in} = 2.50 \mu J / pulse$ in Figure 4.20a). The threshold is the intercept between the x-axis and the fitted curve.

$$E_{threshold} = \frac{-b}{a} \tag{164}$$

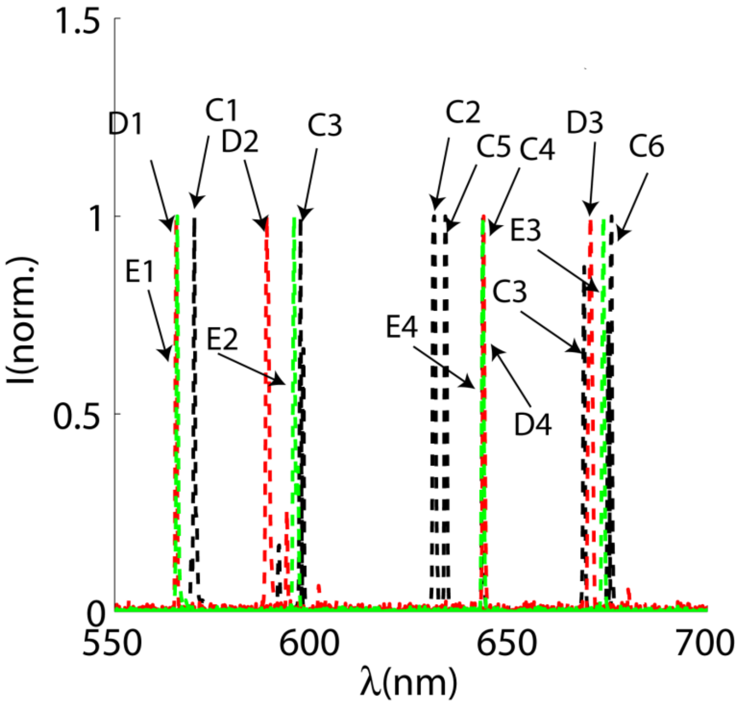

Figure 4.26 Normalized spectrum of CLC laser samples above threshold. Samples with the same BDH1305 concentration have similar pitches and emit around the same wavelength.

The laser spectrum of these samples is shown in Figure 4.26. All samples were measured above threshold. CLC samples with the same chiral dopant concentration (e.g. C4, D4 and E4) have nearly the same pitch and emit at the same wavelength. Some samples (C3) emit from both the left and right edge of the bandgap.

Using $\lambda_{laser} = n_{o/e}P$, P can be derived from the measured lasing wavelength. P is roughly inversely proportional to the concentration of chiral dopant, with a proportionality factor called the helical twisting power $|HTP|$ [77].

$$P = \frac{1}{|HTP| c_{BDH1305}} \tag{165}$$

The pitches estimated from the lasing wavelength follow this relationship (see Figure 4.27). The resulting helical twisting power $|HTP| = 0.55 \mu m^{-1} \%^{-1}$ is found for BDH1305 in E7.

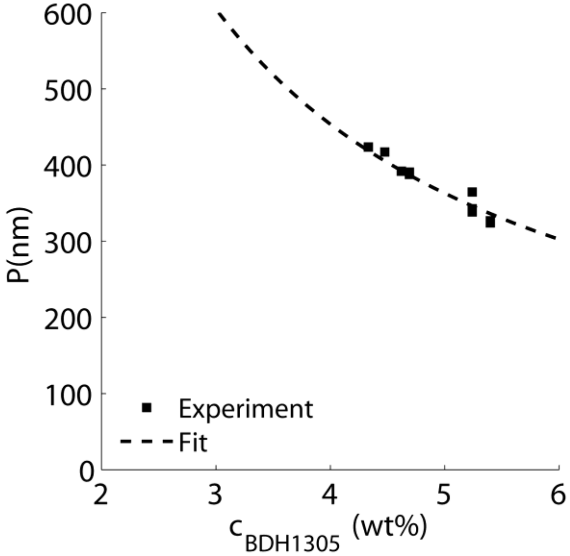

Figure 4.27 Helical pitch as a function of chiral dopant concentration and fit with the inverse proportionality.

The simulated and measured thresholds for different thicknesses and pitches are compared in Figure 4.28. The simulated and measured thresholds are shown in function of P for cells of 15 and 20µm. Note that there is some variation in the thickness of the measured cells. However no correlation was found between the deviation between the average and measured thickness and the deviation between the simulated and measured threshold.

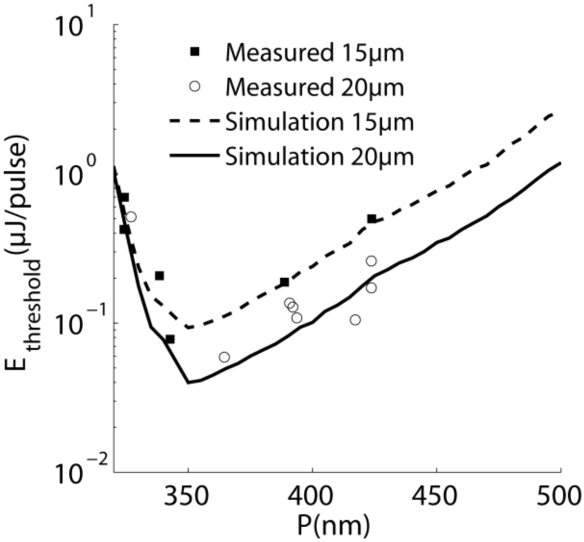

Figure 4.28 Comparison of simulated and measured lasing threshold vs. pitch. Threshold is lowest for a thick cell with the right bandedge matched to the emission spectrum of the laser dye. Simulation and experiment show the same threshold vs. pitch and thickness behaviour.

The simulations predict the lowest threshold for $P = 350\,\text{nm}$ both for $15\,\mu m$ (dashed curve) and $20\ \mu m$ (solid curve) thick cells. This corresponds to the long wavelength band edge matched to the maximum of $S_0(\lambda)$ (see 4.3.2.2). The measured thresholds follow the same trend as the simulations both for $15\,\mu m$ (squares) and $20\,\mu m$ (circles). On average the simulation gives a reliable estimation of which design will give the lowest threshold.

Some discrepancy exists between the measured and simulated threshold, being most pronounced for the 20μm cells. The discrepancy can be caused by several reasons. First there is some variation in the thickness of the measured CLC cells. Second the presence of domain boundaries in the sample can cause additional scattering losses increasing the threshold. As cells become thicker it is more difficult to achieve a mono-domain cell (with no domain boundaries). During fabrication the cells were slowly cooled to room temperature to reduce the number of domains but formation of domains could not be completely avoided. This may be the reason that $20\,\mu m$ cells show different thresholds even for similar P. Third there can be a difference in the absorption of the pump beam for different pitches or more light may be absorbed at the side where the pump beam enters the cell, leading to a non-uniform gain across the cell. In simulation a mono-domain sample and uniform pumping is assumed.

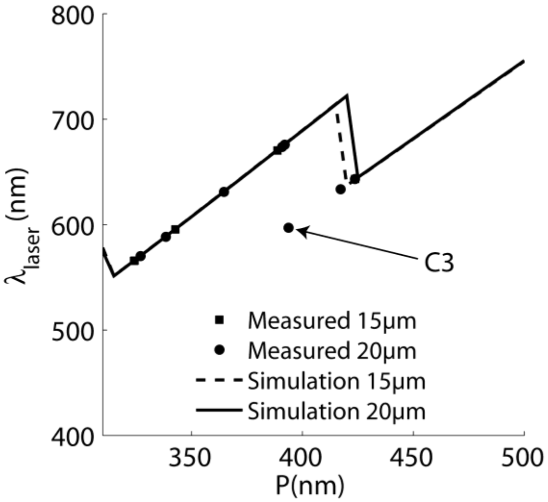

Figure 4.29 Simulated and measured lasing wavelength vs. pitch

Finally the measured and simulated lasing wavelength can be compared (Figure 4.29). Simulation and measurement are in agreement except for the point C3 which emits at right edge of the band gap instead of the expected emission at the left side. The jump occurs for slightly shorter pitches in the experiment than in theory. On a closer look to the lasing spectrum of C3 (Figure 4.26) it is seen that C3 shows laser emission from both band edges of nearly equal intensity (ratio 0.87).

4.4 Conclusion

Cholesteric or chiral nematic liquid crystals are attracting a lot of research interest because they spontaneously form a photonic bandgap. One of the most interesting applications of cholesteric liquid crystals is the liquid crystal laser. Such a self-assembling laser is easy to produce and offers small size lasers that are tuneable over a broad range.

In this chapter light emission from cholesteric liquid crystals has been studied using the plane wave expansion approach. The photonic bandgap of the CLC has a strong influence on the spontaneous emission from inside the CLC. The PBG prevents the emission of waves with wavelength and polarization inside the PBG. At the edges of the PBG the spontaneous emission is enhanced. The fluorescence from a CLC can be modelled by treating the CLC as an ensemble of incoherent dipole antennas inside a stack of thin anisotropic films with periodically varying orientation of the optical axis.

Dipoles with different orientations inside the CLC couple to different wavelengths. A dipole perpendicular to the LC will couple to the wavelengths at the left side of the PBG, dipoles parallel to the LC mainly emit on the right side of the PBG. The measured spectrum, polarization and angular variation of the spontaneous emission are well reproduced by the plane wave simulation.

The plane wave approach can be used to model stimulated emission and lasing in CLCs. Optical gain is treated as an imaginary part of the ordinary and extra-ordinary refractive index. The ratio between the imaginary parts depends on the orientation of the dye molecules. The threshold for lasing is reached when the optical gain compensates for the losses inside the cavity.

When a CLC is sufficiently pumped it will emit a laser beam with wavelength at one of the band edges. The threshold of this beam is determined by the matching of the band edge to the dye spectrum, the cavity losses, and the dipole orientation. Measurements and simulation of the laser threshold are in agreement. The plane wave model for lasing can be used as a tool to design liquid crystal lasers with a lower threshold.

5. Conclusions & Outlook

In this concluding chapter the main results of this thesis and the research leading up to it are summarized. After that some suggestions for future development are given for all three subjects: plane wave expansion modelling, OLEDs and CLC photonic devices.

5.1 Conclusions

The topic of this thesis is the optical modelling of light emitting devices. In a constant search for highly performant, energy-efficient light sources optical modelling is a very important tool to develop and optimize new technologies. In this work the plane wave expansion method is developed for uniaxial anisotropic media and used to model two promising new devices: organic light emitting diodes and self assembling cholesteric liquid crystal lasers

5.1.1 Plane wave methods

The basics of the plane wave expansion method have been introduced in chapter 2. Plane wave modelling of isotropic stacks of thin films was developed in the 80's by Lukosz and is now widely used. In this work the PWE method was expanded to uniaxially anisotropic thin film devices. Plane wave modelling is based on the principle that a complicated electric field can be treated as a sum of plane waves. The behaviour of each plane wave is then calculated separately. In this way the modelling of the full electric field in a complicated device is simplified to calculating the response of the device to individual plane waves. Many devices are made by thin film techniques producing a series of uniform layers on top of each other. The reflection and transmission of plane waves in one-dimensional stacks can be calculated quickly. The plane wave method is thus ideal for optimization of thin film devices.

Light emission is the result of the decay of a molecule from an excited state to the ground state. Usually this happens via an electric dipole transition. The emission averaged over a large amount of photons is equal to the emission of a classical dipole antenna. The first step in the modelling is to decompose the electric field of a dipole antenna in a uniaxial medium as a sum of plane waves. This decomposition is obtained by rewriting and solving Maxwells equations for scalar Hertz potentials.

The second step in modelling the light emission is to calculate the effect of the optical environment on the electric field of the dipole. For this the reflection and transmission by the layers making up the microcavity have to be calculated. For anisotropic media this can be done using the scattering matrix approach (in this work) or the Berreman 4x4 matrix method. The effect of the optical microcavity on the radiative decay rate of excited molecules is modelled by calculating the total power radiated by the dipole antenna.

5.1.2 Organic LEDs

In chapter 3 light emission from organic LEDs has been investigated. OLEDs function in a way similar to standard inorganic LEDs, but are made with organic semiconductor materials. OLEDs are being intensely studied for high quality displays and lighting. OLED displays are already commercially available in smart phones and even large area televisions (55 inch) have been announced by two companies. OLED lighting has also been introduced in high-end design lamps.

Four factors determine the efficiency of OLEDs. The charge balance, an electrical parameter which determines how much of the current is transformed into excitons. The singlet/triplet ratio expresses which fraction of the excited states can decay radiatively. The radiative decay efficiency determines how many of the excitons actually decay radiatively. Finally the outcoupling efficiency expresses how much of the emitted light escapes the device. Both radiative decay efficiency and outcoupling efficiency are influenced by the optical design of the OLED.

The outcoupling of OLEDs is limited by the high refractive index (1.8) of the organic layers in which the light is generated. Only light emitted into an escape cone is able to escape the device, all other light remains trapped. To improve the outcoupling efficiency the emission of the dipoles must be directed into the escape cone as much as possible. Furthermore the trapped light can be scattered into the escape cone. Both a favourable radiation pattern and scattering of trapped light must be combined to achieve optimal outcoupling.

Interference effects inside the organic layer stack have a large influence on the angular distribution of radiation. Most important is the distance to the metal cathode, because this distance determines if the radiation in the forward direction is enhanced or reduced.

Another important effect of the cathode is the excitation of plasmon waves and absorption of the near-field of the dipole antenna. Both near field absorption and excitation of plasmon waves are loss channels in a planar OLED. Both processes should be taken into account in the OLED optimization. Analytical formulas to estimate the effect of both mechanisms have been derived.

The radiation pattern inside the OLED may be further improved by the use of oriented dipole emitters. A dipole oriented parallel to the organic layers radiates up to 50% more light into the escape cone than a randomly oriented dipole. In this work it has been shown that the orientation of dipoles inside organic devices can be determined by measuring the decay time of phosphorescent emitters in a series of organic devices. This outcoupling technique requires no additional structuring and would be suited for both display and lighting applications.

5.1.3 Cholesteric liquid crystals

Another promising type of devices is based on cholesteric liquid crystals. Cholesteric liquid crystals are liquid crystals with a director which rotates in a screw-like manner. When the rotation pitch is of the same size as a wavelength, the CLC becomes highly reflective for circularly polarized light of the same helicity. In this way a CLC is an optical component with periodicity determined by self-organization.

By doping a CLC with a laser dye, the CLC emits a laser beam when sufficiently pumped. This type of laser is tuneable over a broad range in the visible and near-infrared region. CLC-lasers are very cheap to produce. Currently an external pulsed laser is required to pump the CLC-laser. An important challenge is to reduce the threshold to enable pumping with more affordable sources.

The spontaneous emission of dye molecules inside a CLC is significantly different from that in an ordinary medium. Inside the bandgap emission is prohibited, emission at the band edges is enhanced. The light emission from a CLC is accurately modelled using the plane wave model. An important parameter is the orientation of the dipole moment. A dipole will couple most strongly to modes for which the electric field is parallel to the dipole. The experimental spectrum, polarization and angular variation of the emission are all reproduced by plane wave simulations.

The lasing threshold, wavelength and polarization of a CLC laser have been modelled by introducing a gain term to the refractive indices. By increasing the gain until it compensates for the transmission losses the gain threshold can be simulated. The gain threshold is influenced by several factors: the dye spectrum, dipole orientation, pitch and CLC thickness. The simulated threshold values have been verified experimentally with a series of CLC lasers of various pitch and thickness. The simulation model provides a reliable indication for the lasing threshold. This model can be used as a tool to design new liquid crystal laser architectures with reduced threshold.

5.2 Future work

During my thesis I have developed models for thin film light emitting devices. These models have been verified experimentally and proved accurate. A next important step is to use these models to design improved OLEDs, liquid crystal lasers and many other components. In this section a few suggestions for future work are given for expanding the current model, optimizing OLEDs and CLCs and apply this model to other research fields.

The plane wave expansion for dipoles in anisotropic cavities explained in chapter 2 is given for uniaxially anisotropic materials. Another step in the development would be to expand it to biaxial media. For this both the reflection and the transmission calculation need to account for biaxial materials and the dipole field expansion must be made for a biaxial medium. The reflection of biaxial materials can be calculated using the Berreman 4x4 method or by an adapted version of the scattering matrix formalism in chapter 2. The largest challenge lies in solving Maxwells equations for a dipole in a biaxial medium for all orientations of the dipole and the materials principal axes.

The current plane wave model assumes that the device consists of a stack of thin large area layers. The range of application of the model could be greatly enlarged by incorporating the simulation of structured layers like diffraction gratings. Nearly any 3D structure can be simulated as a periodic structure with appropriate boundary conditions[78]. Especially the combination of periodic structures and anisotropy[79] would allow the simulation of configurations that are not easy to simulate by other means.

In chapter 3 the high outcoupling of oriented dipoles in OLEDs has been demonstrated. We (and other authors) have also demonstrated oriented emitters in some materials. A remaining challenge is to implement oriented emitters in OLED devices to achieve high outcoupling. This is not a trivial task since to achieve optimal OLED performance many requirements have to be fulfilled. Ideally the emitter should also have long lifetime, phosphorescent decay and there should be emitters for all colours (red, green and blue) and mainly horizontal orientation. In addition to the dye an appropriate organic host material must also be available with desired bandgap, good electrical properties and long lifetime...

The outcoupling can be increased in many ways: by internal and external scattering and orientation. For the best outcoupling performance an optimal combination of all these techniques must be used. Modelling the combined effects of multiple outcoupling mechanisms can yield the best possible outcoupling for high efficiency OLEDs.

The major challenges for CLC lasers are to achieve high power output and low threshold. Reminiscent of the development of DFB lasers (which show many similarities with CLC lasers) the threshold can be reduced using different layer structures like a defect-mode structure or combining LC layers with other optical structures like Bragg mirrors. The plane wave modelling can be used to design and optimize such structures for low threshold lasing.

Another area for development is the expansion of the laser modelling capabilities. By coupling the gain factor of the refractive index to the population of the excited and ground states of the laser dye it may be possible to model the output power, slope efficiency, saturation, and pulse shape of CLC lasers. This is currently outside of the possibilities of the plane wave model. This expansion of the model however does require assumptions or measurement of the properties of the laser dye and the decay from all states[80].

Finally the plane wave model can also be used to explore the effects of anisotropy in other technologies than OLEDs and CLCs. For example plasmonics is currently a hot topic in photonics research where the optical effects of liquid crystal/metal interfaces are studied. Other possible areas are luminescent solar concentrators, organic light emitting field effect transistors and organic laser diodes.

Appendix A

Detailed calculation of the dipole field in a uniaxial medium

In chapter 2 the radiation of a dipole in an anisotropic layer stack has been derived. For clarity only important intermediate results are shown in chapter 2. The details of the calculation are given in this appendix. The calculation involves five basic steps: writing Maxwells equation for scalar Hertz potentials, obtaining uncoupled differential equations, solving the uncoupled differential equations via the fourier domain, inserting the source terms for an elementary dipole and returning to the *xyz* system with an inverse fourier transform.

Maxwell's equation with scalar Hertz potentials

We will solve Maxwells equations following the approach given in [14]. Maxwell's equations are shown below.

$$\nabla.(\overset{=}{\varepsilon}\mathbf{E}) = \rho \qquad (166)$$

$$\nabla \times \mathbf{E} = -\frac{\partial(\mu \mathbf{H})}{\partial t} \tag{167}$$

$$\nabla.(\mu \mathbf{H}) = 0 \tag{168}$$

$$\nabla \times \mathbf{H} = \frac{\partial(\overline{\overline{\varepsilon}} \mathbf{E})}{\partial t} + \mathbf{J} \tag{169}$$

We split all vector quantities ($\mathbf{E}$, $\mathbf{H}$, $\mathbf{J}$ and ∇) in their components parallel and perpendicular to $\mathbf{c}$.

$$\mathbf{E} = \mathbf{E}_\perp + E_{||}\mathbf{c} \tag{170}$$

$$\mathbf{H} = \mathbf{H}_\perp + H_{||}\mathbf{c} \tag{171}$$

$$\mathbf{J} = \mathbf{J}_\perp + J_{||}\mathbf{c} \tag{172}$$

$$\nabla = \nabla_\perp + \frac{\partial}{\partial c}\mathbf{c} \tag{173}$$

Eq. (167) and (169) are then rewritten as:

$$(\nabla_\perp + \frac{\partial}{\partial c}\mathbf{c}) \times (\mathbf{H}_\perp + H_{||}\mathbf{c}) = \frac{\partial \overline{\overline{\varepsilon}}(\mathbf{E}_\perp + E_{||}\mathbf{c})}{\partial t} + \mathbf{J}_\perp + J_{||}\mathbf{c} \tag{174}$$

$$\left(\nabla_\perp + \frac{\partial}{\partial c}\mathbf{c}\right) \times (\mathbf{E}_\perp + E_{||}\mathbf{c}) = -\mu \frac{\partial(\mathbf{H}_\perp + H_{||}\mathbf{c})}{\partial t} \tag{175}$$

The dielectric tensor is diagonal in this coordinate system. And eq. (174) becomes

$$(\nabla_\perp + \frac{\partial}{\partial c}\mathbf{c}) \times (\mathbf{H}_\perp + H_{||}\mathbf{c}) = \frac{\partial(\varepsilon_\perp \mathbf{E}_\perp + \varepsilon_{||} E_{||}\mathbf{c})}{\partial t} + \mathbf{J}_\perp + J_{||}\mathbf{c} \tag{176}$$

We take the scalar product both of eq.(176) and (175) with $\mathbf{c}$. Taking into account that for any vector $\mathbf{V}$: $\mathbf{c} \cdot \left(\frac{\partial}{\partial c}\mathbf{c} \times \mathbf{V}_\perp \right) = 0$, $\mathbf{c} \cdot \left(\nabla_\perp \times V_{||}\mathbf{c} \right) = 0$, $(\frac{\partial}{\partial c}\mathbf{c}) \times (V_{||}\mathbf{c}) = 0$ and $\mathbf{c} \cdot \mathbf{V}_\perp = 0$ and that $\nabla_\perp \times \mathbf{V}_\perp$ is parallel to $\mathbf{c}$ we obtain:

$$\nabla_\perp \times \mathbf{H}_\perp = \frac{\partial \varepsilon_{||} E_{||}}{\partial t} + J_{||} \tag{177}$$

$$\nabla_\perp \times \mathbf{E}_\perp = -\mu \frac{\partial H_{||}}{\partial t} \tag{178}$$

Two additional equations can be obtained by taking the vector product of eq. (176) and (175) with $\mathbf{c}$. Where we use $\mathbf{c}\times(\nabla_\perp\times\mathbf{V}_\perp)=0$, $\mathbf{c}\times(\frac{\partial}{\partial c}\mathbf{c}\times V_\parallel\mathbf{c})=0$ and $\mathbf{c}\times V_\parallel\mathbf{c}=0$ and also the identities $\mathbf{c}\times(\nabla_\perp\times V_\parallel\mathbf{c})=\nabla_\perp V_\parallel$ and $\mathbf{c}\times(\frac{\partial}{\partial c}\mathbf{c}\times\mathbf{V}_\perp)=-\frac{\partial\mathbf{V}_\perp}{\partial c}$.

$$\nabla_\perp H_\parallel-\frac{\partial\mathbf{H}_\perp}{\partial c}=\mathbf{c}\times\left(\frac{\partial\varepsilon_\perp\mathbf{E}_\perp}{\partial t}+\mathbf{J}_\perp\right)\tag{179}$$

$$\nabla_\perp E_\parallel-\frac{\partial\mathbf{E}_\perp}{\partial c}=-\mu\mathbf{c}\times\frac{\partial\mathbf{H}_\perp}{\partial t}\tag{180}$$

Finally we also take the vector product of eq. (179) and (180) with $\mathbf{c}$.

$$\mathbf{c}\times\nabla_\perp H_\parallel-\frac{\partial\left(\mathbf{c}\times\mathbf{H}_\perp\right)}{\partial c}=-\frac{\partial\varepsilon_\perp\mathbf{E}_\perp}{\partial t}-\mathbf{J}_\perp\tag{181}$$

$$\mathbf{c}\times\nabla_\perp E_\parallel-\frac{\partial\left(\mathbf{c}\times\mathbf{E}_\perp\right)}{\partial c}=+\mu\frac{\partial\mathbf{H}_\perp}{\partial t}\tag{182}$$

The perpendicular fields $\mathbf{E}_\perp$ and $\mathbf{H}_\perp$ are now written as gradients of the scalar Hertz potentials Φ, Θ, Π and Ψ:

$$\mathbf{E}_\perp=\nabla_\perp\Phi+\nabla_\perp\times(\Theta\mathbf{c})\tag{183}$$

$$\mathbf{H}_\perp=\nabla_\perp\Pi+\nabla_\perp\times(\Psi\mathbf{c})\tag{184}$$

and substituted in the six equations (177)-(182). Taking in mind that: $\nabla_\perp\times\nabla_\perp V=0$ and $\nabla_\perp\times(\nabla_\perp\times V\mathbf{c})=-\nabla_\perp^2 V\mathbf{c}$, eq. (177)-(182) can be rewritten as:

$$-\nabla_\perp^2\Psi=\frac{\partial\varepsilon_\parallel E_\parallel}{\partial t}+J_\parallel\tag{185}$$

$$\nabla_\perp^2\Theta=\mu\frac{\partial H_\parallel}{\partial t}\tag{186}$$

$$\nabla_\perp H_\parallel-\frac{\partial\nabla_\perp\Pi}{\partial c}-\frac{\partial\left[\nabla_\perp\times(\Psi\mathbf{c})\right]}{\partial c}=\mathbf{c}\times\left\{\varepsilon_\perp\frac{\partial\left[\nabla_\perp\Phi+\nabla_\perp\times(\Theta\mathbf{c})\right]}{\partial t}+\mathbf{J}_\perp\right\}\tag{187}$$

$$\nabla_\perp E_\parallel-\frac{\partial\nabla_\perp\Phi}{\partial c}-\frac{\partial\left[\nabla_\perp\times(\Theta\mathbf{c})\right]}{\partial c}=\mathbf{c}\times-\mu\frac{\partial\left[\nabla_\perp\Pi+\nabla_\perp\times(\Psi\mathbf{c})\right]}{\partial t}\tag{188}$$

$$(\mathbf{c}\times\nabla_\perp H_\parallel)-\frac{\partial\left\{\mathbf{c}\times\left[\nabla_\perp\Pi+\nabla_\perp\times(\Psi\mathbf{c})\right]\right\}}{\partial c}=-\varepsilon_\perp\frac{\partial\left[\nabla_\perp\Phi+\nabla_\perp\times(\Theta\mathbf{c})\right]}{\partial t}-\mathbf{J}_\perp\tag{189}$$

$$(\mathbf{c}\times\nabla_{\perp}E_{\parallel})-\frac{\partial\left\{\mathbf{c}\times\left[\nabla_{\perp}\Phi+\nabla_{\perp}\times(\Theta\mathbf{c})\right]\right\}}{\partial c}=+\mu\frac{\partial\left[\nabla_{\perp}\Pi+\nabla_{\perp}\times(\Psi\mathbf{c})\right]}{\partial t} \tag{190}$$

In this way we have found 6 differential equations for 6 variables $E_{\parallel}$, $H_{\parallel}$, Φ, Θ, Π and Ψ.

Obtaining uncoupled differential equations

The next step of the calculation is to find a set of uncoupled differential equations. For this we will take the scalar product of $\nabla_{\perp}$ with eq. (187)-(190).

The scalar product of $\nabla_{\perp}$ with eq. (187) can be simplified knowing $\nabla_{\perp}\cdot\left(\nabla_{\perp}\times V\mathbf{c}\right)=0$, $\nabla_{\perp}\cdot\left(\mathbf{c}\times\nabla_{\perp}V\right)=0$, $\nabla_{\perp}\cdot\left(\mathbf{c}\times\nabla_{\perp}\times V\mathbf{c}\right)=\nabla_{\perp}^{2}V$ and $\nabla_{\perp}\cdot\left(\mathbf{c}\times\mathbf{V}_{\perp}\right)=-\mathbf{c}\cdot(\nabla_{\perp}\times\mathbf{V}_{\perp})$.

$$\nabla_{\perp}^{2}H_{\parallel}-\frac{\partial\nabla_{\perp}^{2}\Pi}{\partial c}-\varepsilon_{\perp}\frac{\partial\nabla_{\perp}^{2}\Theta}{\partial t}=-\mathbf{c}\cdot\left(\nabla_{\perp}\times\mathbf{J}_{\perp}\right) \tag{191}$$

Using the same vector identities as above, the scalar products of $\nabla_{\perp}$ with eq.(188)-(190) become:

$$\nabla_{\perp}^{2}E_{\parallel}-\frac{\partial(\nabla_{\perp}^{2}\Phi)}{\partial c}+\mu\frac{\partial(\nabla_{\perp}^{2}\Psi)}{\partial t}=0 \tag{192}$$

$$-\frac{\partial(\nabla_{\perp}^{2}\Psi)}{\partial c}+\varepsilon_{\perp}\frac{\partial(\nabla_{\perp}^{2}\Phi)}{\partial t}=-\nabla_{\perp}\cdot\mathbf{J}_{\perp} \tag{193}$$

$$-\frac{\partial(\nabla_{\perp}^{2}\Theta)}{\partial c}-\mu\frac{\partial(\nabla_{\perp}^{2}\Pi)}{\partial t}=0 \tag{194}$$

We now introduce two auxiliary functions u and :

$$\nabla_{\perp}^{2}u=\nabla_{\perp}\cdot\mathbf{J}_{\perp} \tag{195}$$

$$\nabla_{\perp}^{2}v=-\mathbf{c}\cdot\left(\nabla_{\perp}\times\mathbf{J}_{\perp}\right) \tag{196}$$

and substitute eq.(195) in eq. (193) and eq.(196) in eq. (191).

$$-\frac{\partial(\nabla_{\perp}^{2}\Psi)}{\partial c}+\varepsilon_{\perp}\frac{\partial(\nabla_{\perp}^{2}\Phi)}{\partial t}=-\nabla_{\perp}^{2}u \tag{197}$$

$$\nabla_{\perp}^{2}H_{\parallel}-\frac{\partial(\nabla_{\perp}^{2}\Pi)}{\partial c}-\varepsilon_{\perp}\frac{\partial(\nabla_{\perp}^{2}\Theta)}{\partial t}=\nabla_{\perp}^{2}v \tag{198}$$

All terms of equations (192), (194), (197) and (198) contain the Laplace operator $\nabla_{\perp}^{2}$, which can thus be dropped [14], and the equations respectively become:

$$E_{\parallel} - \frac{\partial \Phi}{\partial c} + \mu \frac{\partial \Psi}{\partial t} = 0 \tag{199}$$

$$-\frac{\partial \Theta}{\partial c} - \mu \frac{\partial \Pi}{\partial t} = 0 \tag{200}$$

$$-\frac{\partial \Psi}{\partial c} + \varepsilon_{\perp} \frac{\partial \Phi}{\partial t} = -u \tag{201}$$

$$H_{\parallel} - \frac{\partial \Pi}{\partial c} - \varepsilon_{\perp} \frac{\partial \Theta}{\partial t} = v \tag{202}$$

We can substitute eq. (200) in the time derivative of (202).

$$\frac{\partial H_{\parallel}}{\partial t} = -\frac{1}{\mu} \frac{\partial^{2} \Theta}{\partial^{2} c} + \varepsilon_{\perp} \frac{\partial^{2} \Theta}{\partial^{2} t} + \frac{\partial v}{\partial t} \tag{203}$$

And substitute eq. (201) in the time derivative of eq. (199).

$$\frac{\partial E_{\parallel}}{\partial t} = -\frac{1}{\varepsilon_{\perp}} \frac{\partial u}{\partial c} + \frac{1}{\varepsilon_{\perp}} \frac{\partial^{2} \Psi}{\partial^{2} c} - \mu \frac{\partial^{2} \Psi}{\partial^{2} t} \tag{204}$$

Eq. (203) and (204) can then be substituted in eq. (186) and (185) respectively. We find two uncoupled differential equations for Θ and Ψ:

$$\nabla_{\perp}^{2} \Theta + \frac{\partial^{2} \Theta}{\partial^{2} c} - \mu \varepsilon_{\perp} \frac{\partial^{2} \Theta}{\partial^{2} t} = \mu \frac{\partial v}{\partial t} \tag{205}$$

$$-\nabla_{\perp}^{2} \Psi - \frac{\varepsilon_{\parallel}}{\varepsilon_{\perp}} \frac{\partial^{2} \Psi}{\partial^{2} c} + \mu \varepsilon_{\parallel} \frac{\partial^{2} \Psi}{\partial^{2} t} = -\frac{\varepsilon_{\parallel}}{\varepsilon_{\perp}} \frac{\partial u}{\partial c} + J_{\parallel} \tag{206}$$

Solving the differential equation

The uncoupled differential equations (205) and (206) are solved by taking their Fourier transform with respect to time and space. After the fourier transformation, the derivatives translate to multiplications by the following relations: $\nabla_{\perp} \to -j\mathbf{k}_{\perp}$, $\partial / \partial c \to -j\mathbf{k}_{\parallel}$ and $\partial / \partial t \to j\omega$. By these relations eq. (205) and (206) become:

$$-k_{\perp}^{2} \Theta - k_{c}^{2} \Theta + \mu \varepsilon_{\perp} \omega^{2} \Theta = j \mu \omega v \tag{207}$$

$$-k_{\perp}^{2} \Psi - \frac{\varepsilon_{\parallel}}{\varepsilon_{\perp}} k_{\parallel}^{2} \Psi + \mu \varepsilon_{\parallel} \omega^{2} \Psi = -j \frac{\varepsilon_{\parallel}}{\varepsilon_{\perp}} k_{\parallel} u - J_{\parallel} \mathbf{c} \tag{208}$$

This yields an expression for Θ and Ψ, which only depends on the source terms $J_{||}$, u and v.

$$\Theta = \frac{j\mu\omega v}{-k_{\perp}^2 - k_c^2 + \mu\varepsilon_{\perp}\omega^2} \tag{209}$$

$$\Psi = \frac{-j\frac{\varepsilon_{||}}{\varepsilon_{\perp}}k_{||}u - J_{||}\mathbf{c}}{-k_{\perp}^2 - \frac{\varepsilon_{||}}{\varepsilon_{\perp}}k_{||}^2 + \mu\varepsilon_{||}\omega^2} \tag{210}$$

Taking the fourier transform (in time and space) of eq. (201), (200), (203) and (204) gives an expression for the other four unknowns Φ, Π, $H_{||}$ and $E_{||}$.

$$\Phi = \frac{1}{\varepsilon_{\perp}}\left(\frac{j}{\omega}u - \frac{k_{||}}{\omega}\Psi\right) \tag{211}$$

$$\Pi = \frac{k_{||}}{\mu\omega}\Theta \tag{212}$$

$$H_{||} = j\left(\varepsilon_{\perp}\omega - \frac{1}{\mu\omega}k_{||}^2\right)\Theta + v \tag{213}$$

$$E_{||} = \frac{k_{||}}{\varepsilon_{\perp}\omega}u + j\left(\frac{k_{||}^2}{\varepsilon_{\perp}\omega} - \mu\omega\right)\Psi \tag{214}$$

Which allows us to construct $\mathbf{E}_{\perp}$ and $\mathbf{H}_{\perp}$ with eq. (183) and (184) .

$$\mathbf{E}_{\perp} = \frac{\mathbf{k}_{\perp}}{\varepsilon_{\perp}\omega}u + \frac{jk_{||}\mathbf{k}_{\perp}}{\varepsilon_{\perp}\omega}\Psi - j\mathbf{k}_{\perp} \times \Theta\mathbf{c} \tag{215}$$

$$\mathbf{H}_{\perp} = -j\mathbf{k}_{\perp}\frac{k_{||}}{\mu\omega}\Theta - j\mathbf{k}_{\perp} \times \Psi\mathbf{c} \tag{216}$$

And ultimately $\mathbf{E}$ (using eq. (170)):

$$\mathbf{E} = \frac{\mathbf{k}}{\varepsilon_{\perp}\omega}(u + jk_{||}\Psi) - j\mathbf{k}_{\perp} \times \Theta\mathbf{c} - j\mu\omega\Psi\mathbf{c} \tag{217}$$

Solution for an elementary electric dipole source

The expression for $\mathbf{E}$ derived above is valid for general sources in a uniaxial anisotropic medium. In this case we are interested in the electric field of an oscillating elementary electrical dipole. This field can be obtained by inserting the source term (and corresponding auxiliary functions u and v) in eq. (217).

The current density of an elementary electrical dipole in the origin is expressed as:

$$\mathbf{J} = \frac{\partial \mathbf{p}}{\partial t}\delta(\mathbf{r}) \qquad (218)$$

In this case $J_{||}$, u and v become:

$$\mathbf{J}_{||} = \frac{\partial \mathbf{p}_{||}}{\partial t}\delta(\mathbf{r}) \qquad (219)$$

$$\nabla_{\perp}^2 u = \nabla_{\perp} \cdot \frac{\partial \mathbf{p}_{\perp}}{\partial t}\delta(\mathbf{r}) \qquad (220)$$

$$\nabla_{\perp}^2 v = -\mathbf{c} \cdot \left(\nabla_{\perp} \times \frac{\partial \mathbf{p}_{\perp}}{\partial t}\delta(\mathbf{r}) \right) \qquad (221)$$

After fourier transformation (w.r.t. time and space) eq. (219)-(221) become:

$$\mathbf{J}_{||} = j\omega \mathbf{p}_{||} \qquad (222)$$

$$u = \frac{-\omega \mathbf{k}_{\perp} \cdot \mathbf{p}_{\perp}}{k_{\perp}^2} \qquad (223)$$

$$v = \omega \frac{\mathbf{c} \cdot \left(\mathbf{k}_{\perp} \times \mathbf{p}_{\perp} \right)}{k_{\perp}^2} \qquad (224)$$

Eq. (222)-(224) can be substituted into eq. (217), which is then rewritten as:

$$\begin{aligned} \mathbf{E}(\mathbf{k}) = {} & \frac{\dfrac{\mathbf{k}}{\varepsilon_{||}}(\mathbf{k}\cdot\mathbf{p}) - \mathbf{k}_{\perp}(\mathbf{k}_{\perp}\cdot\mathbf{p}_{\perp})\dfrac{\mu\omega^2}{k_{\perp}^2} - \dfrac{\mu\varepsilon_{\perp}}{\varepsilon_{||}}\omega^2 p_{||}\mathbf{c}}{-\dfrac{\varepsilon_{\perp}}{\varepsilon_{||}}k_{\perp}^2 - k_{||}^2 + \mu\varepsilon_{\perp}\omega^2} \\ & - j\mathbf{k}_{\perp} \times \frac{j\mu\omega^2}{k_{\perp}^2} \frac{\mathbf{c}\cdot(\mathbf{k}_{\perp}\times\mathbf{p}_{\perp})}{-k_{\perp}^2 - k_{||}^2 + \mu\varepsilon_{\perp}\omega^2}\mathbf{c} \end{aligned} \qquad (225)$$

Inverse fourier transformation

Eq. (225) expresses the electric field in the fourier domain. To obtain the plane wave expansion it is necessary to return (partly) to xyz-coordinates. This can be achieved by performing the inverse Fourier transform.

$$\mathbf{E}(x,y,z) = \frac{1}{(2\pi)^3} \int_{-\infty}^{+\infty}\int_{-\infty}^{+\infty}\int_{-\infty}^{+\infty} dk_x dk_y dk_z \mathbf{E}(\mathbf{k}) \exp\left[-j\left(k_x x + k_y y + k_z z\right)\right] \qquad (226)$$

By performing the inverse fourier transform for arbitrary xyz-coordinates, instead of a basis along the principal axes of the material, a general expression for the plane wave expansion is found. The plane wave expansion is found by only performing the integration over k_z explicitly.

The integration over k_z is performed by applying the Cauchy residue theorem over a suitable contour.

$$\int_{-\infty}^{+\infty} \mathbf{G}(k_z)dk_z = 2\pi j \lim_{k_z \to k_{z,o/e}} \mathbf{G}(k_z)(k_z - k_{z,o/e}) \tag{227}$$

Where $k_{z,o/e}$ is the pole of $\mathbf{G}(k_z)$ inside the contour. The contour should be chosen so that $\lim_{|k_z|\to\infty} \mathbf{G}(k_z) = 0$. To fulfil this requirement, it is necessary to choose a different contour for $z > 0$ and $z < 0$.

The two terms of eq. (225) have a different denominator with different poles. The contour integration is therefore performed separately for each term. We call the first term the extra-ordinary field $\mathbf{E}_e$, the second term is the ordinary field $\mathbf{E}_o$.

$$\mathbf{E}_e = \frac{\frac{\mathbf{k}}{\varepsilon_{\|}}(\mathbf{k}\cdot\mathbf{p}) - \mathbf{k}_{\perp}(\mathbf{k}_{\perp}\cdot\mathbf{p}_{\perp})\frac{\mu\omega^2}{k_{\perp}^2} - \frac{\mu\varepsilon_{\perp}}{\varepsilon_{\|}}\omega^2 p_{\|}\mathbf{c}}{-\frac{\varepsilon_{\perp}}{\varepsilon_{\|}}k_{\perp}^2 - k_c^2 + \mu\varepsilon_{\perp}\omega^2} \tag{228}$$

$$\mathbf{E}_o = -j\mathbf{k}_{\perp} \times \frac{j\mu\omega^2}{k_{\perp}^2} \frac{\mathbf{c}\cdot(\mathbf{k}_{\perp} \times \mathbf{p}_{\perp})}{-k_{\perp}^2 - k_{\|}^2 + \mu\varepsilon_{\perp}\omega^2}\mathbf{c} \tag{229}$$

<u>The ordinary field</u>

We can rewrite the denominator of eq. (229) in xyz-coordinates using $k_{\perp}^2 + k_{\|}^2 = \kappa^2 + k_z^2$. The poles are then given by:

$$k_{z,o} = \pm\sqrt{\mu\varepsilon_{\perp}\omega^2 - \kappa^2} \tag{230}$$

When $\kappa < \mu\varepsilon_{\perp}\omega^2$, the poles are purely real. If $\kappa > \mu\varepsilon_{\perp}\omega^2$ the poles lie on the imaginary axis. Four cases are distinguished for the evaluation of the integral:

- $\kappa > \mu\varepsilon_{\perp}\omega^2$, $z > 0$
- $\kappa > \mu\varepsilon_{\perp}\omega^2$, $z < 0$

- $\kappa < \mu\varepsilon_{\perp}\omega^2,\ z > 0$
- $\kappa < \mu\varepsilon_{\perp}\omega^2,\ z < 0$

The location of the poles and the appropriate contour for each case are displayed in the figure below .

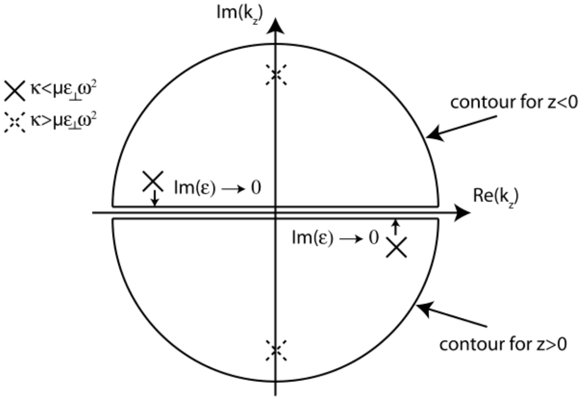

When $\kappa < \mu\varepsilon_{\perp}\omega^2$, the poles are real numbers. In order to perform the contour integration , a small negative imaginary component is added to $\varepsilon_{\perp}$. After integration the limit for $\mathrm{Im}\,\varepsilon_{\perp} \to 0$ is taken.

For the case of $z > 0$, the following expression is found for $\mathbf{E}_o$ after integration.

$$\mathbf{E}_o = \frac{-j\mu\omega^2}{8\pi^2}\int_{-\infty}^{+\infty}\int_{-\infty}^{+\infty} dk_x dk_y \frac{\mathbf{c}\cdot\left(\mathbf{k}_{\perp}\times\mathbf{p}_{\perp}\right)}{k_{z,o}}\frac{\mathbf{k}_{\perp}\times\mathbf{c}}{k_{\perp}^2}\exp\left[-j(k_x x + k_y y + k_{z,o}z)\right] \quad (231)$$

In eq. (230) for $k_{z,o}$ the positive root should be taken if $\kappa < \mu\varepsilon_{\perp}\omega^2$, the negative root should be taken if $\kappa > \mu\varepsilon_{\perp}\omega^2$. For $z < 0$ the same formula applies but with reversed sign for $k_{z,o}$. The negative root for $\kappa < \mu\varepsilon_{\perp}\omega^2$, the positive root if $\kappa > \mu\varepsilon_{\perp}\omega^2$.

The extra-ordinary field

Finding the poles for the extra-ordinary field is more complicated. First we rewrite the denominator of eq. (228).

$$-\frac{\varepsilon_{\perp}}{\varepsilon_{||}}k_{\perp}^2 - k_{||}^2 + \mu\varepsilon_{\perp}\omega^2 = -\frac{\varepsilon_{\perp}}{\varepsilon_{||}}\left(k_{\perp}^2 + k_{||}^2\right) - \frac{\Delta\varepsilon}{\varepsilon_{||}}k_{||}^2 + \mu\varepsilon_{\perp}\omega^2 \quad (232)$$

Now we will change to the xyz-basis using: $k_\perp^2 + k_\parallel^2 = \kappa^2 + k_z^2$ and $k_\parallel = \mathbf{c}\cdot(\kappa + k_z\mathbf{z}) = \kappa c_t + k_z c_z$. With $c_t = \mathbf{c}\cdot\boldsymbol{\kappa}$ and $c_z = \mathbf{c}\cdot\mathbf{z}$ the denominator of eq. (228) can be written in terms of κ and k_z.

$$\mu\varepsilon_\perp\omega^2 - \kappa^2\left(\frac{\varepsilon_\perp + \Delta\varepsilon c_t^2}{\varepsilon_\parallel}\right) - \frac{2\Delta\varepsilon}{\varepsilon_\parallel}c_t c_z \kappa k_z - k_z^2\left(\frac{\varepsilon_\perp + \Delta\varepsilon c_z^2}{\varepsilon_\parallel}\right) \tag{233}$$

With $\Delta\varepsilon = \varepsilon_\parallel - \varepsilon_\perp$. The roots of this expression are:

$$k_{z,e} = \frac{-\Delta\varepsilon c_t c_z \kappa}{\varepsilon_\perp + \Delta\varepsilon c_z^2} \mp \frac{\sqrt{\mu\varepsilon_\perp\varepsilon_\parallel\left[\varepsilon_\perp + \Delta\varepsilon c_z^2\right]\omega^2 - \kappa^2\varepsilon_\perp\left[\varepsilon_\perp + \Delta\varepsilon(c_z^2 + c_t^2)\right]}}{\varepsilon_\perp + \Delta\varepsilon c_z^2} \tag{234}$$

The poles become complex when $\kappa > \kappa_{crit}$.

$$\kappa_{crit}^2 = \mu\varepsilon_\parallel\omega^2 \frac{\varepsilon_\perp + \Delta\varepsilon c_z^2}{\varepsilon_\perp + \Delta\varepsilon(c_z^2 + c_t^2)} \tag{235}$$

With the poles given by eq.(234) the integral of eq. (228) can be evaluated. Once again the appropriate contour (sketched in the figure below) should be chosen for four situations:

- $\kappa > \kappa_{crit}$, $z > 0$
- $\kappa > \kappa_{crit}$, $z < 0$
- $\kappa < \kappa_{crit}$, $z > 0$
- $\kappa < \kappa_{crit}$, $z < 0$

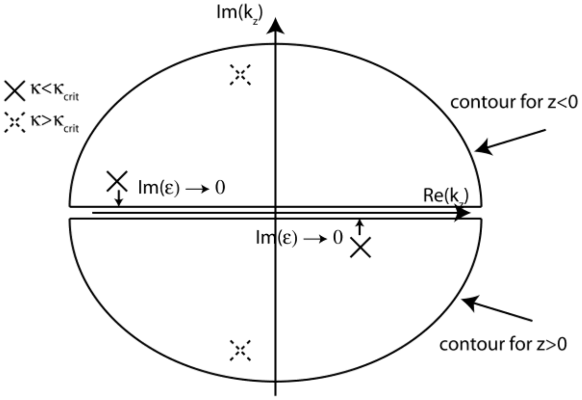

When $\kappa < \kappa_{crit}$, the poles are real numbers. In order to perform the contour integration , a small negative imaginary component is added to $\varepsilon_{\|}$. After integration the limit for $\mathrm{Im}\,\varepsilon_{\|} \to 0$ is taken.

For the case of $z > 0$, the following expression is found for $\mathbf{E}_e$ after integration.

$$\mathbf{E}_e = \frac{-j}{8\pi^2} \int_{-\infty}^{+\infty} \int_{-\infty}^{+\infty} dk_x dk_y \, \frac{\mathbf{k}_\perp - \dfrac{k_\perp^2 \varepsilon_\perp}{k_\|^2 \varepsilon_\|} \mathbf{k}_\|}{\dfrac{\varepsilon_\perp + \Delta\varepsilon c_z^2}{\varepsilon_\|} \left(k_{z,e} + \dfrac{\Delta\varepsilon c_t c_z \kappa}{\varepsilon_\perp + \Delta\varepsilon c_z^2}\right)} \left(\frac{k_\| p_\|}{\varepsilon_\|} - \frac{k_\|^2 \left(\mathbf{k}_\perp \cdot \mathbf{p}_\perp\right)}{k_\perp^2 \varepsilon_\perp} \right) \exp\left[-j(k_x x + k_y y + k_{z,e} z)\right] \qquad (236)$$

In eq. (234) for $k_{z,e}$ the positive root should be taken if $\kappa < \kappa_{crit}$, the negative root should be taken if $\kappa > \kappa_{crit}$. For $z < 0$ the same formula applies but with reversed sign for $k_{z,e}$. The negative root for $\kappa < \kappa_{crit}$, the positive root if $\kappa > \kappa_{crit}$.

Eq. (231) and (236) represent $\mathbf{E}_o$ and $\mathbf{E}_e$ as a sum of plane waves k_x, k_y for an arbitrary xyz -system for any orientation of the dipole moment. This general formulation of the dipole filed can be readily used.

List of publications

International journal papers

1. O. Pietraszkiewicz, S. Mal, M. Pietraszkiewicz, M. Maciejczyk, I. Czerski, T. Borowiak, G. Dutkiewicz, O. Drobchak, L. Penninck, J. Beeckman, and K. Neyts, "Highly photoluminescent Eu(III) complexes of the new 1-triphenylen-2-yl-3-trifluoroacetylacetone," Journal of Photochemistry and Photobiology A: Chemistry 250, 85-91 (2012).
2. L. Penninck, F. Steinbacher, R. Krause, and K. Neyts, "Determining emissive dipole orientation in organic light emitting devices by decay time measurement," Org. Electron. **13**, 3079-3084 (2012).
3. L. Penninck, J. Beeckman, P. De Visschere, and K. Neyts, "Light emission from dye-doped cholesteric liquid crystals at oblique angles: Simulation and experiment," Physical Review E **85**, 041702 (2012).
4. L. Penninck, P. D. Visschere, J. Beeckman, and K. Neyts, "Simulating the Emission Properties of Luminescent Dyes within One-Dimensional Uniaxial Liquid Crystal Microcavities," Mol. Cryst. Liquid Cryst. **560**, 82-92 (2012).

5. L. Penninck, P. De Visschere, J. Beeckman, and K. Neyts, "Dipole radiation within one-dimensional anisotropic microcavities: a simulation method," Opt. Express **19**, 18558-18576 (2011).
6. S. Mladenovski, S. Hofmann, S. Reineke, L. Penninck, T. Verschueren, and K. Neyts, "Integrated optical model for Organic Light-Emitting Devices," J. Appl. Phys. **109**, 083114-083111-083119 (2011).
7. S. Mladenovski, S. Reineke, L. Penninck, and K. Neyts, "Detailed analysis of exciton decay time change in organic light-emitting devices caused by optical effects," J. Soc. Inf. Disp. **19**, 80-86 (2011).
8. L. Penninck, S. Mladenowski, and K. Neyts, "The effects of planar metallic interfaces on the radiation of nearby electrical dipoles," Journal of Optics **12**, 8 (2010).

International conference contributions

9. L. Penninck, F. Steinbacher , R. Krause, and K. Neyts *“Measurement and analysis of evaporated organic light emitting devices with oriented dipole emitters”* Presented at the 16th International Workshop on Inorganic and Organic Electroluminescence. EL , Hong Kong, 2012
10. K. Neyts, L. Penninck, and P. De Visschere, *“Light emission and outcoupling from OLEDs and anisotropic layers”* Presented at the 16th International Workshop on Inorganic and Organic Electroluminescence. EL , Hong Kong, 2012
11. L. Penninck, and K. Neyts, *"Optical outcoupling by oriented emission in top and bottom emitting OLEDs"* Presented at the 24th IEEE Photonics Conference IPC, Burlingame, United States of America, 2012.
12. L. Penninck, P. De Visschere, J. Beeckman, and K. Neyts, *" Modelling of light emission inside planar liquid crystal photonic devices"*

Presented at the 24th International Liquid Crystal Conference ILCC, Mainz, Germany, 2012.

13. K. Neyts, L. Penninck, and P. De Visschere, *" Simulation and measurement of light emission and change in decay rate in organic light emitting devices"* Presented at the International Conference on Simulation of Organic Electronics and Photovoltaics, Oliva, Spain, 2012.
14. L. Penninck, P. De Visschere, J. Beeckman, and K. Neyts, *" Simulating the emission properties of luminescent dyes in liquid crystals"* Presented at the 14th International Topical Meeting Optics of Liquid Crystals OLC, Yerevan, Armenia, 2011.
15. L. Penninck, S. Mladenovski, S. Hofmann, S. Reineke, T. Verschueren, and K. Neyts, *"The Efficiency Of Radiative Decay Inside Organic Light Emitting Diodes"* Presented at the 30th International Display Research Conference. Eurodisplay , Arcachon, France, 2011.
16. K. Neyts , S. Mladenovski , L. Penninck , and S. Reineke, *"Interference and decay time change for the emission from a thin film"* Presented at the 15th International Workshop on Inorganic and Organic Electroluminescence. EL , St. Petersburg, Russia, 2010

Other

17. L. Penninck, J. Beeckman ,P. De Visschere and K. Neyts, *"Light emission from thin films"* First Annual Meeting of the 7th phase of the IAP network "photonics@be", Brussel, 2012
18. T. Ako, J. Beeckman, L. Penninck and K Neyts , "Luminescence in Liquid Crystals (LC) with Nanoparticles and Nanostructures" NB-Photonics Annual Meeting 2012, Gent, 2012

19. L. Penninck, K. Neyts, “Dipole radiation near metal interfaces for electroluminescence” 11^{e} Ugent-Firw Doctoraatssymposium, Gent, 2010
20. L. Penninck, S. Mladenovski, P. Bienstman and K. Neyts, “*Extracting waveguided light with periodic gratings.“* V International Krutyn Summer School, Krutyn, Poland, 2009

References

1. S. Reineke, F. Lindner, G. Schwartz, N. Seidler, K. Walzer, B. Lüssem, and K. Leo, "White organic light-emitting diodes with fluorescent tube efficiency," Nature **459**, 234-U116 (2009).
2. N. Y. Ha, S. M. Jeong, S. Nishimura, G. Suzaki, K. Ishikawa, and H. Takezoe, "Simultaneous red, green, and blue lasing emissions in a single-pitched cholesteric liquid-crystal system," Advanced Materials **20**, 2503-+ (2008).
3. R. Feynman, Transcribed from http://www.youtube.com/watch?src_vid=AU8PId_6xec&feature=iv&v=1qQQXTMih1A&annotation_id=annotation_43514.
4. http://apps1.eere.energy.gov/buildings/publications/pdfs/ssl/energy_efficiency_white_leds.pdf.
5. , http://barrett-group.mcgill.ca/tutorials/liquid_crystal/LC02.htm.
6. A. Einstein, *Zur Quantentheorie der Strahlung* (Gebr. Leemann & Co., 1916).
7. T. H. Maiman, "STIMULATED OPTICAL RADIATION IN RUBY," Nature **187**, 493-494 (1960).
8. G. Overton, "LASER DISPLAYS Liquid-crystal laser promises low-fabrication-cost display," Laser Focus World **45**, 44-45 (2009).
9. A. Yariv, and P. Yeh, *Optical Waves in Crystals: Propagation and Control of Laser Radiation* (Wiley, 2002).
10. M. Born, E. Wolf, and A. B. Bhatia, *Principles of optics: electromagnetic theory of propagation, interference and diffraction of light* (Cambridge University Press, 1999).
11. W. Lukosz, "Light-emission by multipole sources in thin-layers .1. Radiation-patterns of electric and magnetic dipoles," Journal of the Optical Society of America **71**, 744-754 (1981).

12. L. Penninck, S. Mladenowski, and K. Neyts, "The effects of planar metallic interfaces on the radiation of nearby electrical dipoles," Journal of Optics **12**, 8 (2010).

13. P. C. Clemmow, "The theory of electromagnetic waves in a simple anisotropic medium," Electrical Engineers, Proceedings of the Institution of **110**, 101-106 (1963).

14. P. De Visschere, "Electromagnetic source transformations and scalarization in stratified gyrotropic media," Progress In Electromagnetics Research B **18**, 165-183 (2009).

15. R. Loudon, *The Quantum Theory of Light* (Oxford University Press, 2000).

16. W. Lukosz, "Theory of optical-environment-dependent spontaneous-emission rates for emitters in thin-layers," Physical Review B **22**, 3030-3038 (1980).

17. K. Neyts, "Simulation of light emission from thin-film microcavities," Journal of the Optical Society of America. A, Optics image science and Vision **15**, 962-971 (1998).

18. T. Setälä, M. Kaivola, and A. Friberg, "Decomposition of the point-dipole field into homogeneous and evanescent parts," Physical review. E, Statistical physics, plasmas, fluids, and related interdisciplinary topics **59**, 1200-1206 (1999).

19. D. Y. K. Ko, and J. R. Sambles, "Scattering matrix-method for propagation of radiation in stratified media - attenuated total reflection studies of liquid-crystals," Journal of the Optical Society of America. A, Optics image science and Vision **5**, 1863-1866 (1988).

20. D. W. Berreman, "Optics in stratified and anisotropic media - 4x4 matrix formulation," Journal of the Optical Society of America **62**, 502-510 (1972).

21. J. Kalinowski, *Organic Light-emitting Diodes: Principles, Characteristics, And Processes* (Marcel Dekker, 2005).

22. G. Mueller, R. K. Willardson, and E. R. Weber, *Semiconductors and Semimetals: Electroluminescence II* (Academic Press, 2000).

23. S. Mladenovski, S. Hofmann, S. Reineke, L. Penninck, T. Verschueren, and K. Neyts, "Integrated optical model for Organic Light-Emitting Devices," J. Appl. Phys. **109**, 083114-083111-083119 (2011).

24. C. Adachi, M. A. Baldo, M. E. Thompson, and S. R. Forrest, "Nearly 100% internal phosphorescence efficiency in an organic light-emitting device," J. Appl. Phys. **90**, 5048-5051 (2001).

25. M. Bass, and O. S. o. America, *Handbook of optics* (McGraw-Hill, 2001).

26. T. Markvart, "The thermodynamics of optical etendue," J. Opt. A-Pure Appl. Opt. **10**, 7 (2008).

27. S. K. So, W. K. Choi, L. M. Leung, and K. Neyts, "Interference effects in bilayer organic light-emitting diodes," Appl. Phys. Lett. **74**, 1939-1941 (1999).

28. H. Greiner, "Light extraction from organic light emitting diode substrates: Simulation and experiment," Jpn. J. Appl. Phys. Part 1 - Regul. Pap. Brief Commun. Rev. Pap. **46**, 4125-4137 (2007).

29. R. Bathelt, D. Buchhauser, C. Garditz, R. Paetzold, and P. Wellmann, "Light extraction from OLEDs for lighting applications through light scattering," Org. Electron. **8**, 293-299 (2007).

30. P. Bienstman, P. Vandersteegen, and R. Baets, "Modelling gratings on either side of the substrate for light extraction in light-emitting diodes," Opt. Quantum Electron. **39**, 797-804 (2007).

31. K. Neyts, and A. U. Nieto, "Importance of scattering and absorption for the outcoupling efficiency in organic light-emitting devices," J. Opt. Soc. Am. A-Opt. Image Sci. Vis. **23**, 1201-1206 (2006).

32. H. Sasabe, J.-i. Takamatsu, T. Motoyama, S. Watanabe, G. Wagenblast, N. Langer, O. Molt, E. Fuchs, C. Lennartz, and J. Kido, "High-Efficiency Blue and White Organic Light-Emitting Devices Incorporating a Blue Iridium Carbene Complex," Advanced Materials **22**, 5003-5007 (2010).

33. B. J. Scholz, J. Frischeisen, A. Jaeger, D. S. Setz, T. C. G. Reusch, and W. Brutting, "Extraction of surface plasmons in organic light-emitting diodes via high-index coupling," Opt. Express **20**, A205-A212 (2012).

34. A. V. Zayats, Smolyaninov, II, and A. A. Maradudin, "Nano-optics of surface plasmon polaritons," Phys. Rep.-Rev. Sec. Phys. Lett. **408**, 131-314 (2005).

35. S. I. I. Zayats A V, and M. A. A, "Nano-optics of surface plasmon polaritons," Phys. Rep. **408**, 131 (2005).

36. P. A. Hobson, J. A. E. Wasey, I. Sage, and W. L. Barnes, "The role of surface plasmons in organic light-emitting diodes," IEEE J. Sel. Top. Quantum Electron. **8**, 378-386 (2002).

37. D. Z. Garbuzov, S. R. Forrest, A. G. Tsekoun, P. E. Burrows, V. Bulovic, and M. E. Thompson, "Organic films deposited on Si p-n junctions: Accurate measurements of fluorescence internal efficiency, and application to luminescent antireflection coatings," J. Appl. Phys. **80**, 4644-4648 (1996).

38. M. j. Weber, *Handbook of optical materials* (CRC Press, 2003).

39. M. P. Aldred, A. E. A. Contoret, S. R. Farrar, S. M. Kelly, D. Mathieson, M. O'Neill, W. C. Tsoi, and P. Vlachos, "A full-color electroluminescent device and patterned photoalignment using light-emitting liquid crystals," Advanced Materials **17**, 1368-1372 (2005).

40. W. M. V. Wan, R. H. Friend, and N. C. Greenham, "Modelling of interference effects in anisotropic conjugated polymer devices," Thin Solid Films **363**, 310-313 (2000).

41. M. Flammich, M. C. Gather, N. Danz, D. Michaelis, A. H. Brauer, K. Meerholz, and A. Tunnermann, "Orientation of emissive dipoles in OLEDs: Quantitative in situ analysis," Org. Electron. **11**, 1039-1046 (2010).

42. J. Frischeisen, D. Yokoyama, C. Adachi, and W. Bruetting, "Determination of molecular dipole orientation in doped fluorescent organic thin films by photoluminescence measurements," Appl. Phys. Lett. **96**, 3 (2011).

43. L. Penninck, F. Steinbacher, R. Krause, and K. Neyts, "Determining emissive dipole orientation in organic light emitting devices by decay time measurement," Org. Electron. **13**, 3079-3084 (2012).

44. L. Penninck, J. Beeckman, P. De Visschere, and K. Neyts, "Light emission from dye-doped cholesteric liquid crystals at oblique angles: Simulation and experiment," Physical Review E **85**, 041702 (2012).

45. D. V. O'Connor, and D. Phillips, *Time-correlated single photon counting* (Academic Press, 1984).

46. M. Flammich, J. Frischeisen, D. S. Setz, D. Michaelis, B. C. Krummacher, T. D. Schmidt, W. Brutting, and N. Danz, "Oriented phosphorescent emitters boost OLED efficiency," Org. Electron. **12**, 1663-1668 (2011).

47. K. Driesen, D. Moors, J. Beeckman, K. Neyts, C. Gorller-Walrand, and K. Binnemans, "Near-infrared luminescence emitted by an electrically switched liquid crystal cell," Journal of Luminescence **127**, 611-615 (2007).

48. W. De Cort, J. Beeckman, R. James, F. A. Fernandez, R. Baets, and K. Neyts, "Tuning of silicon-on-insulator ring resonators with liquid crystal cladding using the longitudinal field component," Opt. Lett. **34**, 2054-2056 (2009).

49. C. L. Mulder, P. D. Reusswig, A. M. Velázquez, H. Kim, C. Rotschild, and M. A. Baldo, "Dye alignment in luminescent solar concentrators: I. Vertical alignment for improved waveguide coupling," Opt. Express **18**, A79-A90 (2010).

50. C. L. Mulder, P. D. Reusswig, A. P. Beyler, H. Kim, C. Rotschild, and M. A. Baldo, "Dye alignment in luminescent solar concentrators: II. Horizontal alignment for energy harvesting in linear polarizers," Opt. Express **18**, A91-A99.

51. M. O'Neill, and S. M. Kelly, "Liquid crystals for charge transport, luminescence, and photonics," Advanced Materials **15**, 1135-1146 (2003).

52. M. O'Neill, and S. M. Kelly, "Ordered Materials for Organic Electronics and Photonics," Advanced Materials **23**, 566-584 (2010).

53. P. Yeh, and C. Gu, *Optics of liquid crystal displays* (Wiley, New York, 1999).

54. I. C. Khoo, *Liquid crystals* (Wiley-Interscience, 2007).

55. , http://www.nature.com/materials/nanozone/newsandviews/021017/419681a_f1.html.

56. M. Ozaki, M. Kasano, D. Ganzke, W. Haase, and K. Yoshino, "Mirrorless lasing in a dye-doped ferroelectric liquid crystal," Advanced Materials **14**, 306-+ (2002).

57. Y. J. Liu, X. W. Sun, P. Shum, H. P. Li, J. Mi, W. Ji, and X. H. Zhang, "Low-threshold and narrow-linewidth lasing from dye-doped holographic polymer-dispersed liquid crystal transmission gratings," Appl. Phys. Lett. **88**, 3 (2006).

58. W. Y. Cao, A. Munoz, P. Palffy-Muhoray, and B. Taheri, "Lasing in a three-dimensional photonic crystal of the liquid crystal blue phase II," Nat. Mater. **1**, 111-113 (2002).

59. S. Bolis, "Lasing and Gain in Liquid Crystals," (Université Libre de Bruxelles, Brussels, 2011), p. 49.

60. K. Funamoto, M. Ozaki, and K. Yoshino, "Discontinuous shift of lasing wavelength with temperature in cholesteric liquid crystal," Jpn. J. Appl. Phys. Part 2 - Lett. **42**, L1523-L1525 (2003).

61. H. Finkelmann, S. T. Kim, A. Munoz, P. Palffy-Muhoray, and B. Taheri, "Tunable mirrorless lasing in cholesteric liquid crystalline elastomers," Advanced Materials **13**, 1069-1072 (2001).

62. Y. Inoue, H. Yoshida, K. Inoue, Y. Shiozaki, H. Kubo, A. Fujii, and M. Ozaki, "Tunable Lasing from a Cholesteric Liquid Crystal Film Embedded with a Liquid Crystal Nanopore Network," Advanced Materials **23**, 5498-+ (2011).

63. M. H. Song, B. Park, S. Nishimura, T. Toyooka, I. J. Chung, Y. Takanishi, K. Ishikawa, and H. Takezoe, "Electrotunable non-reciprocal laser emission from a liquid-crystal photonic device," Adv. Funct. Mater. **16**, 1793-1798 (2006).

64. A. Chanishvili, G. Chilaya, G. Petriashvili, R. Barberi, R. Bartolino, G. Cipparrone, A. Mazzulla, R. Gimenez, L. Oriol, and M. Pinol, "Widely tunable ultraviolet-visible liquid crystal laser," Appl. Phys. Lett. **86**, 3 (2005).

65. A. D. Ford, S. M. Morris, and H. J. Coles, "Phototonics and lasing in liquid crystals," Mater. Today **9**, 36-42 (2006).

66. H. Coles, and S. Morris, "Liquid-crystal lasers," Nat. Photonics **4**, 676-685 (2010).

67. B. Fan, S. Vartak, J. N. Eakin, and S. M. Faris, "Broadband polarizing films by photopolymerization-induced phase separation and in situ swelling," Appl. Phys. Lett. **92**, 3 (2008).

68. A. C. Tasolamprou, M. Mitov, D. C. Zografopoulos, and E. E. Kriezis, "Theoretical and experimental studies of hyperreflective polymer-network

cholesteric liquid crystal structures with helicity inversion," Opt. Commun. **282**, 903-907 (2009).

69. M. Mitov, and N. Dessaud, "Going beyond the reflectance limit of cholesteric liquid crystals," Nat. Mater. **5**, 361-364 (2006).

70. N. V. Tabiryan, S. R. Nersisyan, T. J. White, T. J. Bunning, D. M. Steeves, and B. R. Kimball, "Transparent thin film polarizing and optical control systems," AIP Adv. **1**, 022153 (022111 pp.)-022153 (022111 pp.)022153 (022111 pp.) (2011).

71. B. Kwang-Soo, C. Uiyeong, M. Yeon-Kyu, H. Jeong Wook, L. You-Jin, K. Jae-Hoon, and Y. Chang-Jae, "Reflective three-dimensional displays using the cholesteric liquid crystal with an inner patterned retarder," Opt. Express **20**, 6927-69316931 (2012).

72. F. Castles, S. M. Morris, D. J. Gardiner, Q. M. Malik, and H. J. Coles, "Ultra-fast-switching flexoelectric liquid-crystal display with high contrast," J. Soc. Inf. Disp. **18**, 128-133 (2010).

73. C. Oldano, E. Miraldi, and P. T. Valabrega, "DISPERSION-RELATION FOR PROPAGATION OF LIGHT IN CHOLESTERIC LIQUID-CRYSTALS," Phys. Rev. A **27**, 3291-3299 (1983).

74. J. Schmidtke, and W. Stille, "Fluorescence of a dye-doped cholesteric liquid crystal film in the region of the stop band: theory and experiment," Eur. Phys. J. B **31**, 179-194 (2003).

75. L. Penninck, P. De Visschere, J. Beeckman, and K. Neyts, "Dipole radiation within one-dimensional anisotropic microcavities: a simulation method," Opt. Express **19**, 18558-18576 (2011).

76. K. Panajotov, M. Zujewski, and H. Thienpont, "Coupled-cavity surface-emitting lasers: spectral and polarization threshold characteristics and electrooptic switching," Opt. Express **18**, 27525-27533 (2010).

77. C. K. Liu, A. Y. G. Fuh, Y. D. Chen, and K. T. Cheng, "Controlling pitch length of chiral monomer-doped nematic/cholesteric liquid crystals using photopolymerization," J. Phys. D-Appl. Phys. **43**, 5 (2010).

78. P. Lalanne, and E. Silberstein, "Fourier-modal methods applied to waveguide computational problems," Opt. Lett. **25**, 1092-1094 (2000).

79. E. N. Glytsis, and T. K. Gaylord, "3-DIMENSIONAL (VECTOR) RIGOROUS COUPLED-WAVE ANALYSIS OF ANISOTROPIC GRATING DIFFRACTION," J. Opt. Soc. Am. A-Opt. Image Sci. Vis. **7**, 1399-1420 (1990).

80. T. Matsui, and M. Kitaguchi, "Finite-Difference Time-Domain Analysis of Laser Action in Cholesteric Photonic Liquid Crystal," Appl. Phys. Express **3**, 3 (2010).